3-2006

Fretting Fatigue Behavior of Nickel Alloy IN-100

Elhoucine Madhi

FRETTING FATIGUE BEHAVIOR OF NICKEL ALLOY IN-100

THESIS

Elhoucine MADHI, Captain, RMAF

AFIT/GAE/ENY/06-M22

DEPARTMENT OF THE AIR FORCE
AIR UNIVERSITY

AIR FORCE INSTITUTE OF TECHNOLOGY

Wright-Patterson Air Force Base, Ohio

The views expressed in this thesis are those of the author and do not reflect the official policy or position of the United States Air Force, Department of Defense, or the United States Government.

AFIT/GAE/ENY/06-M22

FRETTING FATIGUE BEHAVIOR OF NICKEL ALLOY IN-100

THESIS

Presented to the Faculty

Department of Aeronautics and Astronautics

Graduate School of Engineering and Management

Air Force Institute of Technology

Air University

Air Education and Training Command

In Partial Fulfillment of the Requirements for the

Degree of Master of Science in Aerospace Engineering

Elhoucine MADHI, B.S.A.E.

Captain, RMAF

March 2006

AFIT/GAE/ENY/06-M22

FRETTING FATIGUE BEHAVIOR OF NICKEL ALLOY IN-100

Elhoucine MADHI, B.S.A.E.
Captain, RMAF

Approved:

Dr. S. Mall, PhD (Advisor)	date
Dr. V.K. Jain (Member)	date
Dr. T. Nicholas (Member)	date

AFIT/GAE/ENY/06-M22

Abstract

In this study, a systematic investigation of the fretting fatigue behavior of nickel alloy, IN-100 was carried out. The study includes both experimental work and the corresponding analysis of the contact conditions, and the latter is accomplished using the finite element method. Fretting fatigue tests were performed over a wide range of axial stresses to examine both low and high cycle fretting fatigue under constant contact load and the influence of different pad geometries was also explored. It was observed that fretting reduced the fatigue strength of IN-100, and that increasing cylindrical pad radii does not have the same effect as in titanium-based alloys. The crack initiation location and orientation along the surface were measured using the Optical and Scanning Electron Microscopy (SEM). In all experiments, cracks were found to initiate near the contact zone trailing edge, and at an orientation of $\pm 45^o$ with a scatter of $\pm 10^o$. Finite element analysis was conducted through the commercially available software, ABAQUS, to obtain the contact region state variables such as stress, strain and displacement. These state variables were needed for the computation and analysis of fretting fatigue crack initiation parameters which were Findley parameter, Smith-Watson-Topper (SWT) parameter, shear stress range (SSR), and modified shear stress range (MSSR). These parameters were evaluated based on their ability to predict crack location, crack initiation angle and fatigue life without dependence on contact geometry. The comparison of the analysis and the experimental results showed that fretting fatigue life is not only governed by shear stress on the critical plane, but also the normal stresses plays a role in the crack initiation mechanism. After adjusting the constants used in MSSR calculations for Ti-6Al-4V, it was found that MSSR parameter is also capable of predicting crack location, crack initiation angle and fatigue life in IN-100.

Acknowledgements

First, I would like to thank my advisor and idol, Dr Mall, for believing in me and granting me the honor of working under his supervision. It has truthfully been an enriching experience. I want to thank my wife, my two kids, as well my parents for all the support I received at home which was paramount in this endeavor. I would also like to thank Dr. Sabelkin and Dr. Hyukjae Lee for their guidance and support to accomplish the Finite Element Analysis part of the thesis.

Finally, I owe a large debt of gratitude the Royal Moroccan Air Force who granted me this once in a lifetime opportunity to achieve my Master's degree in Aerospace Engineering at AFIT.

Elhoucine MADHI

Table of Contents

Page

List of Figures

List of Tables

List of Symbols

Symbol		Page
N_i	number of cycles to crack initiation	15
ϵ_a	strain amplitude	15
$\epsilon_f^{'}$	strain amplitude	15
τ_{max}	maximum local shear stress	16
τ_{min}	minimum local shear stress	16
σ_{yy}	normal stress along the y-direction	16
m	fitting parameter	17
R_τ	stress ratio on the critical plane	17
$\Delta\tau_{crit}$	shear stress range	17
K_2	Ruiz parameter	18
α	resolved shear stress of slip system	20
n^α	unit vector normal to the slip plane	20
m^α	unit vector along the slip direction of the slip system	20
$\Delta\tau_{max}/2$	maximum resolved shear stress amplitude of slip systems	20
N_f	fatigue life	20
τ_m	mean resolved shear stress on maximum shear slip system	20
τ_b	resolved shear stress related to ultimate tensile strength	20
N	the number of cycles	21
SCN	Single Crystal Nickel	22
Q_{load}	resulting tangential load	28
V	axial load applied by actuator at the lower end of specimen	28
W	the load applied at the upper end to grip the specimen	28
Q_{max}	maximum tangential load	28
Q_{min}	minimum tangential load	28
δ_{max}	maximum displacement	39
$\tau_{x,max}$	maximum shear stress along the x-direction	39
$\Delta\tau_{x,max}$	maximum shear stress range along the x-direction	39
$\sigma_{xx,max}$	maximum axial stress	39

Symbol		Page
$\sigma_{xx,min}$	minimum axial stress	39
FEA	finite element analysis	39
$a_{Ruiz,max}$	contact half width predicted by Ruiz program	43
$a_{Ruiz,max}$	contact half width predicted by Ruiz program	43
$\sigma_{xx,FEA}$	local axial stress as predicted by FEA	43
$\sigma_{xx,Ruiz}$	local axial stress as predicted by Ruiz program	43
$\sigma_{xy,FEA}$	local shear stress as predicted by FEA	43
$\sigma_{yy,Ruiz}$	local axial stress as predicted by Ruiz program	43
$\sigma_{xy,FEA}$	local axial stress as predicted by Ruiz program	44
$\tau_{xy,Ruiz}$	local axial stress as predicted by Ruiz program	44
SEM	scanning electron microscopy	59
$\sigma_{effective}$	Effective Stress	62
R	stress ratio	62

FRETTING FATIGUE BEHAVIOR OF NICKEL ALLOY IN-100

I. Introduction

1.1 Fretting Fatigue

Fretting, recently recognized as an important failure mode, is the surface damage that occurs at the interface between two nominally clamped free surfaces that are undergoing an oscillatory motion of small amplitude. This results in an increased production of debris due to surface wear and initiation of fatigue cracks. When the presence of fretting is associated with a notable reduction in a structural part's service life, the effect is known as fretting fatigue. The fretting fatigue mechanism is driven by the stress fields generated by the clamping of the two surface topographies. Under fretting fatigue, tensile and shear stresses are increased at the contact zone producing surface defects which act as stress concentration sites promoting crack nucleation. Once cracks are initiated, bulk stresses become concentrated in their respective zones resulting in crack propagation. Not only can fretting fatigue cause an increase in maintenance costs, but it also results in a significant reduction in aircraft and engine components' service life and eventually leads to their premature failure. The presence of fretting fatigue conditions in flight structures has been responsible, at times, for high strength reduction factors, of 10 or more. As a result, fretting fatigue is of great interest to the research community since it is frequently encountered in several aircraft structural components. For instance, fretting fatigue is known to develop in the dovetail joints, at the interface between the turbine engine disk slot and blade attachment as shown in Fig. 1.1. Damage can also nucleate at riveted, bolted joints, metallic cables, coil wedges, snap fit areas and other clamped members. Component failure due to fretting fatigue is characterized by four stages: crack initiation, crack propagation due to the combination of contact and bulk stresses, crack propagation

due to bulk stresses only, and fracture. Region I is where the crack initiates. Following initiation, crack will penetrate in the material at an angle and will propagate into the sub-surface when the stress state is sufficient to allow it. Region II depicts the propagation stage, where the damage is still considered a short crack. As the crack progresses deeper into the material, contact stresses reduce making the angle eventually turn to propagate in the direction normal to the axial stress. Region III is where the crack propagates due to bulk stress. Once that direction is undertaken, the crack progresses via mode I fracture until rupture. Region IV is the zone for catastrophic failure which occurs when the stress intensity factor, ΔK_{IC}, is reached or the crack reaches the outer edge of the part.

1.2 Relevance on Nickel Alloy

Many studies have been conducted to better understand the fretting phenomenon and its mechanisms, but only a few have been performed on nickel-based alloys. This superalloy is considered one of the most important material constituents in the core of the land based and aeronautical turbine [34]. Even though the main use of nickel has been as an alloying agent for ferrous metals, nickel as a main constituent forms many alloys that have a very wide range of outstanding properties [16]. Nickel alloys are known to have very low thermal expansion coefficients and almost constant elastic moduli over limited ranges of temperature. It also has excellent magnetic properties, but only at low magnetic induction. Nowadays, the need for the use of high-strength nickel-based superalloys in turbojet engines has motivated the strive to better understand the behavior of these materials under fretting fatigue. Due to the hostile environment in the turbine where the materials are operating, linear elastic fracture mechanics (LEFM) cannot directly be applied to predict the service life of engine parts. Due to their optimum creep, fracture and thermo-mechanical properties in comparison with the other cast alloys, these superalloys can tolerate the combination of multiaxial stress, high temperature gradient and the imposed loadings. Therefore, nickel-base alloys are the typical materials in use for the hot sections of the engines,

starting with the rear stages of the gas turbine engines which are too hot for titanium based alloys. For disc applications, these materials are used for high static and dynamic strengths' properties at temperatures below 750^oC. The material for this study is IN100, which is an advanced fine-grained nickel-base alloy utilized both in the turbine discs and the turbine blades of the gas turbine engines [9].

1.3 Contributing Factors

Fretting is a specific type of contact fatigue which consists of repetitive sliding between the two mating surfaces with a cyclic amplitude ranging between 5 and 50 μm. However, since the sliding is confined to tiny regions near the edge of contact with a stick region at the center of contact, this is usually described as partial-slip. The contact mechanics of fretting make it a very complex process involving the effects of normal load, bulk stress, shear tangential stress, relative slip, coefficient of friction and the contact geometry. Such a combination of parameters affects the relative displacement and the local stresses on a microscopic level, resulting in areas of relatively high stress concentration. It is a well documented fact that the parameters contributing to fretting fatigue are numerous, perhaps as many as fifty. However, the major factors investigated in the literature are the contact pressure, the magnitude of the slip, the peak pressure between the rubbing components, the contact semi-width, and the cyclic stress amplitudes. To isolate the effect of each single variable is a difficult task, if not an impossible endeavor. Many studies are to be undertaken in order to encompass all of them. This paper addresses fretting fatigue as it pertains to polycrystalline nickel-base alloy IN-100, and discusses the effect of the contact geometry, i.e. radius of a cylindrical pad on it.

1.4 Purpose and Objectives

Many fretting fatigue factors affect the service life of a component. Such variables either influence the process directly or indirectly, to a certain unknown degree. This investigation focuses first on the effect of the fretting on the fatigue life of a spec-

imen. Secondly, an attempt is made at understanding the behavior of nickel-based alloy under fretting fatigue at room temperature as a first step in understanding the overall behavior of the superalloy. In effect, this study is to provide the datum information that will allow researchers in the future to further investigate the fretting fatigue behavior of nickel under more complex conditions, starting with elevated temperatures. Finally, this study attempts to measure the effect of increasing the contact area on the fretting fatigue behavior by changing the radius of the cylindrical pad.

1.5 Methodology

Replicating the exact existing component geometry and loading conditions in the turbine engines is a complex, time consuming and mostly expensive process. Therefore, to conduct the fretting fatigue behavior of the nickel-based alloy and isolate the main ingredient of the problem at hand, a simplified cylinder-on-flat model was adopted for the experimental setup of this study as illustrated in Fig. 1.2. This figure shows the two bodies of interest; the IN100 specimen and fretting pad as a representation of any two components in contact. A uni-axial servo-hydraulic machine was utilized to apply a range of cyclic load conditions and record the experimental outputs. Gripped at the top, the specimen is subjected to an axial load, σ_{axial}, at the bottom end. Simultaneously, the pads are pressed against the specimen by a contact load, P, applied to the cylindrical ends of the pads by springs, in the direction normal to the applied bulk stress. The fatigue life diagrams (S-N curves) were established for two different cylindrical pad radii (50.8 mm and 304.8 mm) in order to characterize the fretting fatigue behavior of IN100 specimens. Thanks to the elasticity of the material, the specimen expands and contracts as the axial load is cycled through. In parallel, the pads remain fixed by a fretting fixture and in contact with the specimen through the load P. As a result, a shear load, Q, develops in the direction tangential to the bulk stress provided that the friction between the two bodies is large enough to prevent gross slip. The shear load is determined based on the difference between the applied axial load and the other force experienced at the gripped end of the specimen

through load cells placed at both ends of the specimen. To investigate the fracture surface, contact half-width, crack initiation location, crack initiation orientation, the Optical and scanning electron microscopy (SEM) is used. Finite element analysis (FEA) is undertaken to compute local fretting variables from the stress, strain, and displacement in the contact region and relate them to the experimental findings.

A secondary goal of this work is to evaluate whether any of the predictive fatigue crack initiation parameters that will be discussed in Chapter II including the Modified Shear Stress Range (MSSR) can predict within reasonable accuracy the number of cycles before failure caused by fretting. For other superalloys such as Ti-4V-4Al, the MSSR is known to work well for such a purpose. All predictive fretting fatigue parameters discussed in Chapter II are calculated for each experiment along the contact surface based on the stress state. The parameters' evaluations are based on estimating crack initiation location, orientation and the number of cycles to failure.

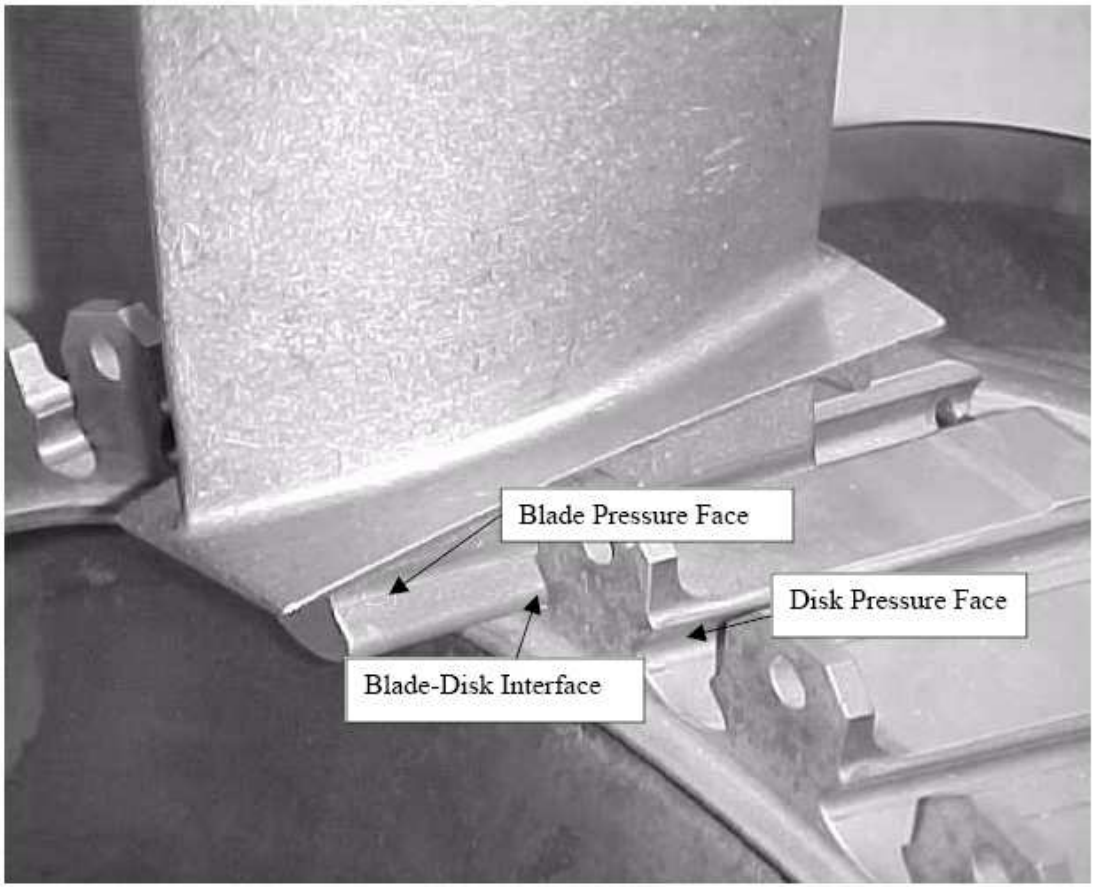

Figure 1.1: Turbine Engine dovetail Joint Interface

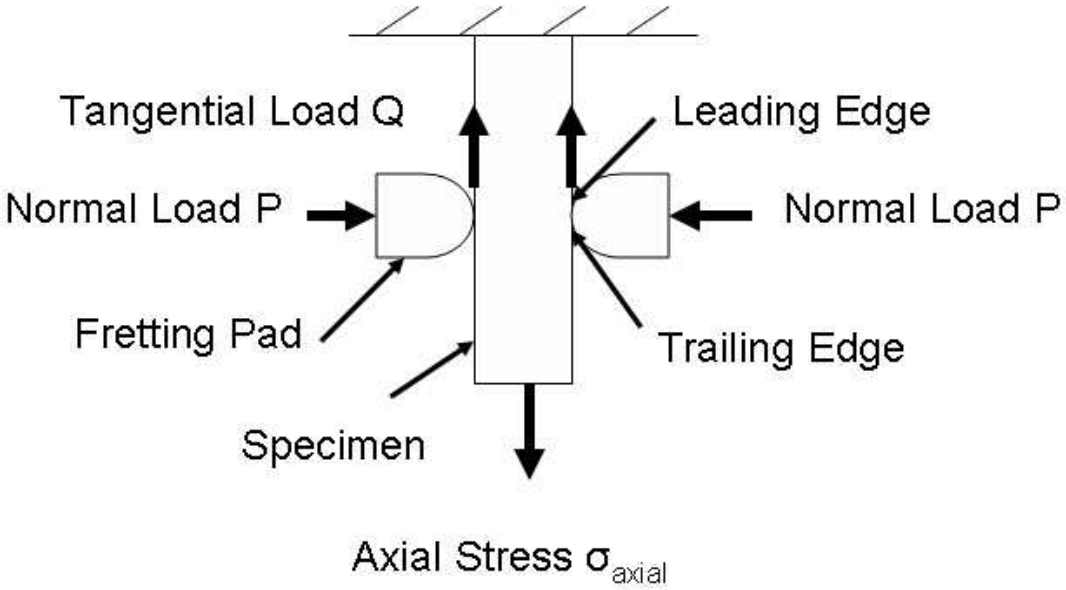

Figure 1.2: Fretting Fixture Adopted in The Present Study

II. Background

This chapter will provide a basis for the remainder of this work by reviewing fundamental concepts of fretting fatigue developed and tested on alloys and materials other than nickel-based superalloys. First contact mechanics will be addressed and discussed. Second, parameters which help to predict the fretting fatigue life are enumerated and explained. In addition, the author goes over the crack initiation process and the mechanisms behind it. Then, analytical techniques used to validate the experimental findings are introduced. Finally, the study attempts to explain how all the theories discussed are related to the present alloy IN-100.

2.1 Contact Mechanics

For the purpose of understanding the different variables involved, it is useful to look at a 2-D picture of the experimental setup depicted in Fig. 2.1. As shown, a cylindrical-end body in contact with a flat body setup is adopted as the fretting fatigue configuration. The specimen is represented by the rectangular shape in the middle while the two rounded bodies on the two sides of the specimen are the fretting pads. A represents the cross sectional area of the specimen, σ_{axial} denotes the applied axial stress, P corresponds to the contact load, Q is the resulting tangential load, b indicates half thickness of a specimen, d is the specimen thickness, while a represents the contact half width. The fretting pads have a constant radius r in the cross sectional plane, and since the specimen is flat, the radius of the fretting fatigue specimen is considered infinite in the cross sectional plane. The length of the contact area, when the normal load is applied, is known as the contact width, 2a. Half of the contact width is the contact semi-width, a. The rubbing effect, which is an important factor in fretting, takes place as the substrate is stretched and relaxes back to initial state. As the specimen is stretched due to the bulk stress, it moves relative to the pads which are pressed against it. The presence of friction between the pads and the specimen results in the development of the above-mentioned surface shear force, Q.

To explain fretting fatigue process, Sakata [29] from Japan related fracture mechanics in his analysis using the Stress Intensity Factor calculated from the stress distribution at the crack tip growing from the contact edges. The stress distribution is based upon the boundary element method program that was specifically tailored for these kinds of contact problems. In his work, he compared the program results to the Stress Intensity Factor threshold of the material at question. He concluded that the results were in good agreement with the previous experimental tests. In another study, Hattori [13], through the analysis of the fretting fatigues characteristics, suggested an estimation of the fretting fatigue strength based on the Stress Intensity Factor at the tip of cracks in the contact area. His calculations were based on the contact pressure and tangential stress distribution. Mingjian [22] devised a method to predict the fretting damage and the crack location at the contact region, in a dovetail joint specimen. It was possible thereby to determine the stress and temperature fields in the area of contact and to estimate the stick and slip dimensions as well as the energy consumed for friction. Szolwinski [35] also proved through other works that the critical location for crack development is at the trailing edge of the contact zone.

Specific to fretting fatigue is the development of distinct regions visible to the naked eye in the contact area. There are many studies in the literature that have defined three zones within the contact width, 2a. The central area is where the pad and specimen stick together. As such this area is called the stick zone, 2c. Right next to the stick zone on both sides, slip of the contacting bodies relative to each other is known to occur. Hence these two areas are called the slip zones. The amount of slip that takes place between the specimen and the pads is known as the micro slip range. No contact beyond the slip zones is occurring between the two contact bodies.

Moreover, Hattori [12] came out with a way to estimate the initiation of fretting fatigue crack based on the stress singularity parameters at contact edges. For the propagation part, he used fracture mechanics analysis to estimate the corresponding behavior. He demonstrated that cracks do initiate early in the fretting fatigue life, and that propagation process of these small initiated cracks dominates the fretting

fatigue life. Therefore, it is essential to be able to characterize and predict the crack initiation and propagation during fretting fatigue. As for the frequency of the applied cyclic load, Iyer et al. [15] revealed that increasing the contact pressure reduces life at 1 Hz but does not have any effect at 200 Hz.

Adibnazari [1] supports the existence of a normal pressure threshold, after which increasing the pressure does not affect the part service life. Below that limit, fretting fatigue failure depends on frictional stress and the change of frictional stress. However, beyond that point, failure was only a function of normal pressure and frictional stress and not their change. He also argued the existence of a critical frictional stress that makes the fretting damage reach its threshold faster. On the other hand, Szolwinski and Farris [36] showed interest in the effect of the subsurface stress field on crack initiation and propagation, as a result of the three-dimensional fretting contact. His study used the assumption that crack initiation is controlled by the effective stress in the Von Mises yield criterion which made it possible to predict the effect of normal and tangential loads as well as the coefficient of friction on crack initiation. It was found that the coefficient of friction and the tangential load have a crucial impact on the tensile stress at the contact edge.

To follow is a discussion of the contact mechanics and analytical solution associated with the cylinder on flat configuration adopted in this study of fretting fatigue behavior. The solution is obtained by solving a set of equations governing the displacements of two bodies in contact, which are assumed to have infinite boundaries. Figure 2.1 represents a diagram of two bodies in contact under fretting fatigue, where σ_{axial} is the applied axial stress, P is the applied normal load, Q is the tangential load, A is the cross sectional area of the specimen, a is the contact half-width, b is the specimen's half thickness and r is the fretting pad radius. In this study, two different radii are used: 50.8 mm and 304.8 mm. Assuming that given points in the contact zone are displaced in the y-direction by v1(x)-v2(x) and with reference to the displacement relationship developed by Hills and Nowell [14], the relationships in the contact region is as follows:

$$\frac{1}{A*}\frac{\delta h(x)}{\delta x} = \frac{1}{\pi}\int \frac{p(\zeta)}{x-\zeta}d\zeta - \beta q(x) \tag{2.1}$$

where h(x)=v1(x)-v2(x) is the amount of overlap that would occur if the contacting bodies could penetrate each other freely, q is the surface shear stress and p is the pressure in the contact zone, while the rest of the equation parameters are defined as below:

$$A* = 2(\frac{1-\nu_1^2}{E_1} + \frac{1-\nu_2^2}{E_2}) \tag{2.2}$$

$$\beta = \frac{1}{2A*}(\frac{1-2\nu_1}{E_1} - \frac{1-2\nu_2}{E_2}) \tag{2.3}$$

where E is the Modulus of Elasticity and ν is the Poisson's Ratio for the contact bodies, respectively. Based on the premise that the tangential displacement can be defined by:

$$g(x) = u_1(x) - u_2(x) \tag{2.4}$$

A similar equation is obtained as follows:

$$\frac{1}{A*}\frac{\delta g(x)}{\delta x} = \frac{1}{\pi}\int \frac{q(\zeta)}{x-\zeta}d\zeta - \beta p(x) \tag{2.5}$$

In this study, $\beta = 0$ since the contact bodies are made of the same material, thus equations2.1 and2.5 can be further simplified. When fretting begins between the contacting bodies after application of the normal load, P, the displacement of adjoining points in the stick zone on the contact surface will be exactly the same. At the same time, a certain pressure distribution, p(x,y), will be introduced by the contact load. As a result, the pressure distribution from the contact load is Hertzian:

$$p(x) = p_0 * \sqrt{1-(\frac{x}{a})^2} \tag{2.6}$$

where p_0 is the peak pressure which is given by either of the two following formulas assuming that the materials in contact are elastically similar:

$$p_0 = \frac{2 * P}{\pi * a} \tag{2.7}$$

$$p_0 = \sqrt{\frac{P * E}{2 * \pi * (1 - \nu^2) * R}} \tag{2.8}$$

To calculate the contact half-width, a, the following equation is used:

$$P = \frac{(\pi * k * a^2)}{2A*} \tag{2.9}$$

where k is termed the radius of curvature, such that:

$$k = \frac{1}{R_1} + \frac{1}{R_2} \tag{2.10}$$

where R_1 and R_2 are the radii of fretting pad and specimen, respectively.

Moreover, σ_{xx}, the axial stress resulting from the applied contact load P can be expressed in Cartesian coordinates as:

$$\sigma_{xx} = -p_0(\frac{\sqrt{a^2 - x^2}}{a}) \tag{2.11}$$

Also, q, the shear stress distribution along the contact surface can be expressed as:

$$q(x) = \frac{C}{\sqrt{a^2 - x^2}} \tag{2.12}$$

where C=Q/π, Q, being the total shear stress along the contact length which can be calculated by integrating the shear stress distribution as:

$$Q = \frac{f p_0 \pi}{2a}(a^2 - c^2) \tag{2.13}$$

The stick zone size can be obtained as below:

$$(\frac{c}{a} = \sqrt{(}1 - |\frac{Q}{fP}|) \tag{2.14}$$

Chan and Lee [7] wrote a FORTRAN program named "Ruiz program" to calculate the numerical solutions required by analytical analysis for variables such as Hertzian Peak Pressure in Equation 2.7, contact half-width in Equation 2.9, σ_{xx} in Equation 2.11, and so forth. These solutions from both analytical equations and Ruiz program are computed to verify the finite element model used in this study and then are compared to experimental results, which will be discussed in Chapter III. It should be noted that finite element analysis, FEA, is necessary for the cylinder-on-flat configuration, due to the fact that ratio of the thickness of the fretting fatigue specimen to the contact half width is less than 10. Therefore, FEA represents an alternative solution to this shortcoming in the analytical analysis, as will be further developed in Chapter IV. Finite element analysis will be used to calculate the governing parameters along the contact surface, such as stress, strain and displacement. These results will be later on used to determine the predictive fretting fatigue parameters.

2.2 Predictive Fretting Fatigue Parameters

Researchers, through time, came to recognize predictive parameters that are developed on the basis of stress or strain history of the plain fatigue configuration. These techniques have been extended to fretting fatigue data. Such analysis is of paramount importance since if one can predict accurately the crack location, crack initiation angle, and the fatigue life until crack initiation, the danger of unexpected failures can be greatly reduced. In addition, these parameters will also help engineers design components with enhanced resistance to fretting fatigue. Since the following parameters are known to forecast many details about fretting fatigue life in alloys, they are used in this study on IN-100 to verify which of them can be extended to nickel-base superalloys.

2.2.1 Critical Plane. In fretting fatigue, crack initiation and nucleation take place in the contact region where the state of stress is multiaxial by nature. One of the most important predictive parameters are the stresses occurring at the critical plane. The critical plane models are based on the premise that crack initiates on a particular plane, called the critical plane. It has been hypothesized that on that plane, normal stress opens cracks that reduces the friction between the crack surfaces and shear stress inducing dislocation movement along slip lines, and causing nucleation and growth of cracks. As such, the approach goes about finding the maximum shear strain amplitude and the plane on which it acts and then using the maximum normal stress on this plane to determine the effect of a mean stress. In a recent study, Namjoshi et al. [24] argued that the initiation of a fretting crack is a function of the shear stress on the critical plane and that the fretting fatigue life is influenced by the normal stress acting upon the same plane. It is mostly recommended by researchers in the field of fretting fatigue due to the multi-axial nature of the stress state developing at the contact region. It has been proven on Ti-6Al-4V that this method has the advantage of predicting crack orientation and could provide an accurate estimate of the crack size. The only difficulty is to measure these stresses experimentally. Therefore, test simulations are used based on a combination of analytical solutions and FEA output data to determine such parameters.

With regards to the tests conducted in this work, the following fretting fatigue parameters were investigated:

2.2.2 Findley Parameter. Originally created in the 1960's, the Findley Parameter, FP, was used first for plain fatigue analysis. It takes into account both the shear stress amplitude and the maximum stress normal to the orientation of the maximum shear plane. In effect, Findley [10] suggested the use of a multiaxial fatigue parameter to predict fretting fatigue behavior in the following manner:

$$FP = \tau_a + K\sigma_{max} \tag{2.15}$$

where τ_a is the shear stress average, σ_{max} is the maximum stress normal to the orientation of maximum shear plane and K is an influence factor (K=0.35) found from plain fatigue data, and

$$\tau_a = (\tau_{max} - \tau_{min})/2 \tag{2.16}$$

where σ_{min} is the minimum stress normal to the orientation of shear stress plane. The parameter is determined, on all planes from $-\pi/2 \leq \theta \leq \pi/2$ in increments of 0.1^o. These calculations provide the critical plane where this parameter is the maximum.

2.2.3 Smith-Watson-Topper (SWT) Parameter. This parameter was first based on the total strain amplitude calculated as follows:

$$\epsilon_a = \frac{\sigma_f^{'}}{E} 2N_i^{b'} + \epsilon_f^{'} * 2N_i^{c'} \tag{2.17}$$

where $\sigma_f^{'}$ is the fatigue strength coefficient, N_i is the number of cycles to crack initiation, ϵ_a is the , $\epsilon_f^{'}$ is the fatigue ductility coefficient, b' and c' are constants. Equation 2.17, usually referred to as the strain life equation, was modified by Smith and al. [31] as to include the effects of fatigue data tested at different strain ratios. They were able to prove that plain fatigue data generated at different strain ratios could be collapsed on to the fully reversed, R=-1.0, fatigue curve. The new formula is as follows:

$$\Gamma = \sigma_{max}\epsilon_a = \frac{(\sigma_f^{'})^2}{E}(2N_i^{2b'} + \sigma_f^{'}\epsilon_f^{'}(2N_i)^{b'+c'} \tag{2.18}$$

Equation 2.17 is commonly referred to as the Smith-Watson-Topper (SWT) parameter. Later on, Socie [32] modified it to make the parameter multiaxial, by making the the left hand side of Equation 2.18 represent the maximum principal strain amplitude and the maximum principal stress. It was later altered by Szolwinski and Farris [36] in order to be applied to fretting fatigue crack initiation [37]. The modified parameter assumes crack initiates on the plane where the product of normal strain amplitude ϵ_a and maximum normal stress, σ_{max} is maximum. The parameter, defined as $\Gamma = \sigma_{max}\epsilon_a$, has worked in predicting the crack initiation location and

orientation for other alloys. To calculate this parameter, the FEA calculated stresses and strains are used. Using this concept, the critical plane is assumed where the modified SWT parameter reaches its maximum. In this manner as the Findley parameter, this study calculates the SWT parameter in increments of 0.1^o at all planes ranging from $-\pi/2 \leq \theta \leq \pi/2$. In this version, SWT parameter has been used effectively to predict fatigue life in steels and aluminum alloys under the multi-axial fatigue loading condition [17]. However, several authors have demonstrated that γ parameter was also able to predict accurately the cycles to crack initiation [35], [38], [39].

2.2.4 Shear Stress Range (SSR) Parameter. The stress range is affected by local interfacial mechanistic parameters such as peak contact pressure, local bulk stress, local shear stress, slip amplitude and contact semi-width Iyer et al. [15]. Stress range can be determined as follows:

$$\Delta\tau = \tau_{max} - \tau_{min} \tag{2.19}$$

where τ_{max} and τ_{min} are the shear stress values due to the application of the maximum and minimum axial loadings. To find the stress range, the maximum shear stress range is determined on all planes ranging from $-\pi/2 \leq \theta \leq \pi/2$ as follows:

$$\tau|\theta = \frac{-(\sigma_{xx} - \sigma_{yy})}{2} sin2\theta + \tau * cos2\theta \tag{2.20}$$

where σ_{yy} is the normal stress along the y-direction. However, this equation does not take into account the effect of mean stress nor that of stress ratio, which are well documented in fatigue literature to be relevant to fatigue strength. On the other hand, Walker [40] came up with an alternative method to include those effects as follows:

$$SSR = \Delta\tau_{crit} = \tau_{max}(1 - R_\tau)^m \tag{2.21}$$

where m is the fitting parameter chosen to collapse plain fatigue crack initiation data at different strain ratios and R_τ is the stress ratio on the critical plane as below:

$$R_\tau = \frac{\tau_{min}}{\tau_{max}} \tag{2.22}$$

. m is determined to be 0.45 by Lykins [8].

An accurate critical plane fatigue parameter formulated as described above is able to predict fatigue life, crack initiation location, and crack initiation orientation. The SSR parameter is calculated in this study to examine its applicability to IN-100.

2.2.5 Modified Shear Stress Range Parameter (MSSR). MSSR is considered by many researchers in the field to be the premier predictive parameters of fretting fatigue behavior. It is simply a modified version of the SSR parameter to make it include the effect of maximum normal stress, which generally acts in opening the crack surface. As such, it is known to eliminate the effect of pad geometry. MSSR is calculated as follows:

$$MSSR = A\Delta\tau_{crit}^{B} + C\sigma_{max}^{D} \tag{2.23}$$

where $\Delta\tau_{crit}$, A, B, C and D are constants determined by curve fitting to be 0.75, 0.5, 0.75, and 0.5 respectively for Ti-6Al-4V [28]. Just like SSR, MSSR is calculated at all planes ranging from $-\pi/2 \leq \theta \leq \pi/2$ using the stress data obtained from FEA analysis at every point along the contact length. The critical plane is the plane where MSSR attains its maximum.

For Ti-6Al-4V, Namjoshi et al. [25] showed that MSSR, showed very little dependence on pad geometry. He found that this parameter may be used, in conjunction with an analysis, to predict fretting fatigue life from plain fatigue life data. It was his argument that accuracy of this parameter was due to taking into consideration both the effect of shear stress as well as normal stress in the case of multiaxial fatigue loading condition. In this study, MSSR is calculated in order to measure its ability, as

a fretting fatigue parameter, to predict fatigue life, crack location and crack initiation orientation of IN-100.

2.3 Crack Initiation Mechanism

In previous studies, it has been demonstrated that the primary crack, which causes failure in the specimen, always initiated near the trailing edge on the contact surface, although there is usually some smaller secondary cracks that do not grow enough to develop further to cause failure. The initiation angles are $\pm 45^o \pm 15^o$ from a perpendicular to the axial loading direction. Also, maximum shear stress range can occur on two planes orthogonal to each other, one in the positive quadrant and the other in the negative one. Hence, for every state of stress, there are two critical shear stress planes with equal possibility of crack orientation. Only local microstructure property may make one plane preferred over the other. It has been observed by researchers that fatigue crack initiated and propagated in inter-granular manner under fretting fatigue conditions. In effect, grain boundaries are not the preferred location or direction for crack development. Moreover, crack behavior is found to be independent of pad geometry and fretting load conditions.

2.4 Analytical Model

To validate any computational model accomplished through FEA, analytical solutions can be used to verify the accuracy of its respective results. For this purpose, Chan and Lee [7] developed a FORTRAN program named "Ruiz program" to calculate variables such as Hertzian Peak Pressure and contact half-width. The program allows also the estimation of the stress state at every location along the contact length and its comparison with the output data from the FEA model used in this study. Furthermore, Ruiz suggested the use of K_2 parameter to predict the fretting fatigue initiation location. This parameter combines the effect of the surface tangential stress,

shear stress and the relative slip at the interface. To calculate K_2:

$$K_2 = (\sigma_T \tau \delta)_{max} \tag{2.24}$$

In addition, Ruiz proposed another parameter, K_1 that takes into account the maximum frictional work as well, as follows:

$$K_1 = (\sigma_T)_{max}(\tau \delta)_{max} \tag{2.25}$$

These parameters combined collapse the crack initiation process into one criterion; based on the premise that frictional work is the mechanism that nucleates cracks whilst the maximum tangential stress is the process responsible for opening and propagating those cracks.

2.5 Gross slip and Partial slip

In general, when a fretting fatigue process starts, the two mating bodies experience slip, long before a stick zone is formed. Under this condition, the pads and specimen are relatively free to slip against each other. Over time, fretting either turns into gross slip or partial slip condition. Gross slip occurs when the two contacting surfaces are in full sliding mode across the contact zone during a portion of the cyclic loading, and the resulting damage is called fretting wear. On the other hand, partial slip is identified when no gross relative displacement is observed but only small slip zones exist near the edges of contact. In the center of contact, the substrate and the pads are welding together. Another possible mode is a combination of gross and slip conditions. This may be the result of a low coefficient of friction. Overall, Fig. 2.2 shows the two regions ideally distinguished.

2.6 Previous Studies on Nickel-based Alloys

Extensive research has been done on other polycrystalline alloys and especially titanium. Very few studies were found in the literature about nickel-based superalloys

in the area of fretting fatigue. For instance, Wan [41] studied the low-cycle fatigue (LCF) behavior of smooth and notched specimens of nickel-based single-crystal DD3 superalloys at 620^o. The study, developed a model based on experimental results and FEA analysis, takes into consideration the mean stress effect and adopts the crystallographic theory as a basis. This theory is based on the relationship between the resolved shear stress and resolved shear strain of the activated slip systems. For the smooth round specimens, these two variables are calculated as follows:

$$\tau^{\alpha} = \sigma : P(\alpha) \tag{2.26}$$

where α is the resolved shear stress of slip system, P^{α} is obtained from

$$P(\alpha) = 0.5(m^{\alpha}n^{\alpha^T} + n^{\alpha}m^{\alpha^T}) \tag{2.27}$$

where n^{α} and m^{α} are unit vectors normal to the slip plane and along the slip direction of the slip system (α), respectively. The following power-law life model was assumed for the DD3 superalloys:

$$\frac{\Delta\tau_{max}}{2} = AN_f^b \tag{2.28}$$

where $\Delta\tau_{max}/2$ is maximum resolved shear stress amplitude of all activated slip systems, A and b are parameters and N_f is fatigue life. Equation2.28 is valid only for zero mean stress. In order to consider mean stress effect, Equation2.28 is modified as below:

$$\frac{\Delta\tau_{max}}{2} = AN_f^b 1 - (\frac{\tau_m}{\tau_b})^2 \tag{2.29}$$

where τ_m is the mean resolved shear stress on the slip system corresponding to maximum shear stress, and τ_b is the resolved shear stress corresponding to the ultimate tensile strength.

In a work done by Shyam [30], he developed a theoretical model for slip irreversibility in a polycrystalline nickel-base superalloy which deforms in a planar manner. The slip irreversibility parameter was based on the fraction of dislocations

exiting the free surface due to the applied loading. According to this definition, the slip irreversibility parameter has the values between zero, corresponding to reversible slip and one, which denotes fully irreversible slip. After comparing the theoretical calculations with the experimental observations of slip offsets due to a single stroke compression test, it was found that slip irreversibility increased with temperature. Therefore, Shyam claimed that slip irreversibility variation with temperature causes the observed decrease in fatigue crack propagation threshold values with increasing temperature. Using the SEM, it was observed that nickel-base single crystal superalloys deformed by slip on crystallographic planes. It was also shown that the fracture surface coincided with the octahedral slip system (1 1 1)[0 1 1]. He concluded that activation and movement of slip systems are the basic deformation mechanism of notched and round specimens like smooth round specimens.

In another study, Brien and Decamps [6] tested the microstructural characteristics of another single crystal nickel based superalloy (AM1) under high temperature fatigue at 950^o. For repeated fatigue ($R_e = 0$), two types of behavior were found depending on N, the number of cycles and $\Delta\epsilon^t$, allowing a map of microstructures versus the N and $\Delta\epsilon^t$ to be developed. A domain called A shows anistropic microstructures due either to a partition of the plasticity throughout the γ channels, or to an oriented coarsening of the $\gamma^{'}$ precipitates of the so-called type B (raft orthogonal to the loading direction). The H domain presents homogeneous deformation microstructures. The presence of the precipitates significantly affects the usual behavior of monocrystalline alloys under fatigue and localizes the plastic deformation in the channels. In addition, Brien and Decamps claim that there is a geometrical differentiation of plasticity due to heterogeneity of the local stress resulting from the presence of internal stresses. Further, alternate fatigue ($R_e = -1$) also leads to the same type of coarsening, even for very low cycle numbers. It was shown that alternate fatigue causes a three-dimensional distribution of the plastic deformation in the γ channels, since tension activates plastic flow in the channels perpendicular to [001] and compression in the others.

Moreover, Piard et al. [27] simulated creep-fatigue crack growth in PM nickel-base superalloy, at 750^o under high vacuum, based on different cohesive models and experimental data. Although creep effects play an important role, he focused on the small ΔK range where crack propagation occurs during the reloading phase only. He undertook two simulations, one with a hold time and one without it. Based on the introduction of damage fields describing fatigue and creep effects in the vicinity of crack tip, Piard et al. found that these damage fields are related to crack opening displacements. In addition, he showed that the predicted cracking curves accurately reflect the influence of hold time duration in the ΔK range where crack propagation takes place during the reloading phase only.

In another study accomplished by Sondhi et al. [33], he ascertained the presence of an internal stress field within IN-100 alloy which caused an unusual response of low and even negative creep rates in tension. His intent was to characterize the behavior of an as-received and pre-aged IN100 disc alloy so as to validate a previous hypothesis that the unusual response of low and even negative initial creep rates in tension is caused by the presence of an internal stress field within the alloy. He found that the absolute values of initial creep rates in compression to be significantly higher than in tension, resulting in an asymmetric creep response, which proves the presence of an internal compressive field internal stress. Comparison of tensile and compressive creep was consistent with plastic deformation being largely confined to the matrix where there is a compressive internal stress. This observed asymmetry was practically removed by thermal pre-ageing prior to creep. The simulation used a microstructure-based creep model incorporating an evolving internal stress field.

Finally, in a fretting fatigue work done on nickel alloy conducted by Murthy et al. [23], single crystal nickel SCN specimens and IN100 pads were tested under elevated temperature. Using a rig designed to operate at conditions representative of engine conditions, Murthy et al. found that the effect of orientation of the material principal axes on subsurface stresses is significant. The work postulates that the crystal orientations could be used to evaluate contact stresses, which in turn can be

utilized to estimate the life of the specimen. Using a co-ordinate measuring machine, the fracture plane was observed along [1 1 1] within a few degrees. Crack initiation was found to initiate at the edge of contact pad and dog-bone specimen. However, little effort was spent on understanding the contact mechanics of fretting fatigue in this study. Furthermore, no finite element analysis was conducted to understand the stress state in the contact area.

In summary, the previous works done on nickel-base superalloys are very limited. More importantly, the studies conducted on fretting fatigue of nickel base superalloys especially are not available as far as the author is aware. Moreover, these studies focused only on single crystal nickel based alloys, and even then, do not have the basic reference data on the behavior of the material under room temperature. Therefore, it is the intent of the author to characterize fretting fatigue behavior of polycrystalline nickel base superalloy, under room temperature before investigating it further under more complex environment conditions.

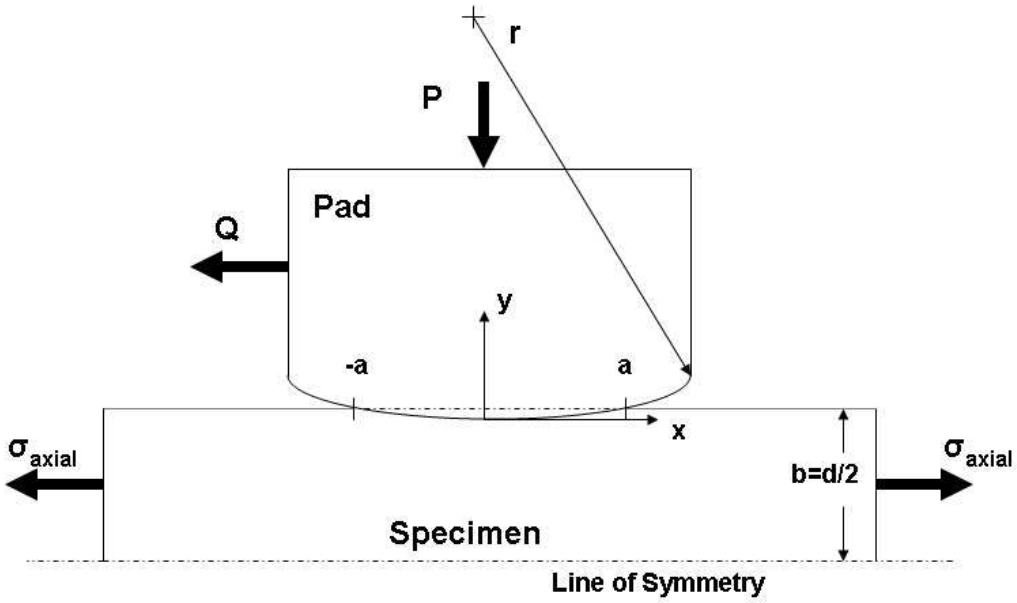

Figure 2.1: Diagram of Two Cylindrical-on-flat Bodies Under Fretting Fatigue

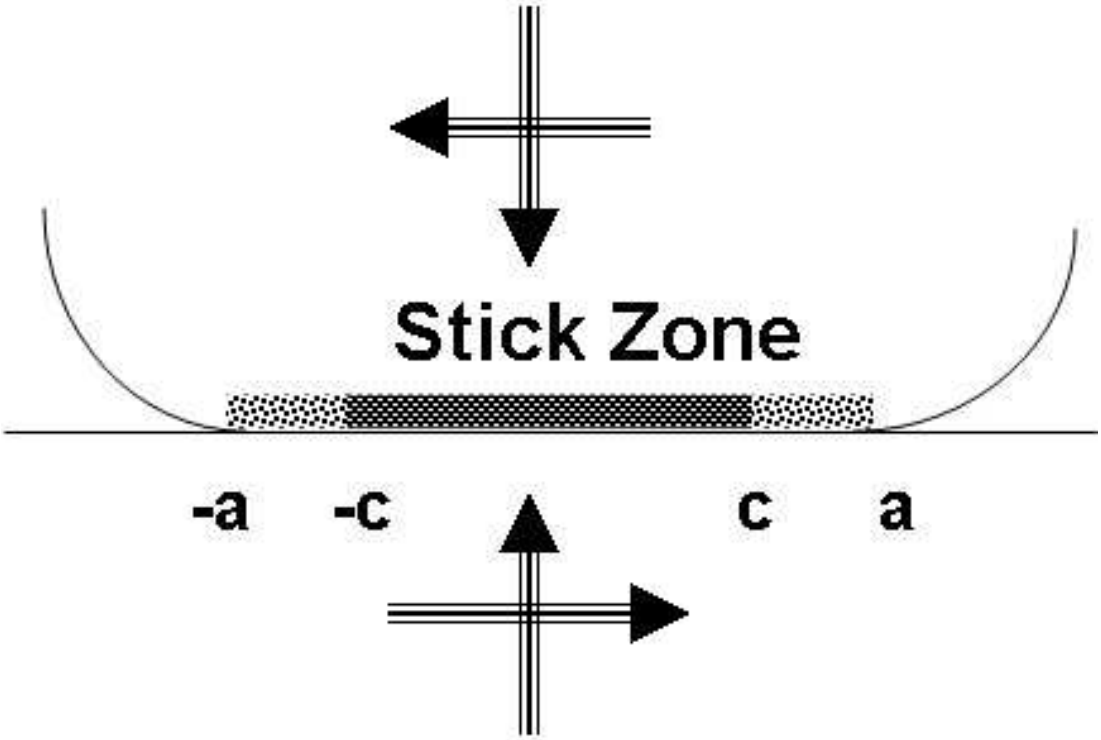

Figure 2.2: Diagram distinguishing the slip and stick zones

III. Experiments

This chapter documents the experimental procedure and setup used in this study to investigate the behavior of IN100 under fretting fatigue at room temperature with two cylindrical pad radii. Experiment test details such as test apparatus, specimen and pad geometry, material property, load determination, and test procedure are covered in this chapter.

3.1 Test Set-up

The experimental setup in this study uses a 22.2 kN servo-hydraulic uniaxial test machine. Figure 3.1 is a photograph showing the whole test machine. Figure 3.2 shows schematically the fretting fixture which is capable of keeping the normal load constant via lateral springs throughout the experiment. The axial load is controlled via the 22.2 kN servo-hydraulic load frame. The axial load variation that the test specimen undergoes during the test runs are measured by load cells attached to the servo-hydraulic load frame. This actuator is controlled by Multi-Purpose Test Software (MPT) which allows the user to choose the magnitude, frequency, and waveform of the applied axial load. During a load cycle, the contact pads undergo small relative movement with respect to the specimen, and in the process, cause fretting action on the face of the specimen. Therefore, alignment becomes of paramount concern, and must be checked prior to every experiment. Such task is not always easy to undertake, especially with the 304.8 mm which are particularly hard to align. It is a well known fact that the flatter the pads are, the more difficult they are to align. Since the contact area is larger for flatter pads, making the two pads on each side touch the specimen exactly at its center becomes tricky.

3.2 Specimen and Pad Geometry

The dimensions of the dog-bone shaped are as follows: specimen thickness of 3.81 mm, specimen width of 6.35 mm, cross sectional area of 24.194 mm^2 and a length of 127 mm, as shown in Fig. 3.3. Also displayed in the same figure are the two different

pads used, with an equivalent radii of 50.8 mm and 304.8 mm respectively at one end with flat-end at the other side. The thickness and the width of both types of pads are both 9.525 mm. Both pads and specimens are made up of cast IN100 nickel-base alloy, which is commonly used in turbine engine discs and blades. The measured grain size was about 100 μm. The material at hand has a modulus of elasticity of 126 GPa and ultimate tensile strength of up to 1520 MPa (at room temperature), and a Poisson's ratio of 0.28 (See Appendix A for more details). IN-100 is composed of (in %) Ni 60, Co 15, Cr 9.5, Al 5.5, Ti 4.75, Mo 3.0, V 0.95, Fe 0.20, Zr 0.06, W 0.04, Mn 0.01, Si 0.05, C 0.18, B 0.02 [4]. Both the dog-bone specimens and the pads are cut by the wire electrical discharge method. The displacement of the specimen is applied in the axial direction through the actuator in a cyclic fashion at a constant amplitude of 10 Hz. The shear load is a dependent variable of the bulk stress and the resistance from the pads caused by the lateral springs.

3.3 Experimental Configuration

A fretting fatigue apparatus is adopted to have control over most of the critical fretting fatigue variables. All the experiments were accomplished over a wide range of axial tension-tension loading condition at different stress levels ranging from 650 to 950 MPa, at a constant Stress Ratio of 0.03. On both sides of the specimen, a pair of pads is mounted into the fixture holding blocks. Prior to any test, the pads are first aligned to ensure pads' surfaces are in perpendicular contact with the specimen and transverse with the applied bulk stress. The pressure sensitive tape, put between specimen and pad, is used for this purpose. Then, the specimen is removed from the fixture, and a warm-up procedure programmed in MPT is executed for at least 30 minutes to ensure hydraulics are well functioning. This procedure is programmed using the displacement control for the axial load actuator. Once warmup done, the specimen is mounted and clamped into the test fixture through the upper and lower grips. At this moment, the normal load is applied manually via the lateral butterfly screws in increments of 111.2 N until the desired load of 4003 N is reached. After that,

lateral screws are tightened sufficiently to avoid vibration of the whole setup as the experiments starts. At this point, the control interface ensures gradual application of the axial load until the maximum σ_{axial} is achieved. The actuator cycles then in a periodic fashion (sinusoidal) between the maximum and minimum loads at the frequency of 10Hz, until failure of the specimen. To ensure that the experiments are not simple wear tests, the specimen is watched visually at the beginning and the end for any deposit of debris. During the experiments, peak-valley compensator (PVC) is activated for axial loads to reduce variation between command and feedback signals sensed by the test machine. Axial loads and tangential loads were recorded in parallel in time-steps of 0.04 seconds, in an output file. After a specimen fails, the number of fretting fatigue cycles were taken down as the specimen's fatigue life. A total of fourteen fatigue tests were conducted, ten of them under fretting fatigue fixture in order to determine the effect of fretting on the regular fatigue life of a part made out of IN-100, as shown in Table 3.1.

3.4 Load Determination

To be able to perform Finite Element Analysis (FEA) in Chapter IV, both the bulk and shear stress had to be determined. The maximum and minimum data sets are inputs to FEA. As previously noted, the axial load is measured through a load cell attached to the servo-hydraulic frame. Hence the tangential load can be calculated as follows: Q=$\frac{V-W}{2}$ where Q_{load} is the resulting tangential load on each side of the specimen, V is the axial load applied by the actuator at the lower end of the specimen, and W is the load applied at the upper end to grip the specimen. In this fashion, the tangential loads Q_{max} and Q_{min} corresponding to maximum and minimum σ_{axial} can be readily found after each test. Also, The change of the tangential load with respect to the applied load P, is looked at after each experiment to observe the hysteresis loops, where it is possible to discern the gross sliding from the partial sliding conditions. During the gross slip usually, after a small amount of cycles following test start for cylindrical pads, Q increases to a local maximum, and then decreases to an

asymptotic value, reaching the steady state condition. However, during partial slip stage, Q is considered stable with stabilized extremum, which are used in the FEA input data. In Fig. 3.4, typical hysteresis loops are illustrated for the stress level of 850 MPa. Gross sliding is where the larger loops are formed, which happens only during the first 100 cycles. When the circles start to shrink to almost a line, the test is said to have reached partial slip stage. Another check is also performed, which verifies that tangential loads are stabilized quickly after experiment beginning and remaining that way until the end of the test as depicted in Fig. 3.5.

3.5 Coefficient of Friction

The coefficient of friction, f, has to be determined for subsequent use in the finite element analysis, is expected to be different for each load condition. The applied contact loading conditions generally affect the coefficient of friction on a contact surface. It has been shown in previous studies, that the coefficient of friction stabilizes after about 1,000 to 2,000 cycles to a constant value [24]. In order to determine the coefficient of friction, the contact load was first applied onto the specimen by the fretting pads. Then, a monotonically increasing axial load was applied gradually to one end of the specimen, while the other end was kept free. The resulting tangential load was monitored and recorded continuously. The load is increased until gross slip between a specimen and pads is observed. The static coefficient of friction is then calculated as follows:

$$f = \frac{Q}{P} \tag{3.1}$$

The experimental stabilized f ranged from 0.35 to 0.45 for the 50.8 mm pads, and 0.3 to 0.39 for the 304.8 mm pads. Therefore, this study adopted a coefficient of friction of 0.45 as one of the FEA input variables.

In the next chapter, using part of the experimental results, FEA is conducted for each experiment, to correlate the experimental findings with the computational

predictions. In the next section, the procedure to determine crack initiation and measure crack orientation along the contact surface is provided.

3.6 Crack Location and Orientation

One of the fretting fatigue parameters that could be predicted is crack initiation location. It is a well documented fact in the literature, that the crack always initiates at or near the trailing edge of the contact, as confirmed by this study. For 50.8 mm pads, Fig. 3.6 clearly shows the crack location near the trailing edge of the broken part onto the left. The observed contact half-width is approximately 0.508 mm while the analytical solution predicted 0.602 mm (Ruiz Program). As for the 304.8 mm pads, the experimentally measured contact half-width is 1.288 mm whilst the Ruiz program predicts 1.476 mm.

Moreover, crack orientation is one of the important fretting fatigue features that can be predicted computationally. Using the SEM, the crack initiation zone is at first noted as the the area with discoloration on the failed specimen surface. Using the precision saw machine, the specimen is sectioned laterally along the x-axis as close as possible to the center of the estimated crack initiation zone. More material is shaved off until a clear SEM picture allows the investigation of the crack orientation.The polished specimens are placed in the SEM to evaluate the orientation of the crack along the contact surface.

The experimentally found angles and locations will be compared to the angles predicted through fretting fatigue parameters. The comparison is accomplished for both pad radii.

Figure 3.1: A Frontal View of The Test Machine Used in experiments

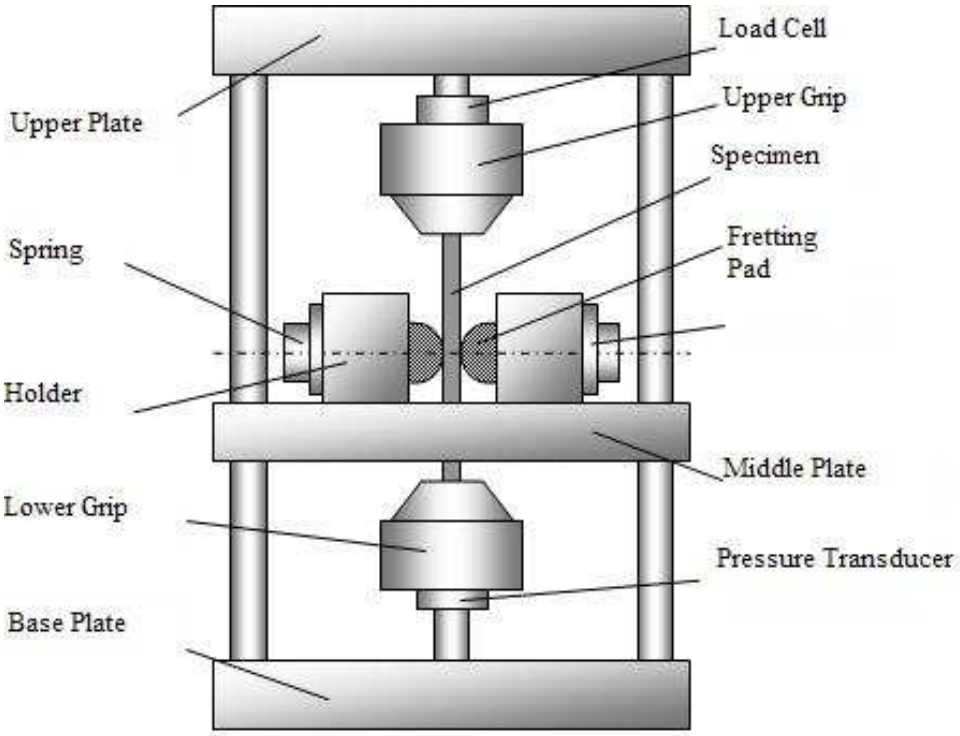

Figure 3.2: Fretting Fixture

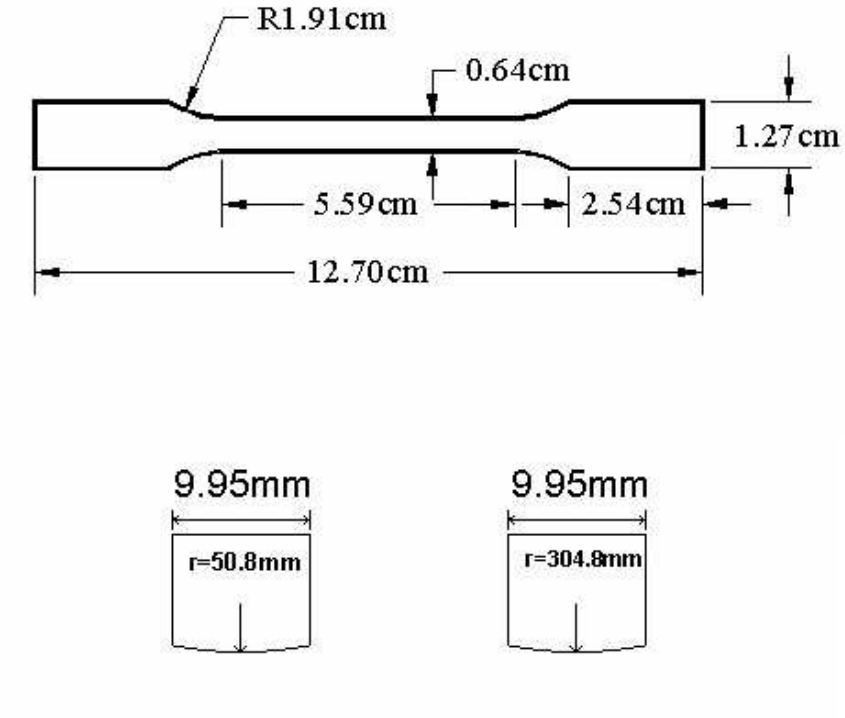

Figure 3.3: Dimensions of the Specimens and pads used

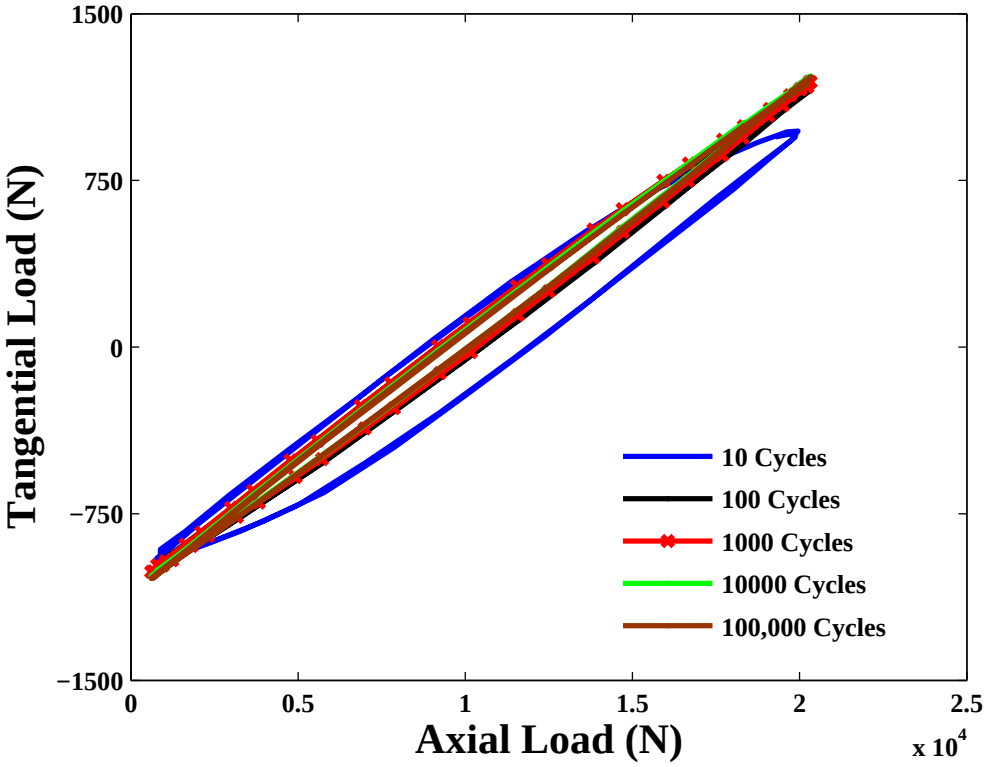

Figure 3.4: Hysteresis Loops for Test #4

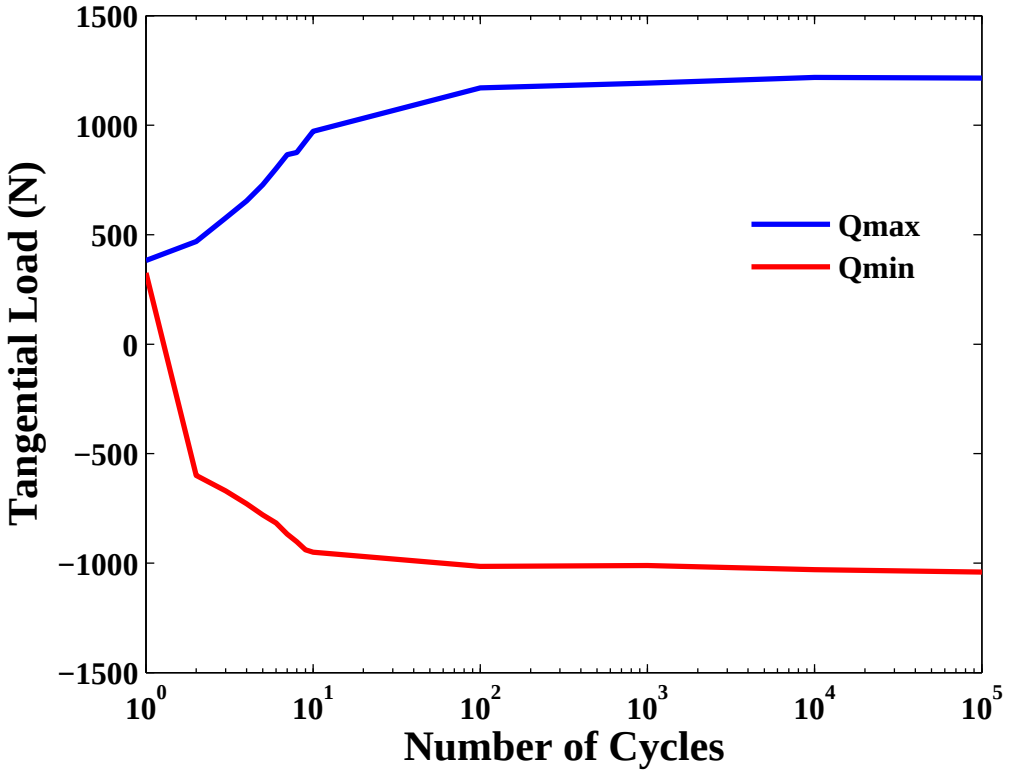

Figure 3.5: Tangential Load vs. Number of Cycles run for test #4

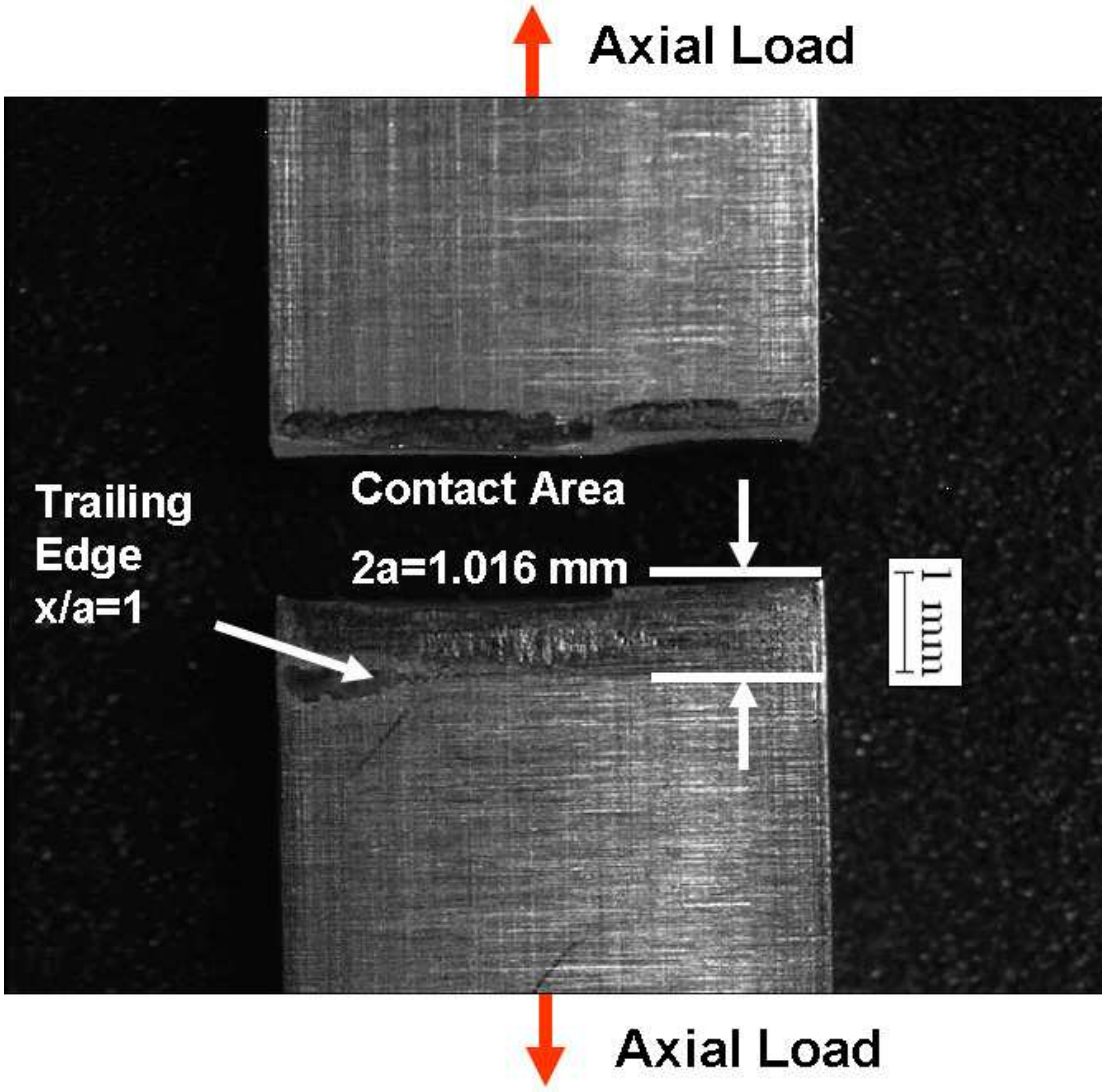

Figure 3.6: Scar View for test #2

Table 3.1: Experimental Test Settings

Test	Type	Pad	P	σ_{max}	σ_{min}	Δ_σ	σ_{eff}
		mm	N	(MPa)	(MPa)	(MPa)	(MPa)
1	Fretting Fatigue	50.8	4003	650	19.5	630.5	641.15
2	Fretting Fatigue	50.8	4003	750	22.5	727.5	739.79
3	Fretting Fatigue	50.8	4003	800	24	776	789.11
4	Fretting Fatigue	50.8	4003	850	25.5	824.5	838.43
5	Fretting Fatigue	50.8	4003	950	28.5	921.5	937.07
6	Fretting Fatigue	304.8	4003	650	19.5	500	641.15
7	Fretting Fatigue	304.8	4003	750	22.5	400	739.79
8	Fretting Fatigue	304.8	4003	800	24	351	789.11
9	Fretting Fatigue	304.8	4003	950	28.5	300	937.07
10	Plain Fatigue	-	-	885	26.55	858.45	846.76
11	Plain Fatigue	-	-	944	28.32	915.68	903.21
12	Plain Fatigue	-	-	1062	31.86	1030.14	1016.12
13	Plain Fatigue	-	-	1080	32.4	1047.60	1033.34

IV. Finite Element Analysis

In this chapter, FEA and fretting fatigue parameters are discussed. The requirement for FEA as well as a description of the model configuration is provided. FEA results are validated by comparison to the analytical solution.

4.1 Requirement of FEA

This work uses two cylindrical on flat configurations, each one with a cylindrical fretting pad for each radius, on a flat specimen. It has been noted in previous studies, that the size of the contact area between the two fretting bodies hinges upon the applied load. Since both the pads and the specimens are both elastically similar and made out of IN-100, according to the Hertz solution, a pressure distribution results.

To use the analytical techniques, the radii of pads and specimens are assumed large in comparison to the contact dimensions. Also the contacting bodies are assumed to have infinite boundaries. In this case, the latter assumption's basis, known as the half space assumption, is violated since half the specimen's thickness, b, is less than ten times the contact half width, a. The contact half width is determined as follows:

$$a^2 = \frac{2PA'}{k * \pi} \tag{4.1}$$

where P is the normal load distributed over the width of the specimen, and A', for the contact bodies, is given as:

$$A' = \frac{4(1-\nu^2)}{E} \tag{4.2}$$

where ν is the Poisson's Ratio, E is the Modulus of Elasticity and k is the radius of curvature such that:

$$k = \frac{1}{R1} + \frac{1}{R2} \tag{4.3}$$

where R1 is the radius of the fretting pad and R2 is the radius of the specimen. In this study, the pads have two constant radii; 50.8 mm and 304.8 mm, while the specimen is attributed an infinite radius.

Violation of the half space assumption has been proven to cause deviation from the expected analytical solution as related by Fellows [14]. Therefore, another technique, that does not rely on the half-space assumption, has to be used to validate our experimental findings, FEA.

4.2 Advantages of FEA

More than just providing a solution to the half space assumption violation, the use of finite element model provides several advantages over both the experimental and analytical solutions. First, FEA allows the researcher access to information otherwise not obtainable neither through experimental tests nor analytical solution. This computational analysis has the ability to determine the local parameters p_0, a, δ_{max},$\tau_{x,max}$, $\Delta\tau_{x,max}$, $\sigma_{x,max}$, $\Delta\sigma_{x,max}$ in the contact region utilizing only the boundary conditions including P, $\sigma_{xx,max}$, $\sigma_{xx,min}$ and the corresponding Q_{max} and Q_{min}. From local parameters, all the predictive parameters cited in Chapter II can be obtained. Moreover, FEA allows access to additional information about the experimental setup. For instance, Iyer et al. [15] has found, through FEA, that a tensile stress concentration results from merely applying the contact load on the specimen. In addition, Magaziner [20] noted that the contact semi-width is not symmetric about the center of contact. Therefore, FEA offers valuable benefits in the study of the fretting fatigue phenomenon.

4.3 FEA's Approach

The salient feature of FEA is to discretize a continuum body into a finite number of four-node plane strain quadrilateral elements to determine stress, strain and displacements magnitudes at the contact interface. The basis of FEA is to first formulate the n x n governing equations at the nodes which are discrete points that

make up the elements, and then solve the equations as well as any other unknown simultaneously to obtain the final solution. In other words, the elasticity problem is formulated by considering the potential energy of a continuous elastic system. This potential energy is then minimized to solve for the displacements. For the purpose of FEA, a commercially available software, ABAQUS, is used to model the contact analysis in this study. The contact conditions are simulated using the "master-slave" interfacial algorithm for contact modelling of the experimental configuration. The software creates contact points using anchor points on the master surface. It locates these anchor points by drawing a unit normal from the slave surface nodes to the master surface. The slave nodes are then required to deform relatively to the anchor points.

4.4 Model Description

This work uses two versions of the two-dimensional finite element model shown in Fig. 4.1 and 4.2, for the two pad radii configurations, 50.8 mm and 304.8 mm. The model consists of three main parts: fretting specimen, fretting pad and rigid body constraint as The master surface is the fretting pad and the slave one is the specimen. ABAQUS algorithm determines which segments on the master surface interact with which nodes on the slave surface. These master segment/slave node relationships are then used to establish the contact algorithm to determine how loads are transferred at the contact interface. The specimen is fixed at its far end in the negative x-direction, restricted from vertical movement at the bottom surface and only free to roll in the x-direction and along the gripped end. Thanks to the symmetry of the setup along the centerline of the specimen, only half of it is modelled using FEA. Hence the finite element model has a thickness of 1.905 mm. The specimen is represented as being 9.525 mm long in both directions of the center of contact. The cylindrical pad is rigidly fixed to the pad holder which in turn is free to roll in the y-direction. The fretting pad is constrained in the x and y direction by the rigid body constraint or pad holder while the half space of fretting specimen was constrained in the x and y

direction along its boundary. Further, a Multi-point constraint (MPC) is applied to the pad and specimen to keep the two bodies from rotating due to the loads applied as depicted in Fig. 4.3. The top nodes of the pad are forced to move in unison in the y-direction. In addition, MPC is imposed between the border elements where element sizes change in the same part of the setup. This is necessary in order to prevent free nodes of the smaller elements to penetrate their bigger counterparts. The fretting pad, its holder, and the specimen all have the same depth of 6.35 mm. The pad and specimen have both the same material properties of IN-100, while pad holder's are different. The pad holder is intentionally assigned low material properties so that it has only minimum effect on the interaction between the pad and specimen. Thus, the Modulus of Elasticity and Poisson's Ratio attributed to the holder are 5 Pa and 0.3 respectively. The contact load is applied on the upper side of the pad, the tangential load is applied on its the left hand side, and the axial stress is applied onto the right hand side of the half space of specimen. A small sliding contact condition is imposed between the specimen and pad.

As far as meshing is concerned, the four-node plane strain elements are chosen, as mentioned earlier on in this chapter, instead of the eight-node elements, in order to avoid oscillation in the stress state along the contact surfaces. The mesh of the pad and the specimen is gradually more refined towards the center of contact surface by changing certain geometric coordinates in the ABAQUS input file. Since the focus of the analysis is the stress, strain, and displacement distribution profile, such refinement is necessary in order to encompass any minute change in those values that could turn out to be crucial to understanding the fretting fatigue process in IN-100. Far away from the center, coarse mesh is used to save in computing time and system resources. The coefficient of friction is set at 0.45, slightly greater than the ratio of Q/P in order to have a converging numerical solution.

The generated meshes with their respective loading conditions, are run on the ABAQUS program in the UNIX environment. For each numerical simulation, The application of the constant contact load is applied as Step 1. Then, the maximum

bulk stress point and corresponding Q value on one hand and the minimum bulk stress point and corresponding Q value on the other hand are run separately in FEA as step 2. It should be mentioned that Q_{max} and Q_{min} used in FEA input files are determined after analyzing the experimental data for each specific test. Hence for every experimental test, two different input files are generated to run the simulation.

4.5 Load Inputs

As a first step during all FEA analysis, the contact load is applied and kept constant, 4003 N, throughout the process to avoid gross slip condition. The second step involves either the application maximum axial load condition or the minimum axial load setting. For the first case, the model simulates the application of the load cycle maximum with the shear force at its maximum in the same direction, as shown in Fig. 4.4. In the second scenario, the model simulates the application of the minimum axial stress condition, 3% of the maximum load, with the shear force at reaching its maximum in the opposite direction, as shown in Fig. 4.5. The frequency of the axial load is held at 10 Hz.

4.6 FEA Model Validation

Although the half-space assumption is violated in this study, and the "Ruiz" program is developed on the basis of that same assumption under static applied contact and axial loads, it remains a useful tool for quick check of FEA model by comparing their respective outputs. Figure 4.6 demonstrates that the $\sigma_{xx}, \sigma_{yy} and \sigma_{xy}$ stress curves from FEA analysis match well with the those from the Ruiz program for test #2. But for the purpose of this validation, FEA outputs of tests #2 (50.8 mm pad) and #7 (304.8 mm pad) are compared to the results predicted by the analytical solution calculated from Ruiz Program under the same load conditions, for the same tests. The check is conducted by comparing the contact half-width, the stress profile, Hertzian peak pressure, and nominal stress from both solutions.

4.6.1 Peak Pressure and Contact Half-Width. The first check is to compare the Peak Hertzian Pressures and the contact semi-widths computed via FEA with the theoretical values outputted from Ruiz. These values proved to be match well from both solutions, as shown in Fig. 4.7 for test #5 (50.8 mm pad). Hertzian peak pressure (P0) from FEA was determined as 680.217 MPa at x/$a_{Ruiz,max}$=.512 for 50.8 mm pads. When compared with the Ruiz results, the difference was 2.1% in magnitude and 0.778% in location along x-direction. As for the 304.8 mm pads, hertzian peak pressure (P0) from FEA was determined as 278.577 MPa at x/$a_{Ruiz,max}$=1.290 for 50.8 mm pads. When compared with the Ruiz results, the difference was 1.154% in magnitude and 0.178% in location along x-direction.

4.6.2 Stress Profiles. Figures 4.8 and 4.9 show the variation of the normal stress in the x-direction along the contact surface from the Ruiz Solution for test #2 (50.8 mm pad) and test #7 (304.9 mm pad) respectively, compared to the computational values of the specimen for this research. Good agreement is clear between the theoretical solution and the results of the FEA calculated results. For instance, in test #2 case, the predicted maximum normal stress in the x-direction varied by 5.7 %, $\sigma_{xx,FEA}$= 785.41 MPa versus $\sigma_{xx,Ruiz}$= 740.45 MPa. The location of the maximum stress is near the trailing edge (x/a=.96), with a difference of about 0.24%.

Figures 4.10 and 4.11 also depict the distribution of the shear stress in the x-direction along the contact surface from the Ruiz solution, and the computational values of the specimen for this research. Good agreement is readily observed between the theoretical solution and the results of the FEA calculated results. For test #2 case, the predicted maximum shear stress in the x-direction varied by 8.8%, $\sigma_{xy,FEA}$= -261.1 MPa versus $\sigma_{yy,Ruiz}$= -237.98 MPa. The location of the maximum shear stress is at a location of x/a=0.48 with a difference of 14.6%.

Lastly, Fig. 4.12 and 4.13 show the variation of the normal stress in the x-direction along the contact surface the Ruiz solution, and the computational values of the specimen for this research. The two solutions present good agreement. The

predicted maximum normal stress in the x-direction, for test #2, varied by approximately 0.6 %, $\sigma_{xy,FEA}$= -298.6 MPa versus $\tau_{xy,Ruiz}$= -296.79 MPa. The location of the maximum normal stress is at the center of the area of contact (x/a=0) with a difference of about 1.78%.

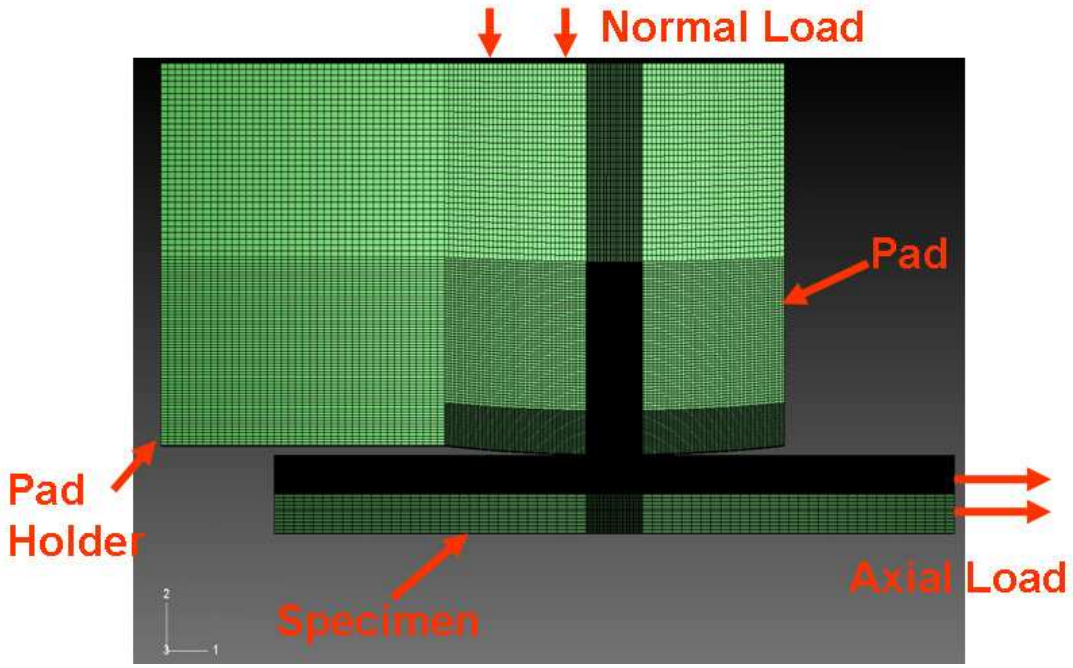

Figure 4.1: Finite Element Analysis Model for the 50.8 mm pad configuration

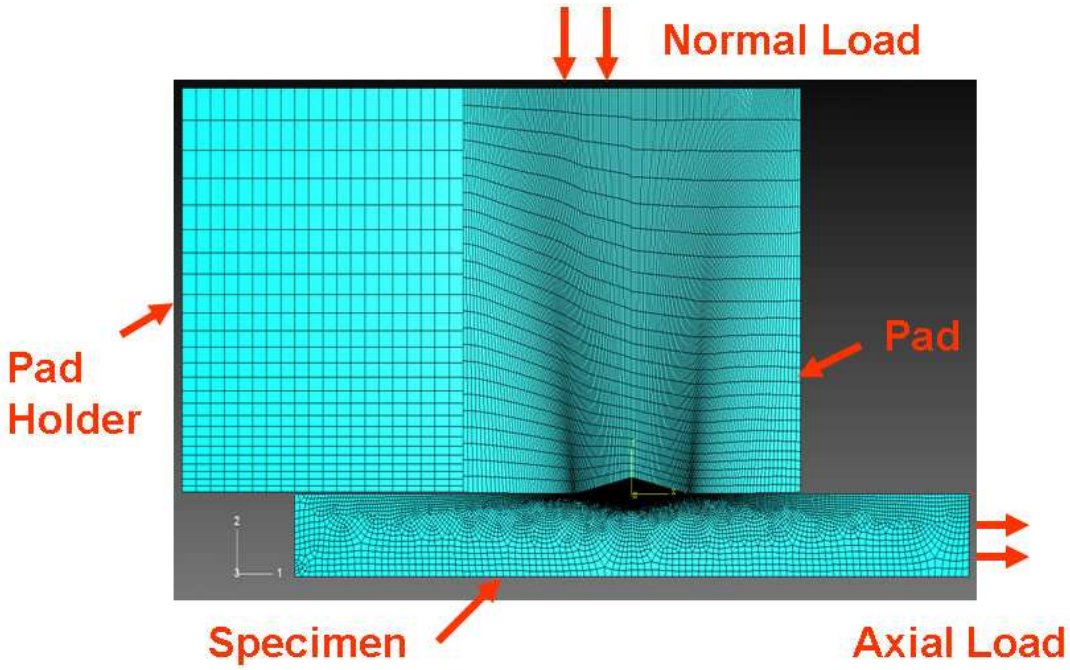

Figure 4.2: Finite Element Analysis Model for the 304.8 mm pad configuration

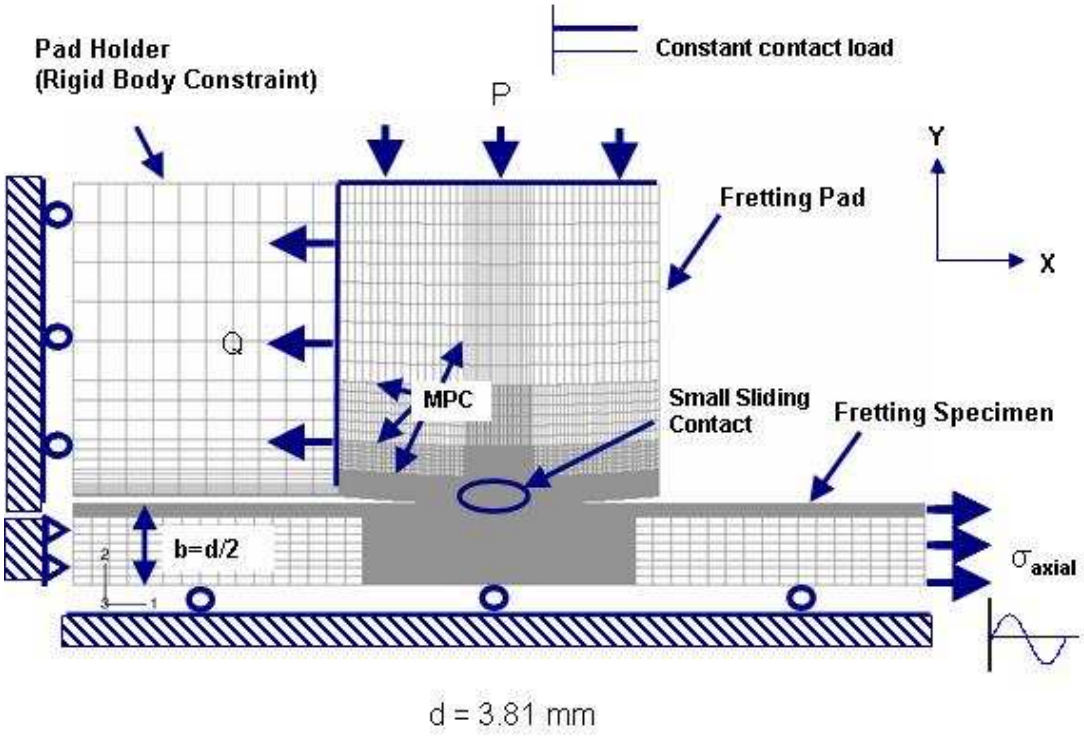

Figure 4.3: MPC Constraints in the Finite Element Analysis Model

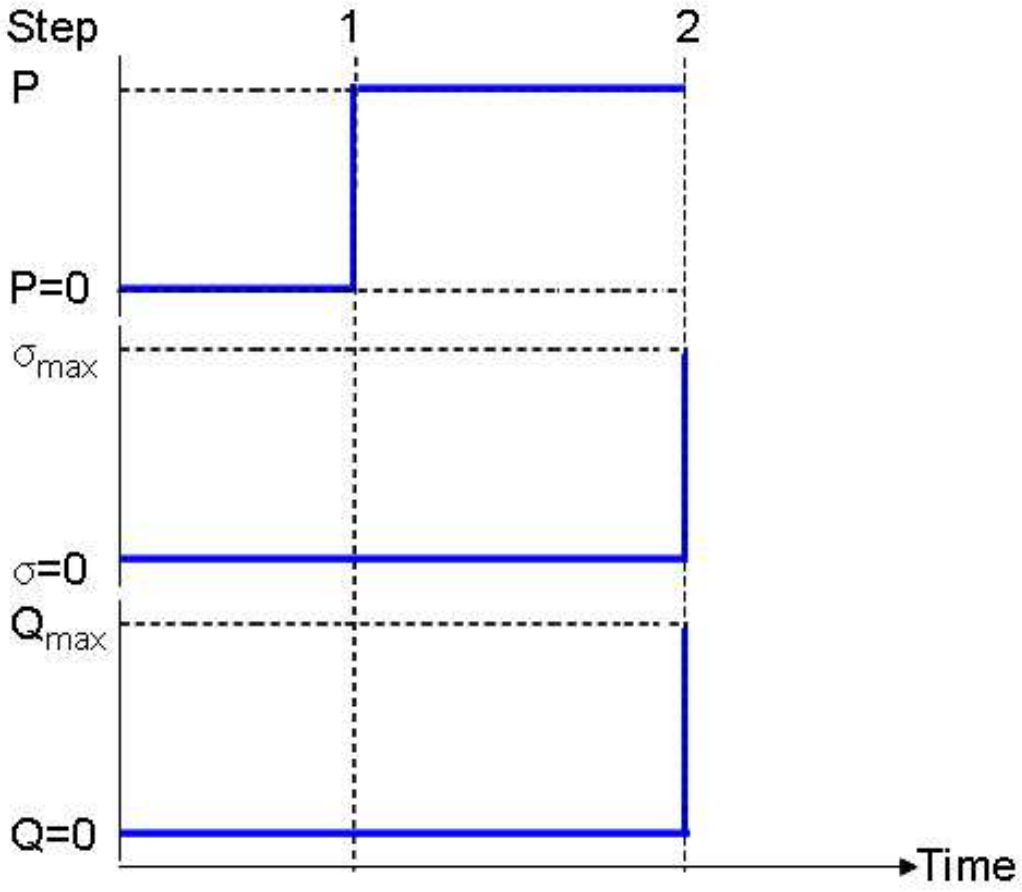

Figure 4.4: Load Configuration For Maximum Axial Load Condition

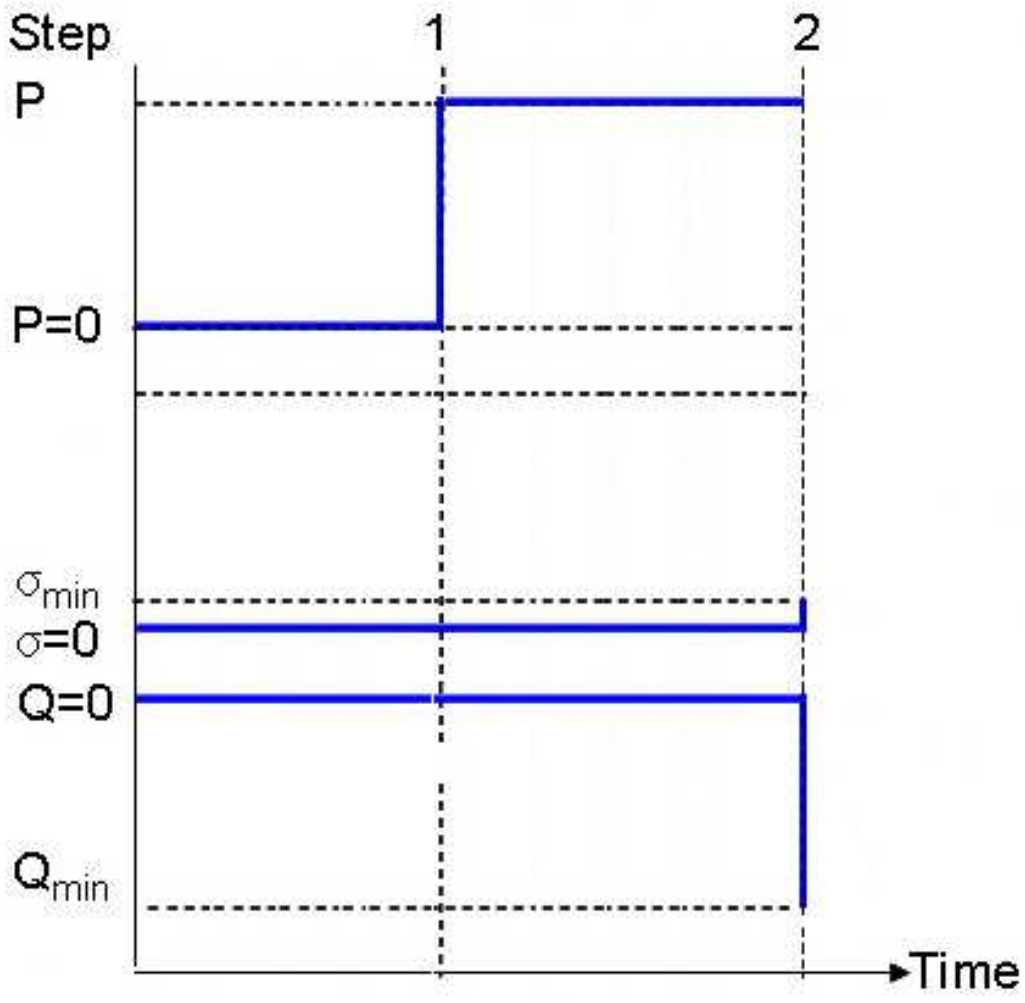

Figure 4.5: Load Configuration For Minimum Axial Load Condition

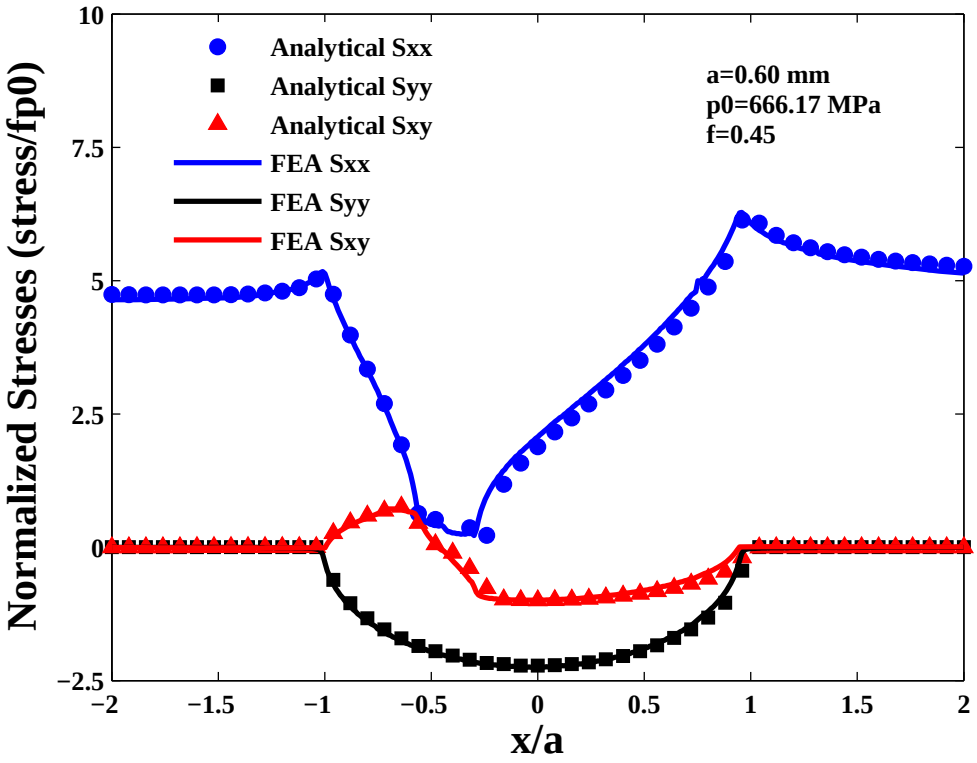

Figure 4.6: Stress Profiles Calculated from FEA and Ruiz Program along Contact Surface at step 2, Test #2

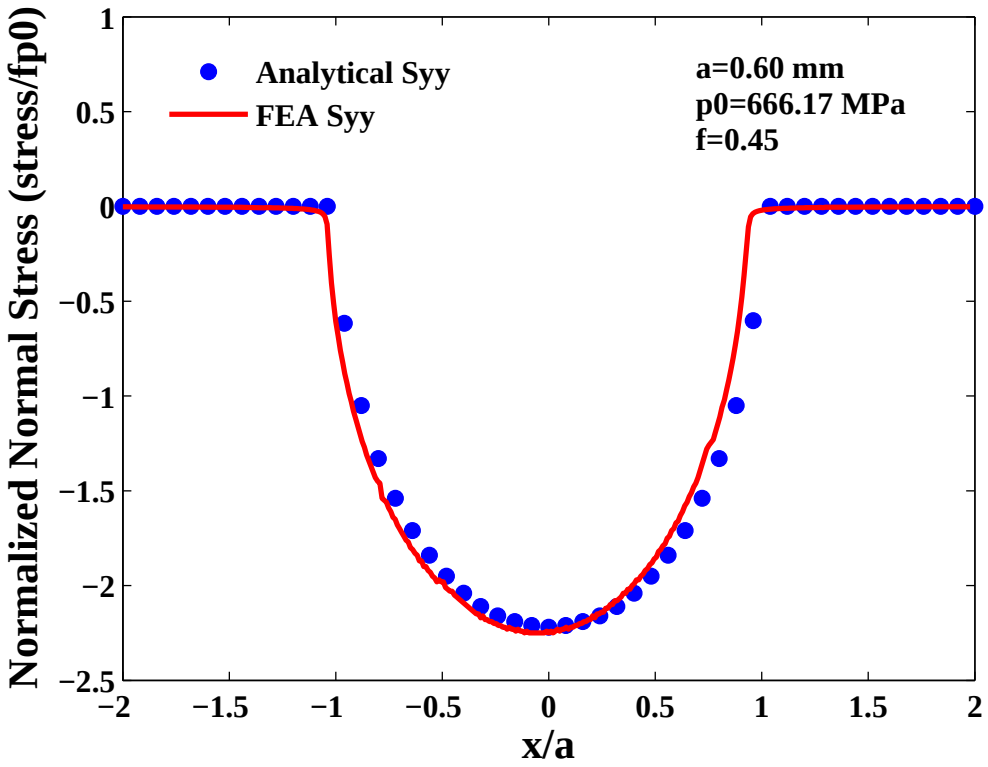

Figure 4.7: Stress Profile Calculated from FEA and Ruiz Program along Contact Surface at step 2, Test #5 for Hertzian Peak Pressure

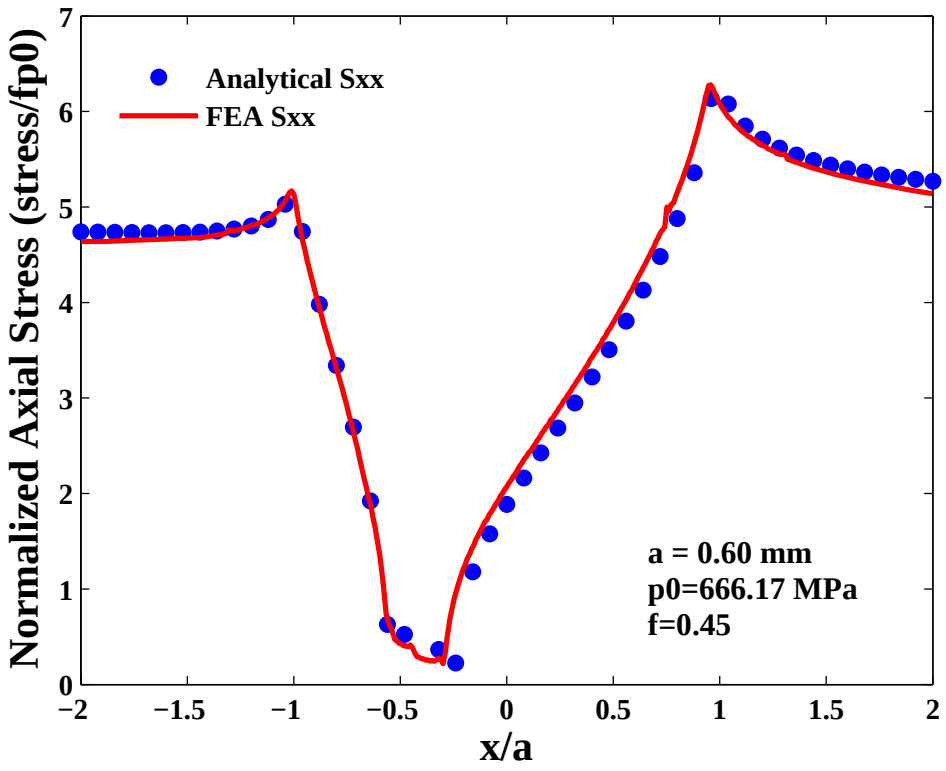

Figure 4.8: Analytical and Numerical Results of σ_{xx} Distribution Curves along the contact area of the 50.8 mm pad radius at the Maximum Loading Case for test #2

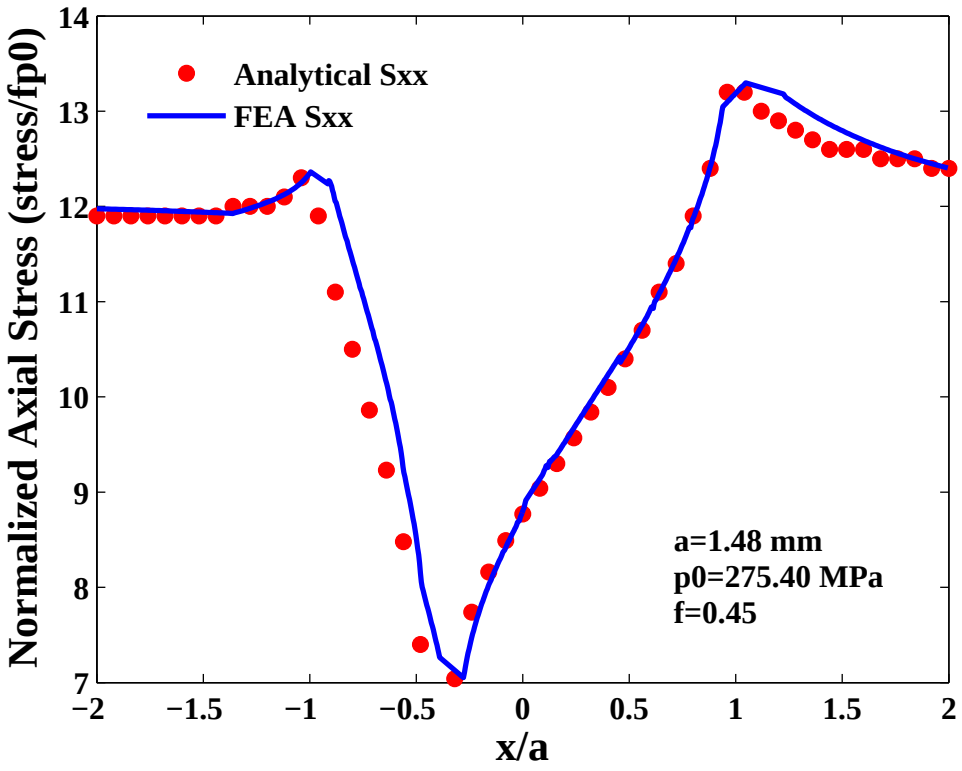

Figure 4.9: Analytical and Numerical Results of σ_{xx} Distribution Curves along the contact area of the 304.8 mm pad radius at the Maximum Loading Case for test #7

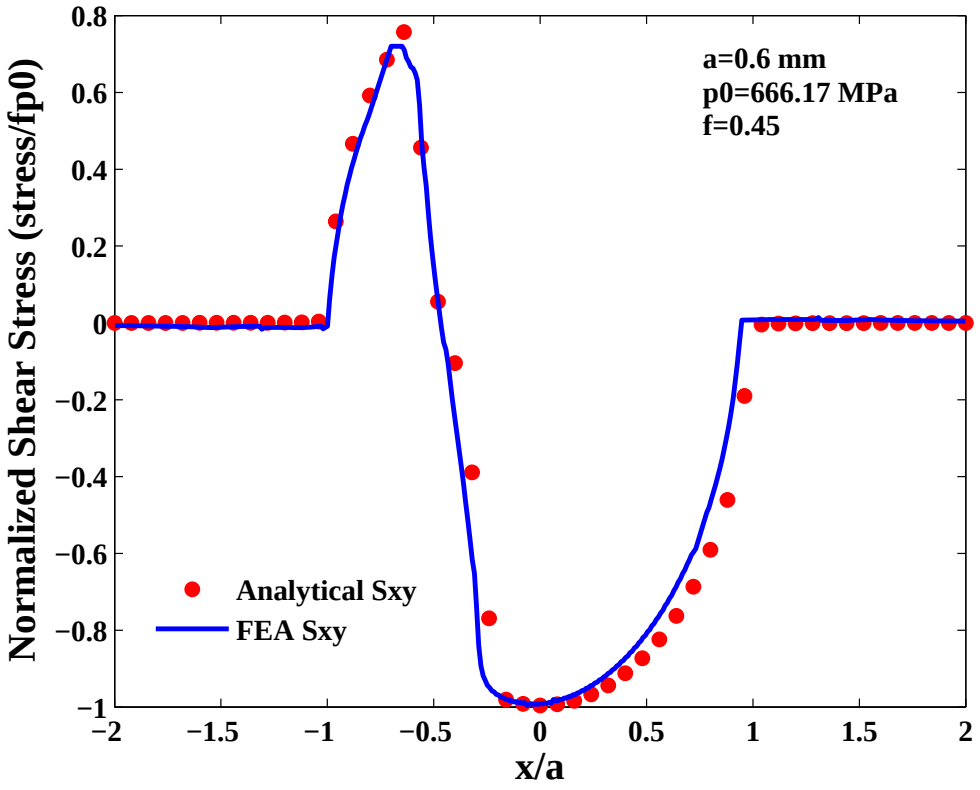

Figure 4.10: Analytical and Numerical Results of τ_{xy} Distribution Curves along the contact area of the 50.8 mm pad radius at the Maximum Loading Case for test #2

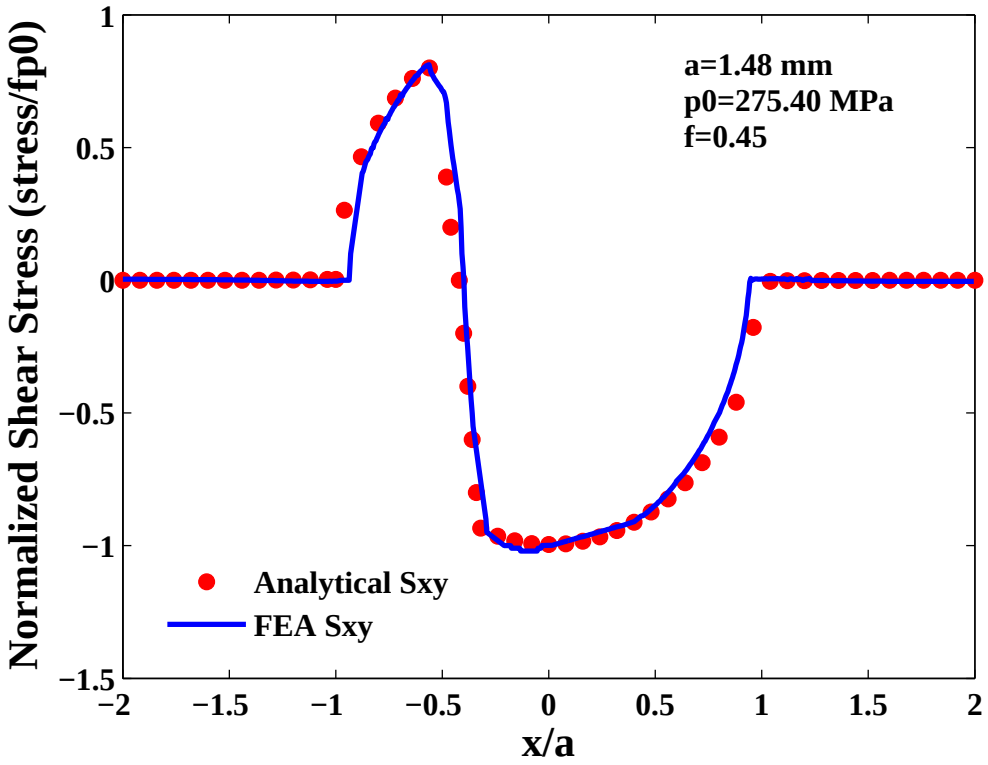

Figure 4.11: Analytical and Numerical Results of τ_{xy} Distribution Curves along the contact area of the 304.8 mm pad radius at the Maximum Loading Case for test #7

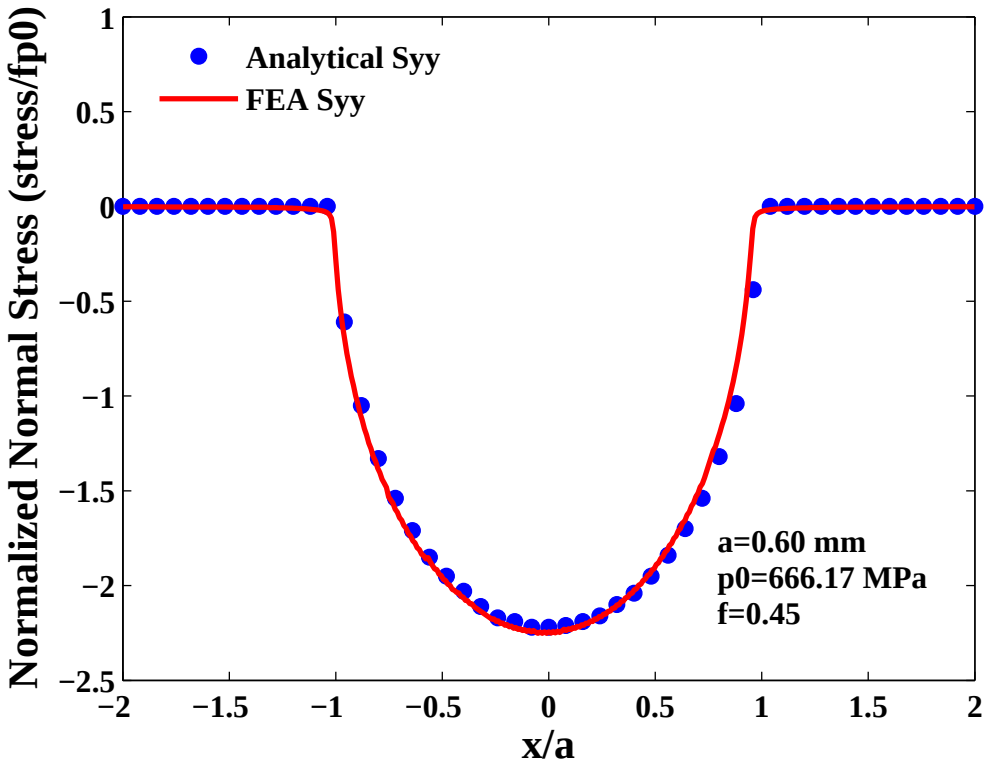

Figure 4.12: Analytical and Numerical Results of σ_{yy} Distribution Curves along the contact area of the 50.8 mm pad radius at the Maximum Loading Case for test #2

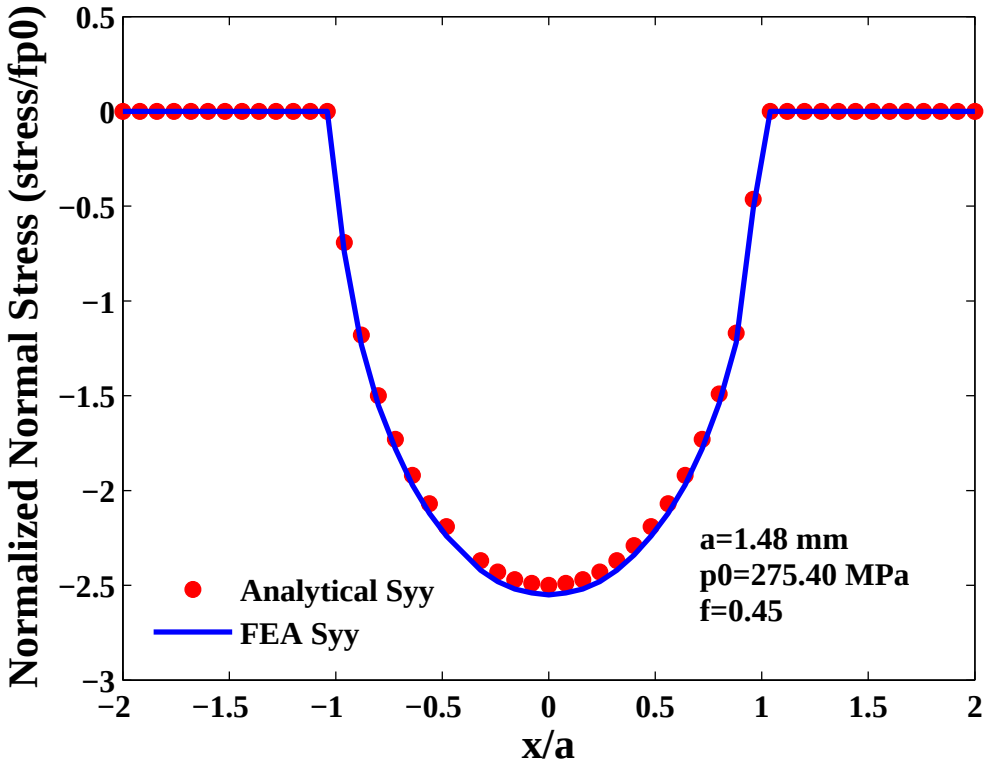

Figure 4.13: Analytical and Numerical Results of σ_{yy} Distribution Curves along the contact area of the 304.8 mm pad radius at the Maximum Loading Case for test #7

V. Results and Discussion

This first part of this chapter is devoted to present the experimental results. Also, the effect of fretting on fatigue life of IN-100 is discussed as well as that of changing the pad radius. To make any work complete, it is mandatory to supplement the experimental results with the computational analysis to attain a better understanding of the fretting fatigue behavior of nickel-based superalloys. So the second part of this chapter presents the finite element outputs. Following this, fretting fatigue predictive parameters are evaluated based on their ability to predict fatigue life without dependence on pad radii, crack initiation and crack initiation orientation angle.

5.1 Experimental Output

The applied stress range is the simplest fretting fatigue parameter to represent fatigue life data. There has been numerous studies showing the effect of this parameter on the fretting fatigue strength. Thirteen experimental tests were performed under the scope of this work. Their corresponding results are summarized in Table 5.1. The first five data points are obtained using the 50.8 mm radius pads whilst the next four tests were with the 304.8 mm radius pads. The last four experiments are conducted under plain fatigue conditions, i.e. the absence of any normal forces. The value of the shear force for each case is calculated using experimental data as described in Section 2.1.

5.1.1 Fretting Fatigue Condition Check. As discussed in Section 3.4, the process of fretting fatigue is known to develop a certain trend in hysteresis loops. This preliminary check has been undertaken for all fretting fatigue tests performed in this study. As an example, Fig. 5.1 shows clearly that the partial slip condition is met well before reaching the first thousand cycles. Further, tangential loads stabilized quickly and remained that way until the end of the test as depicted in Fig. 5.2. Therefore, the required partial slip condition was met for fretting fatigue tests, and this was the case for every experiment under this work. Hence, fretting variables such as contact

load, shear traction, axial load and coefficient of friction are expected to remain in a stable condition until failure occurs.

5.1.2 Shear Traction characteristics. Tangential load is plotted as time progresses for all tests. Figure 5.3 shows its sinusoidal pattern in phase with the axial load and at the same frequency. The two forces have the same trend and features, but vary in magnitude as expected. This plot is used to pick discrete load conditions for the two extremum steps used in the FEA modelling. As mentioned in Section 4.3, the maximum and minimum points of the axial loading which coincide with their corresponding extremum for the tangential load are used in FEA analysis.

5.1.3 Contact Details. One of the major drawbacks in studying the behavior of nickel-base superalloys is that they are magnetic materials. When taking pictures of the cross-sectional area where the failure occurred under the SEM, the scanning electron microscopy, the electron beams emitted by the microscope on the specimen deflect as a result of the magnetic field, and make the SEM miss important details resulting in a blurry image. This makes it almost impossible to take any higher magnification pictures with the SEM, usually lower than 500x magnification. Several attempts are made to improve the quality of the photographs shown by the SEM, such as reducing the voltage to its absolute minimum to make the electron beams as thin as possible and reduce the magnetic effect. Coatings the cross-section area of the specimen has also been tried. Nevertheless, the author of this study was not able to obtain ultra high magnifications of the concerned region, so as to characterize the micro-structure of the initiation zone to better understand the fretting mechanism at the grain level and make correlations with other superalloys. All in all, some of the features of fretting fatigue are still depicted in figures taken for specimens and pads contact area.

A typical specimen scar pattern is shown in Fig. 5.4 and 5.5 for the 50.8mm pads and the 304.8mm pads respectively. Similar to the contact model shown in Fig. 2.2, the fretting fatigue scars shown identify clearly a "stick zone" in the center

area with darker thin lines on the edges denoting "partial slip" zones at the leading and the trailing edges of the contact area. The width of the resulting scar pattern for each test run is measured and determined to be twice a_{exp}, which comes within 16% maximum of the theoretical values determined by the Ruiz program. So the contact width, 2a, for experiments with pad radius of 50.8 mm was 1.016 mm against 2.576 mm for the 304.8 mm radius pad-experiments. The corresponding analytical values were 1.204 mm and 2.951 mm respectively. These measurements confirm that, as predicted by Equation 2.9, contact half-width is only affected by the magnitude of the constant contact load and pad radius but is independent of the bulk stress conditions.

5.1.4 Crack Initiation Details. A crucial feature of fretting fatigue behavior is the prediction of crack initiation location. For all experiments under this study, crack initiation location occurred at the trailing edge, at a location of x/a=+1.0 along the x-direction, as shown in Fig. 5.6. Zones of crack initiation are identified as the discolored and darker region on the failed specimen surface as also illustrated in Fig. 5.7. As was mentioned earlier, the trailing edge location corresponds to the point where maximum axial load is applied. Similar observation was made in Ti-6Al-4V which is well explained in the literature. In effect, Magaziner argued in his study [20], that crack nucleates in this particular area due to the fatal stress concentration forming at the border of the stick zone which could be the cause of the shifting of the stick zone. It was previously observed from the FEA output, that the stick zone shifted between the two combined loading cases, as the fretting pad rolls while Q and normal load change magnitude. When the specimen and pad are "welded" together, it is conceivable that the stick zone shifts which results in material ripping from the substrate surface that was stuck to the pad. Potential cracks can then initiate at the sharp tears produced in the ripped surface, and propagate due to the applied axial load. This explanation makes logical sense since, in the absence

of fretting, no stick zone forms preventing any dangerous crack from initiating in the first place.

At higher magnification, the distinction between the "stick zone" and "partial slip zone" is still noticeable but is fading away as the magnification reaches a certain value due to the magnetic material effect, as shown in Fig. 5.7 and 5.8. The river-like patterns noted in several studies on Ti-6Al-4V [43], [3], are depicted in the figure right at the boundary of the stick zone. It can be readily seen that the stick zone with all the microstructure details is blurry and shows no further details as regards the slip between the grain boundaries or the striations that the author was hoping to depict.

5.1.5 Crack Initiation Location and Orientation. Another important issue in this study is to determine the crack orientation along the contact surface. The main purpose for that is to compare the predicted angle of crack orientation and the experimentally measured value, which can be used to validate the accuracy of fretting fatigue parameters. In most previous studies not including nickel-base superalloys, failure takes place due to growth of a primary crack that nucleates at the trailing edge of the contact surface. There are almost always other secondary and smaller cracks that never grow big enough to cause failure. In Ti-6Al-4V, the initiation orientation angle is known to be 45 $\pm 15^o$. In this study, the author is interested in determining crack orientation angle for IN-100 specimens and compare their values to their counterparts in Ti-6Al-4V. To determine crack initiation orientation, failed specimens are sectioned in the direction of the applied normal load. The cut substrate is then mounted in a transparent medium, ground and polished. To ensure that the sectioned surface is at the center of the crack initiation zone, the SEM is used after polishing small increments of the specimen.

In general, there are two types of cracks that are found in a fretting fatigue specimen, primary and secondary ones, as discussed in Section 2.3. The first type is the crack that leads to failure, whilst the other type does not, but is also detectable

by the SEM along the contact surface. The photograph from the scanning electron microscopy presented in Fig. 5.9 shows that primary crack initiation orientation is at 43^o for test #4. There were no other secondary cracks for this specimen. In this work, only two specimens are sectioned and looked at, since the results are in agreement with the predicted values by the fatigue parameter as discussed later.

5.2 Fretting Fatigue Life

Figure 5.10 is the S-N curve obtained which plots the number of cycles until failure for all the tests conducted in this work. The figure also shows the best fit to the three plots, fretting fatigue data with 50.8 mm radius pads, 304.8 mm radius pads as well as plain fatigue data. This logarithmic plot shows the same characteristics of fretting fatigue life as those known in other alloys. As the bulk stress decreases, the slope of the specimen's fatigue life becomes flatter in the direction of the endurance limit, which is not reached in this study. By definition, the endurance limit is the stress level at which a part manufactured from the material will not fail in fretting fatigue.

5.2.1 Fretting Fatigue Versus Plain Fatigue Data. In this subsection, the fretting fatigue and plain fatigue experimental data are compared. The data is compared based on the applied load conditions by using, $\sigma_{effective}$, the effective stress, calculated as follows:

$$\sigma_{effective} = \sigma_{max}(1 - R)^m \tag{5.1}$$

where R is the stress ratio and m is a constant found to be 0.45 by Lykins [19]. The two sets of data are compared without taking into account the stress concentration that occurs at the trailing edge of the contact zone. Several authors, among whom Adibnazari [2], Harris [11], and Waterhouse [42], have used this method by considering only the contribution of stress from the axial load.

A number of authors have used plain fatigue data as a baseline, from which to assess fretting fatigue behavior. The reduction in fretting fatigue strength as

compared to plain fatigue is a result of the effect of contact stress concentration, and the effect of corrosion, as reported by Nishioka [26]. The fretting fatigue endurance is also known to be greatly affected by the introduction of fretting as reported by Migala [21]. Moreover, it has been suggested that titanium alloys incur a reduction in fatigue strength due to the removal of the protective surface axide layer, as shown by Antoniou [5].

Figure 5.10, represents the plain fatigue best fit curve relative to fretting fatigue data, in terms of the number of cycles until failure for all the test runs in this work, as recorded in Table 5.1. Note that for a given value of the effective stress, the fretting fatigue data exhibits a much shorter life than its plain fatigue counterpart. For instance, at $\sigma_{effective} = 922$ MPa, the fretting fatigue life is about 78,000 cycles (50.8 mm pad configuration) and the plain fatigue is more than 200,000 cycles. The S-N curve, as displayed in Fig. 5.10 illustrates a significant decrease in the failure cycle numbers due to the presence of fretting, i.e. the introduction of a normal load. Namjoshi et al. [25] demonstrated the same trend for Ti-6Al-4V. In most other superalloys, the magnitude of the reduction in the endurance limit due to the introduction of fretting varies in laboratory tests but a reduction of 30 % of the plain fatigue life is not uncommon. So in essence, IN-100 behavior under fretting fatigue does confirm the general premise of degradation as compared to plain fatigue. It is readily seen that this difference is of major importance.

5.3 Pad Geometry Effect on Fretting Fatigue Behavior

Since two different pad radii, 50.8 mm and 304.8 mm, were used in this work, the present study investigated the repercussions from different pad radii on the global fretting fatigue behavior of IN-100.

5.3.1 Pad Geometry Effect on Fatigue Life. Figure 5.10 illustrates the effect of different pad radii on the fretting fatigue life of IN-100. It was interesting to note that changing the radius of the cylindrical pads from a high curvature value (50.8

mm) to merely flat pads (304.8 mm) did not have equal effect on the fatigue life. The two pad configurations life fatigue curves are certainly distinguishable, as can be seen from the two corresponding curve fits, yet they are not too far apart as is the case in titanium alloy, Ti-6Al-4V as shown in Fig. 5.11 [24]. In fact, for the same maximum axial stress level of 800 MPa, changing the pad radius from 50.8 mm to 304.8 mm (500% increase) the fretting fatigue life only decreased from 245,000 cycles to 189,000 cycles ($\sim$ 23%). Figure 5.12 shows the S-N curves for both Ti-6Al-4V and IN-100 alloys, which illustrate clearly that IN-100 is a stronger alloy than Ti-6Al-4V.

5.3.2 Pad Geometry Effect on Stress Profiles. Figure 5.13 illustrates the effect of changing the pad radius on the axial stress distribution for the same maximum axial stress level of 650 MPa, a longitudinal load of 12.80 MPa and a constant normal load of 4003 N. Both curves show approximately the same overall trends. However, it is interesting to note that the 50.8 mm pad configuration presents a minimum compressive stress near the center of the area of contact at x/a=0.08, while minimum stress for 304.8 pad configuration is tensile at x/a=-0.5. The 304.8 mm curve is almost symmetric with respect to the y-axis, since it is practically a flat pad. Also the maximum stress is approximately 1.3 times larger for tests with the 50.8 mm pad than with the 304.8 mm pad, both occurring near the trailing edge.

Figure 5.14 depicts the effect of changing the pad radius on the shear stress distribution for the same cited load conditions cited earlier. For the the 50.8 mm pad configuration, the maximum value in magnitude occurs interestingly very close to the center of contact, while its corresponding location for 304.8 mm pad tests is at x/a=-0.4. Further, the effect of flatter pad is apparent at x/a near the two ridges, since the shear stress distribution is parabolic in that area. Moreover, the minimum stress is approximately 2.5 times larger for tests with the 50.8 mm pad than with the 304.8 mm pad.

Figure 5.15 illustrates the effect of changing the pad radius on the normal stress distribution for the same load conditions cited earlier. Both curves show exactly the

same overall symmetrical distribution, although the 304.8 mm curve is flatter around the origin. However, the maximum stress, Hertzian peak pressure, is approximately 2.3 times larger for tests with the 50.8 mm pad than with the 304.8 mm pad. On the other hand, changing the pad radius did not alter the location of the Hertzian peak pressure, which is at the center of the contact zone for both pad configurations.

5.4 FEA Results

As discussed in Section 5.1, the load values shown in Table 5.1, are used in the FEA model in order to determine the stress, strain, and displacement distribution within the area of interest on the contact surface. Throughout this section, nickel-based superalloy is compared to titanium as a reference due to the numerous studies done on the latter in fretting fatigue regime.

5.4.1 Contact Stress State. Table 5.2 summarizes the different stresses input values used in the two FEA models, one for each pad radius. The distribution of stresses $\sigma_{xx}, \sigma_{yy}, \sigma_{xy}$ is presented in Fig. 4.8, 4.12 and 4.10 for test #4. These figures look very similar to the stress distribution for titanium under fretting fatigue, as shown in Fig. B.1, B.2 and B.3 found in Appendix B. For the σ_{xx} curve, the maximum value is reached at the trailing edge at a location of $\frac{x}{a}$ between 0.93 and 0.96 for the 50.8 mm pads and between 0.91 and 0.96 for 304.8 mm pads. These points are located inside the stick zone. This location is known as the trailing edge. Looking up in the positive x-direction from the center of the contact area, the curve almost linearly slopes up to a tensile stress peak, which is almost at the edge of the contact zone. From that point on, σ_{xx} continues to decrease until it eventually goes back to the remotely applied bulk stress at the actuator end. In the negative x- direction, σ_{xx} slopes up less rapidly to a lower peak and then gradually decreases until it eventually reaches the remotely applied bulk stress as well. At the center of the contact area, it is interesting to note that concentrations of compressive σ_{xx} are found in test runs with 50.8 mm pads, also observed in titanium [20]. The maximum always occurs at

the center of contact, with a slight difference of about 2.95% to 7.17%. With the 304.8 mm pads, the minimum stress value is tensile but also took place at a location near the center of the contact with a difference between 1.7% and 3.44%.

Concerning σ_{yy}, it shows the symmetrical distribution typical of any cylinder on flat contact. As shown in Fig. 4.7, the local normal stress reaches a maximum compressive value at the very center of contact as expected. With symmetry towards both edges of the contact area, the stress increases parabolically to reach zero approximately at the edge of the contact zone. This only seems logical since just the part of the substrate that comes into contact with the pad is capable of generating pressure. In reality, the computational model is not exactly at zero at the edges of contact but will asymptotically reach it. Therefore, the σ_{yy} distribution curve is used to determine the FEA predictive value for contact width. The contact widths are collected from each test and compared with the theoretical values. The results show very close correspondence with a difference of 1% at most for the 50.8 mm pads and 5.3% for the 304.8 mm pads. For peak pressure, the FEA model predicted values with an accuracy of 3.7% difference from the analytical model for both radii. Hence, good agreement is established between the analytical and computational analyzes with regard to the contact width.

Between the two radii considered in this study, the σ_{yy} distribution differed in contact width and peak pressures at the same stress condition. The first difference concerning the width makes logical sense since the flatter the pads are, the more contact is in effect. Further, the tips of each curve bell are at different magnitudes. As can be concluded from the analytical formula, the peak contact pressure decreases as the radius increases. Hence the σ_{yy} distribution is also in conformity with the expected trends.

As for τ_{xy} distribution along the contact surface, it is commonly agreed that the local normal stress and shear stress are linked. The extremum noted in σ_{xx} are known to be an effect of the presence of shear stress. For all tests, shear stress

distribution keeps the same trends. The maximum values are persistently reached in the positive x-direction somewhere between the center of contact and the trailing edge. It is significant to note that all the specimens run under this work failed at a location between the position of maximum shear stress and maximum axial stress. In this particular portion of the contact, shear stress is decreasing parabolically until it reaches zero values outside the contact area. There is another extremum reached by τ_{xy} in the negative x-direction, but of less magnitude than the first one.

5.5 Fatigue Parameters

In this section, the fretting fatigue parameters discussed in Section 2.2 will be evaluated based on their ability to predict the number of cycles to failure without dependence on pad geometry, the crack location and the crack initiation orientation along the contact surface. Those parameters are: the shear stress range parameter, the Findley parameter, the Smith-Watson-Topper parameter and the modified shear shear stress parameter. For this purpose, finite element analysis (FEA) is conducted to simulate the experimental conditions. Using FEA output in terms of stress, strain and displacement at each node along the contact zone, a FORTRAN program calculates each parameter at those locations and returns the maximum value for each of the parameters and its respective location. These results will be compared to the experimental results presented in Section 5.1. The appropriate parameter for IN-100 will be discussed in light of this comparison results.

5.5.1 SSR Parameter. It is a well accepted fact that for ductile materials, crack initiation begins with the creation of slip bands resulting from intense deformation due to shear motion between crystal planes [8]. Lundberg [18] demonstrated that the shear stress amplitude on the critical plane can be used to predict bearing ring failures under contact conditions. Since the roller bearing configuration is similar in the most part to the fretting fatigue configuration, shear stress amplitude on the critical plane maybe an appropriate parameter to predict the fretting fatigue param-

eters. SSR parameter is evaluated using the computed values of local stresses from the finite element analyzes to determine the maximum and minimum shear stresses at all planes ranging from $-\pi/2 \leq \theta \leq \pi/2$ in increments of 0.1^o using the equations in Chapter II. The results are shown in Table 5.3.

Figure 5.16 shows the measured fretting fatigue life as a function of the SSR parameter, obtained for two cases; 50.8 mm and 304.8 mm pads. The first condition for the acceptance of a fretting fatigue parameter is its ability to predict the number of cycles until failure, without dependence on pad geometry. In this respect, SSR parameter shows the same trend as the S-N curve in Fig. 5.10 for both pad radii, decreasing as the fretting fatigue life increases. Yet, they are spread apart, with about 300 MPa difference on average for the same fatigue life. This difference is clearly much more pronounced than the difference shown in the S-N curve. Hence SSR has failed based on this consideration.

The second condition that must be met for a predictive fretting fatigue parameter acceptance is the ability to predict crack location. SSR predicted crack location, as seen in Table 5.3 correlates well with the observed crack location. In fact, the initiation location was determined to be near the trailing edge of contact, $0.89 < \mathrm{x/a} < 0.99$.

The third condition for the parameter's acceptance is the ability to predict the crack initiation orientation along the contact surface. It should be noted that there are two possible choices for crack orientation, due to the shear stress on the critical plane. The angles can be out out phase by either 90^0 or 180^o, as can be deduced from a simple inspection of the Mohr's circle. From Table 5.3, SSR can evidently predict well the crack initiation orientation, since the predicted angles are $\pm 45^o \pm 5^o$.

Overall, the SSR parameter did not meet all the conditions for fretting fatigue parameter acceptance. It could satisfactorily predict crack location and crack initiation orientation but it failed to predict fatigue life without dependence on pad geometry. This may be due to the fact that it does not account for normal stress

contribution, as noted by Namjoshi et al. [25] in Ti-6Al-4V. Hence, this study goes on to use the Findley parameter which includes the effect of normal stress to a certain degree.

5.5.2 Findley Parameter. Multiaxial loading effect are to be taken into consideration when studying fretting fatigue behavior, as it is one of the main causes of the fretting fatigue process. The Findley parameter takes into account both the shear and normal stresses, as described in Section 2.2.2. Figure 5.17 shows the Findley parameter distribution for both pads radii. The parameter shows two distinct curves approximately following the same trends as in the S-N curve in Fig. 5.10. Again referring to the conditions of fretting fatigue parameter acceptance, the first condition is the ability to predict the number of cycles to failure. Through the figure, it is clear that the Findley parameter has brought the two pad parameter curves closer together, by making the contribution of the shear stress more important than the normal stress, k=0.35 in Equation 2.15. However, Findley parameter still relies on pad radii and does not completely collapse the data onto one curve that allows the prediction of the fatigue life.

The second condition that must be met for fretting fatigue parameter acceptance is the ability to predict crack location. The predicted crack location resulting from this fretting fatigue parameter is in good agreement with the experimental results. The crack initiation location was determined to be near the trailing edge, within satisfactory accuracy, $0.88 < x/a < 1.0$ (See Table 5.4).

As for the third criterion that must be satisfied for fretting fatigue parameter acceptance, crack initiation angles prediction. This parameter predicts values of approximately -63.0^o for 50.8 mm pads and between -60.5 and -67.1^o for the 304.8 mm pads, which differs significantly from the experimental results ($\pm 45^o$). In general, the findley parameter failed to predict the crack orientation along the contact surface. Further, it has been previously observed in a study performed by Namjoshi et al. [25]

that this parameter could not discern between plain fatigue and fretting fatigue when determining fatigue life, which is evidently very important.

In summary, the Findley parameter cannot be considered a good predictive fretting fatigue parameter for IN-100. The parameter was not effective in collapsing the data onto a single curve to predict the number of cycles to failure without dependence on pad geometry. Moreover, the Findley parameter could not predict well the crack orientation along the contact surface. However, this parameter predicted the crack location to be near the trailing edge of contact, which correlates with the experimental observations.

5.5.3 SWT Parameter. The SWT parameter is evaluated in two slightly different ways. The first method is the product of the maximum principal stress and the principal strain amplitude, i.e. $\sigma_{max}\epsilon_a$, while the second method uses the maximum of the product of the two values, ie. $(\sigma * \epsilon_a)_{max}$. In the present study, the two methods are compared and the maximum SWT parameter is selected. The results are shown in Fig. 5.18, taken for two pad radii cases. More details are provided in Table 5.5.

With respect to the condition of fretting fatigue parameter acceptance, the first condition is the ability to predict the number of cycles to failure. As can be observed, the SWT parameter showed a similar trend as that of the S-N curve. It has brought the two pad configurations closer together, relatively better than the Findley parameter. However, it is still making clear distinction between the two pad radii, like the Findley parameter distribution.

The second criterion that must be satisfied for a good fretting fatigue predictive parameter is the ability to predict crack location. The predicted crack location resulting from SWT parameter was in good agreement with the experimental results except in one case, test #9. In the most of the cases, the SWT parameter predicted the crack location to be at the trailing edge of the contact area, $0.8 < \mathrm{x/a} < 0.95$.

The other condition that has to be met for fretting fatigue parameter acceptance is the ability to predict the crack orientation along the contact surface. As Table 5.5 shows, the angles predicted for crack initiation orientation were approximately $0^o \pm 1.2^o$. These results differ from the observed orientation angle of $\pm 45^o$. In all cases, SWT parameter failed to predict the crack initiation orientation angle along the contact surface, just like in Ti-6Al-4V [3].

In general, the SWT parameter failed to meet all of the required conditions for predictive parameter acceptance. Although the parameter succeeded into some extent in bringing the two pad configurations' curves closer together, it was not able to totally collapse them onto one single curve that predicts fatigue life without dependence on pad geometry. It was not also able to accurately predict crack initiation orientation angle, and failed in one case to predict the crack location.

5.5.4 MSSR Parameter. As discussed in Section 2.2.5, to overcome its shortcomings, the SSR parameter has been modified in the form similar to the Findley parameter to account for the normal stress which contributes in opening the crack surfaces. However, the constants A,B,C,D used to calculate this parameter as shown in Equation 2.23, were developed based on a curve fit to data obtained on Ti-6Al-4V [24]. So as a first step, this work used these same constants in order to determine if this parameter can collapse the fretting fatigue life data on one single curve, with no dependency on pad radius. Figure 5.19 shows the fretting fatigue life data as a function of the Modified Shear Stress Range parameter. More details about these results are found in Table 5.6.

The MSSR parameter, as used for Ti-6Al-4V [24], predicted well the crack initiation location, i.e. near the trailing edge (x/a between 0.98 and 0.96). In addition, the crack initiation angle was $\pm 3^o$ within + or -45^o angles, which matched well with the experimental results. On the overall distribution, MSSR shows the same approximate trend as that of the S-N curve in Fig. 5.10, decreasing as fretting fatigue life increased for both pad radii. It has brought the two curves much closer together,

but not enough to collapse the two pad configurations onto a single curve that can predict fatigue life without dependency on pad geometry. Since the first condition for fretting fatigue predictive parameter acceptance is to collapse the data into one curve to predict fatigue life without reliance on pad radii, the author attempted further to find new A,B,C and D constants that can do just that.

The second set of constants chosen were A=0.75, B=0.25, C=0.75 and D=0.5. It is clear from these values that less emphasis is put on shear stress distribution. Table 5.7 shows the corresponding results. Figure 5.20 is an illustration of MSSR parameter distribution for both pad configurations. The figure depicts the two pad configurations' curves collapsed to one single curve with a standard deviation of 1.53, and a mean error of 0.001%. Therefore, this version of MSSR can be considered to work well to predict fatigue life without dependency on pad geometry. However, the two curves have become too flat making the data had to employ in the design of components subjected to fretting fatigue.

A third version of the constants was A=0.5, B=0.25, C=0.75 and D=0.5. Table 5.8 shows the corresponding results. Figure 5.21 depicts MSSR parameter distribution for both pad configurations. The figure shows the two pad configurations' curves collapsed to one single curve with a standard deviation of 1.41, and a mean error of 0.0006%. As a result, this version of MSSR works even better than the previous one to predict fatigue life without dependency on pad geometry. However, the two curves are even flatter making the fretting fatigue life prediction hard to do. It is clear that making the constant B=0.25, which takes the power of the shear stress range to a quarter, makes the slope flatten out.

Therefore, this study adopted another approach in an attempt to collapse MSSR results onto a single curve without losing the slope effect shown in the S-N curve. This method involves changing the MSSR constants first similar to the Findley parameter approach, by reducing the normal stress factor (C) to even lower values than 0.35 used in the latter, as k factor. It was clear that the two curves were coming closer

even further than with the Findley parameter, while keeping the same slope seen in the S-N curve (See Appendix C). In addition, A and B constants were adjusted so as to bring the two pad configuration curves onto a single scatter band. Using A=0.05, B=0.5, C=0.05 and D=0.9, the MSSR results, from both pad radii and plain fatigue data, came within a scatter band for pad geometries as shown in Fig. 5.22, with a standard deviation of 3.54 and a mean error of 1.0%. Similar MSSR trends were observed in a study conducted by Namjoshi et al. [24] conducted on Ti-6Al-4V alloy using different pad geometries. Figure 5.23 illustrates those findings in the titanium superalloy with the MSSR constants: A=0.75, B=0.5, C=0.75 and D=0.5. The two MSSR distributions, presented in equivalent scales, show approximately the same scatter band of the data. The IN100 data has a relatively higher scatter due to the fact that it is a stronger material than its titanium counterpart. This is shown in Fig. 5.24 where MSSR parameter is plotted versus fatigue life for both materials.

The second condition that must be met for predictive parameter acceptance is the ability to predict crack initiation location. The crack location, as predicted by the MSSR parameter, was in good agreement with the experimental findings. The MSSR parameter predicted the crack location to be very close to the trailing edge of the contact area, $0.89 < x/a < 0.99$.

The third criteria for the parameter's acceptance is the amount of accuracy to predict the crack initiation orientation along the contact surface. From Table 5.8, MSSR can evidently predict well the crack initiation orientation, since the predicted angle is $\pm 45^o \pm 5^o$.

Overall, MSSR parameter was the only parameter to satisfy all the three criteria, to a certain extent in IN-100, for fretting fatigue predictive parameter acceptance. This only supports the fact that although shear stress plays a significant role in fretting fatigue, normal stress contribution cannot be neglected in the nickel ally also. Therefore, MSSR parameter may be used for estimating fretting fatigue life without dependence on pad geometry.

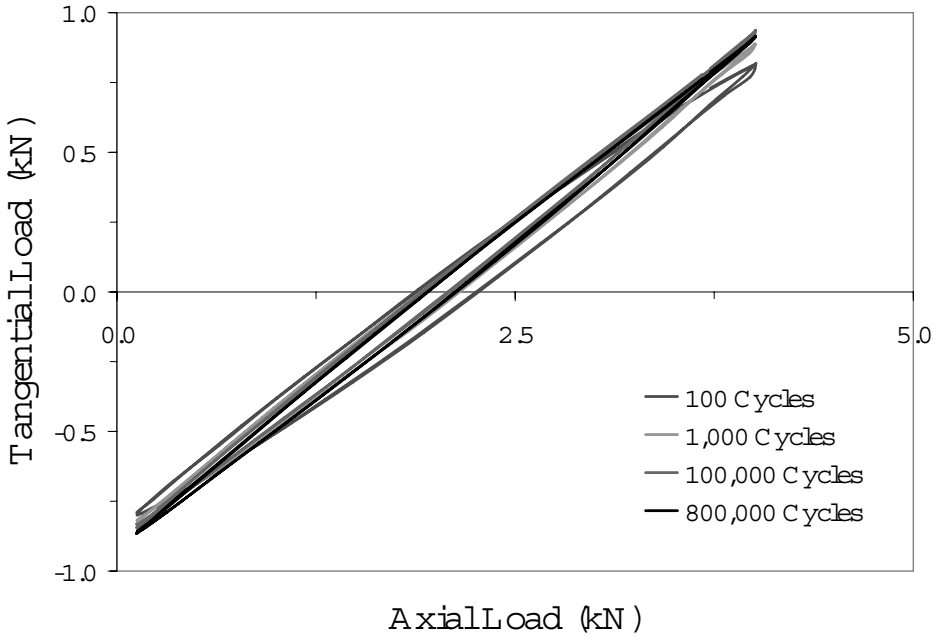

Figure 5.1: Hysteresis Loops for test #2

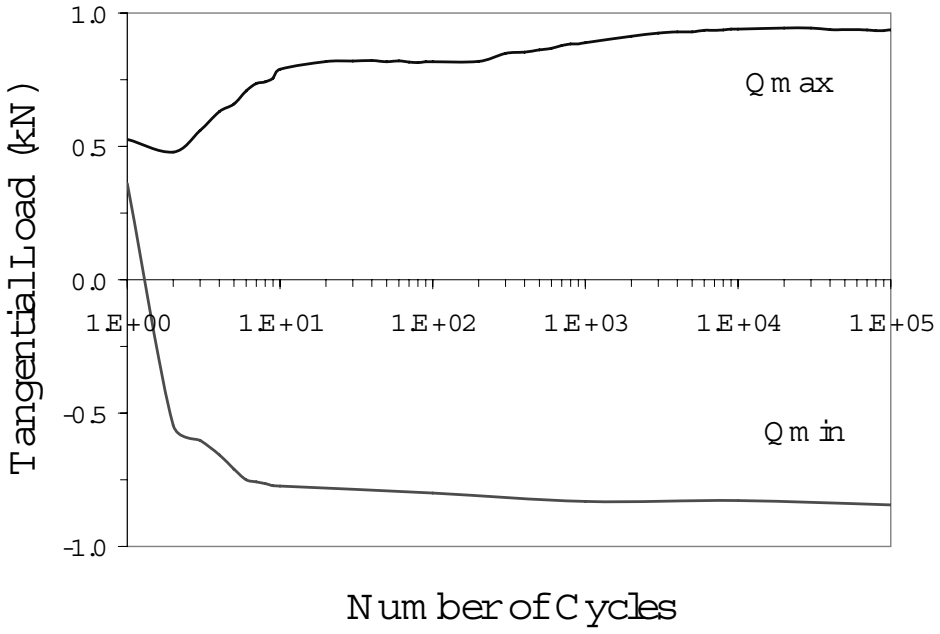

Figure 5.2: Tangential Load vs. Number of Cycles run for test #2

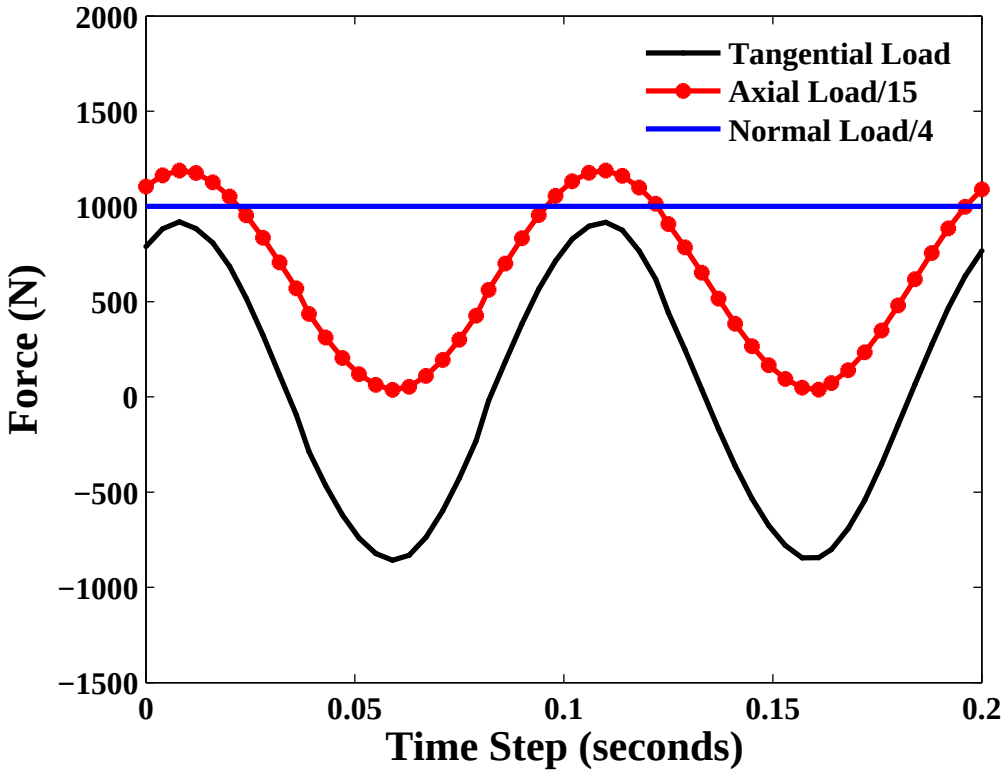

Figure 5.3: Sinusoidal Pattern of Tangential Load and Axial Load at 400,000 cycle for test #2

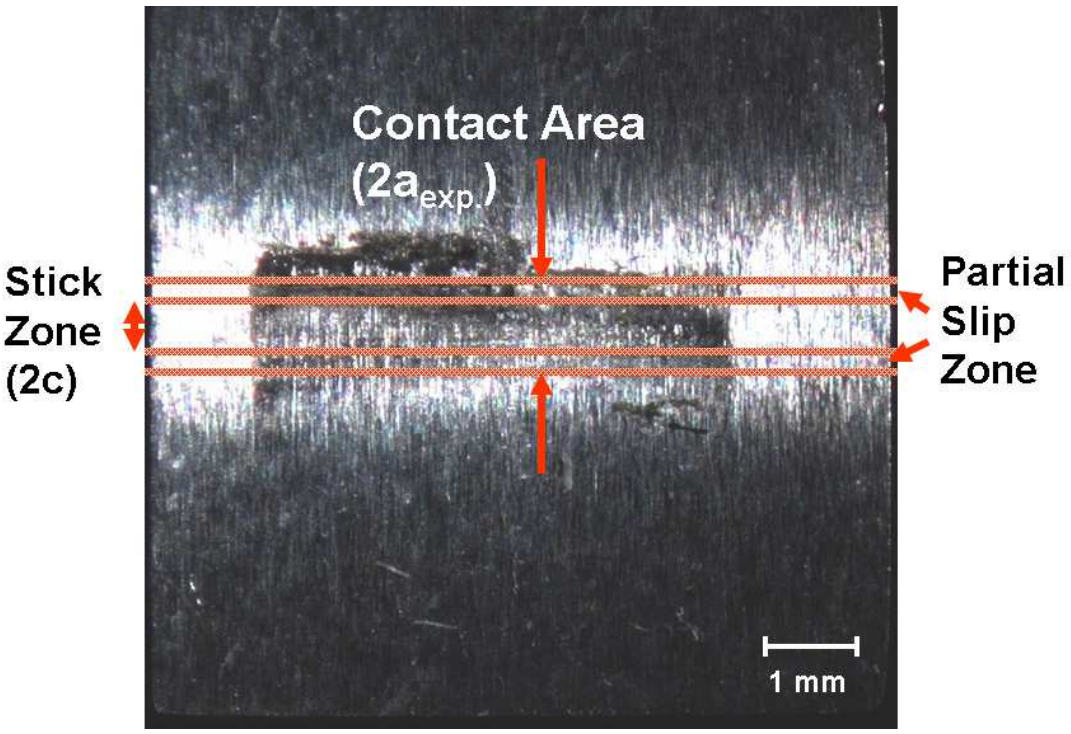

Figure 5.4: Fretted Scar on the 50.8 mm pads (test #5)

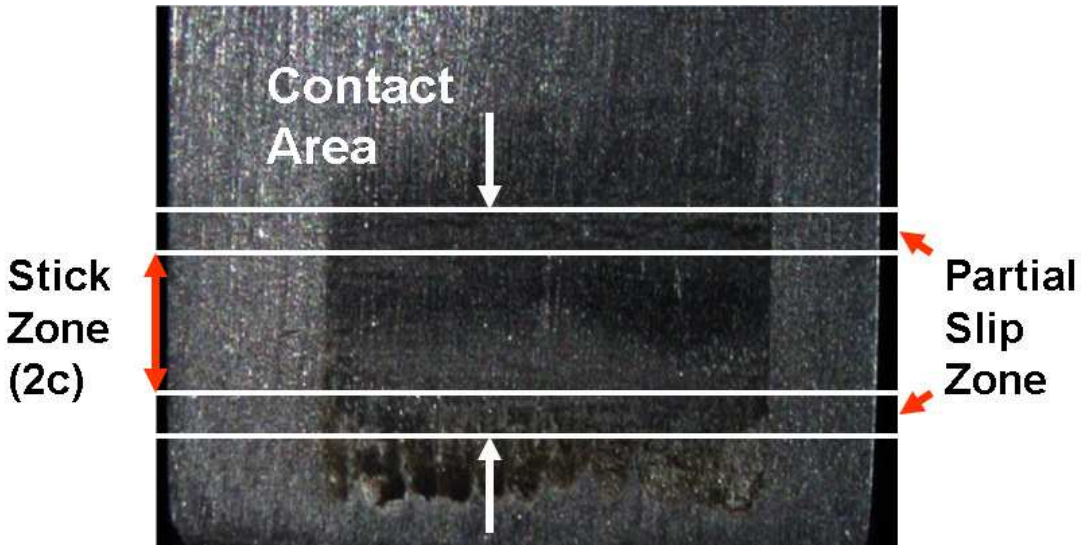

Figure 5.5: Fretted Scar on the 304.8 mm pads (test #9)

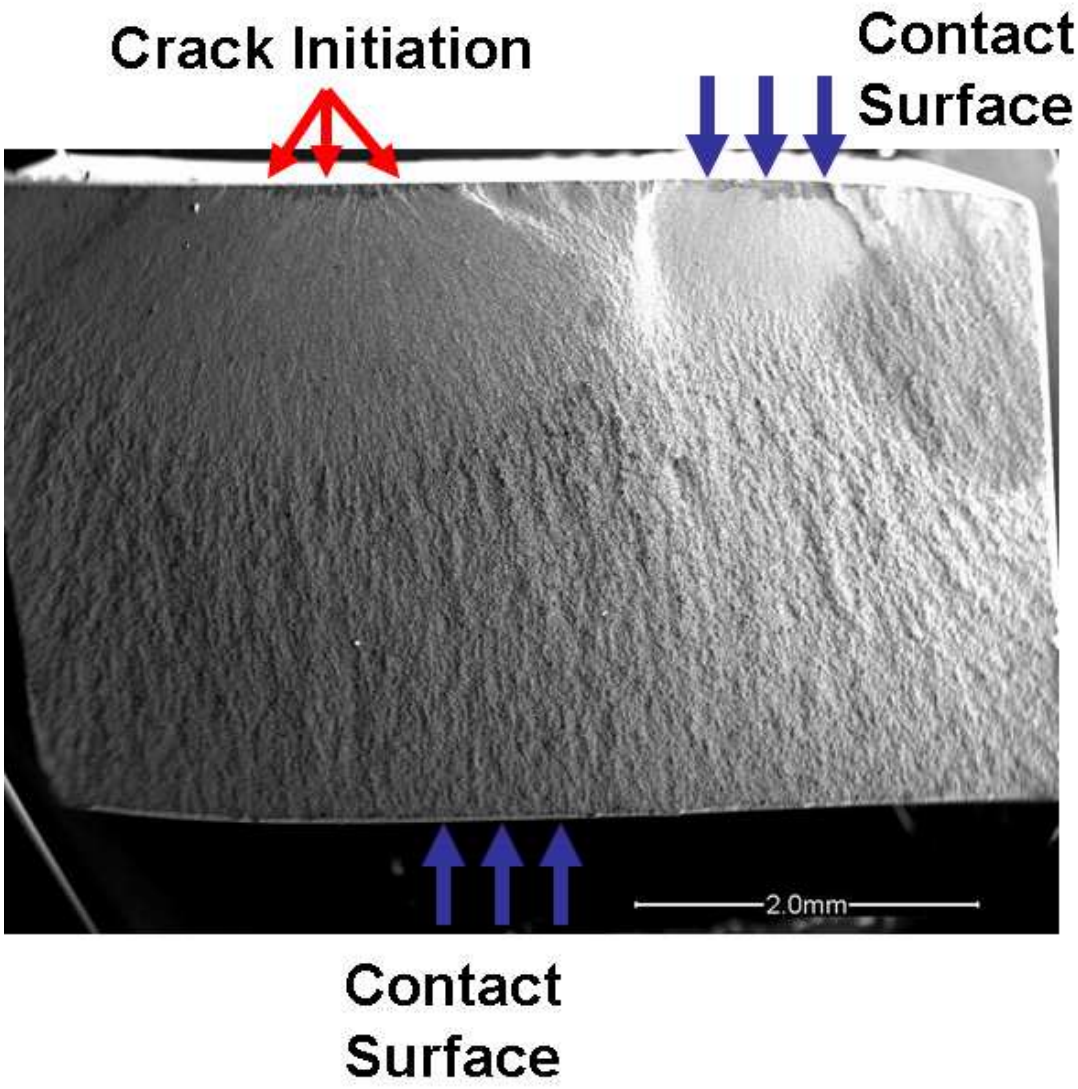

Figure 5.6: Crack Initiation Observed on Contact Surface (at Lower Magnification) (test #4)

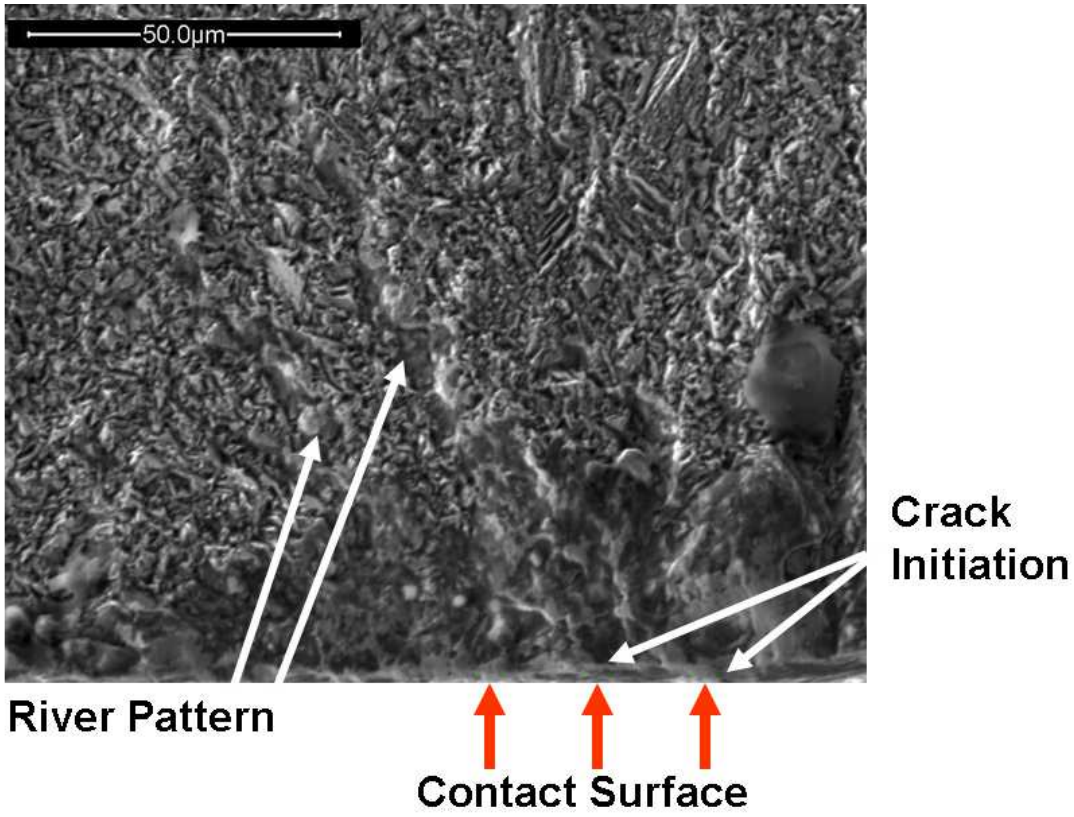

Figure 5.7: Crack Initiation Observed on Contact Surface (at Higher Magnification) (test #4)

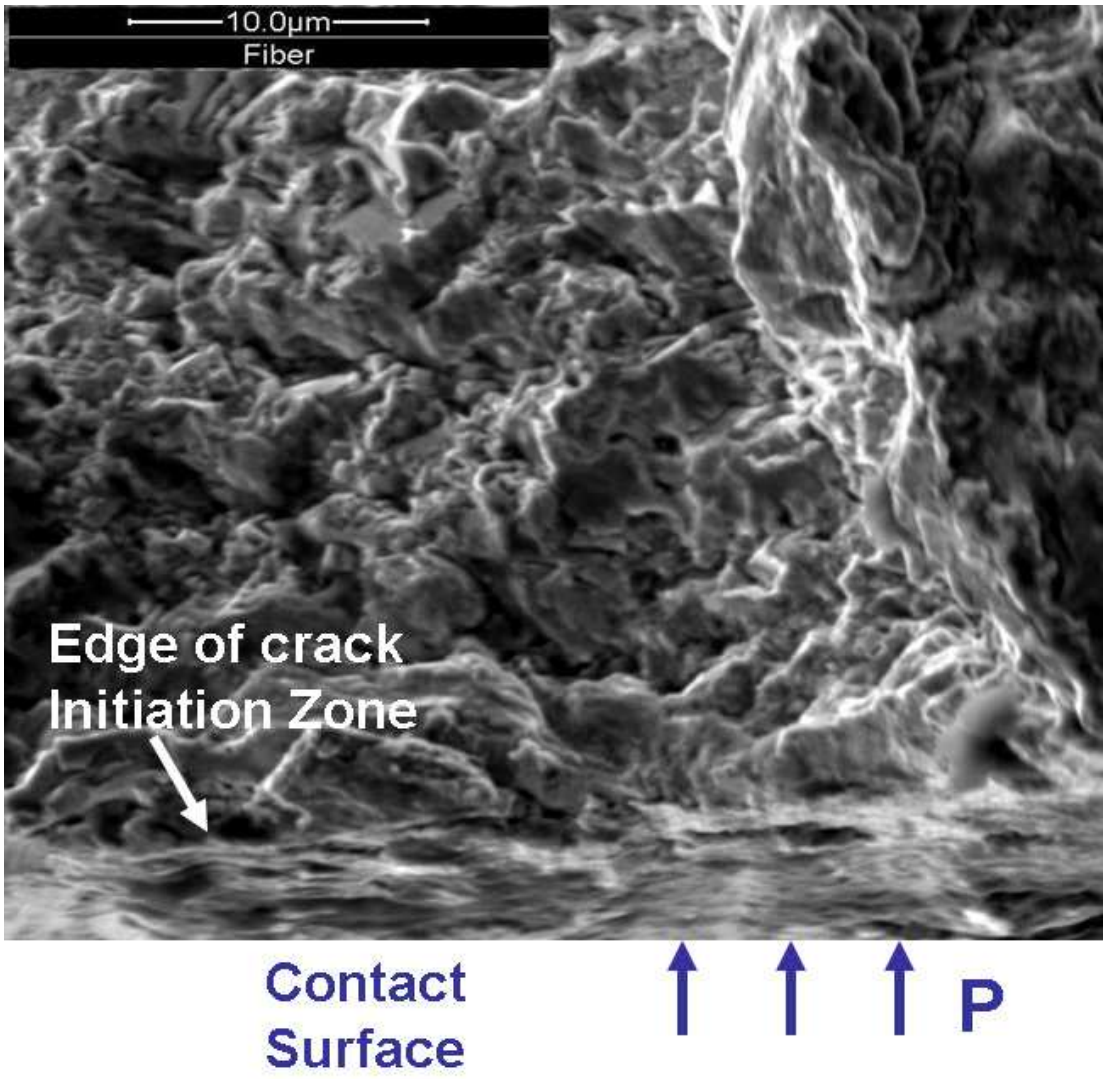

Figure 5.8: Crack Initiation and Stick Edge Zone Observed on Contact Surface (at Very High Magnification) (test #4)

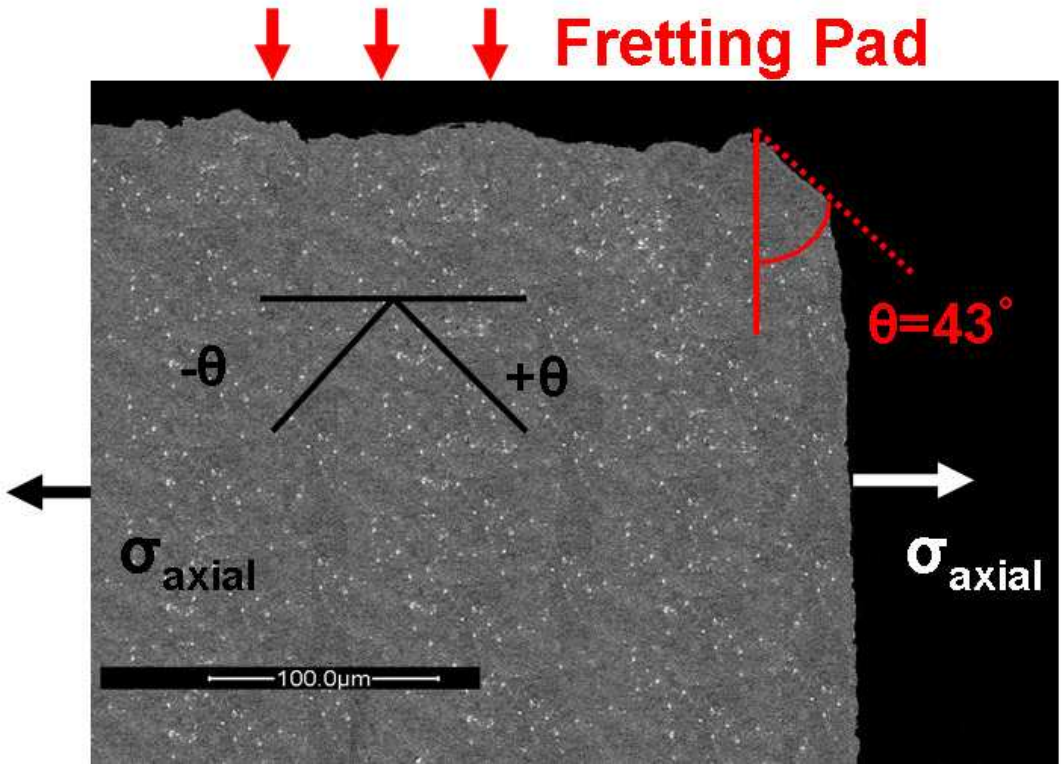

Figure 5.9: Crack Initiation Orientation Angle (test #4)

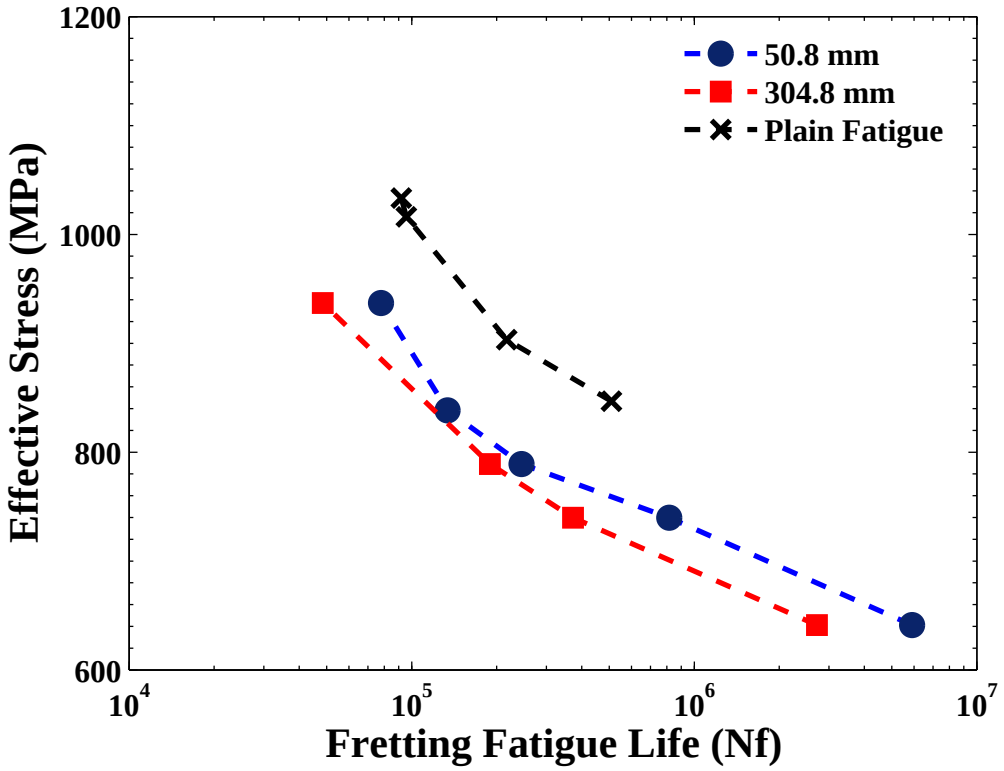

Figure 5.10: Stress Level versus Cycles to failure for all test experiments

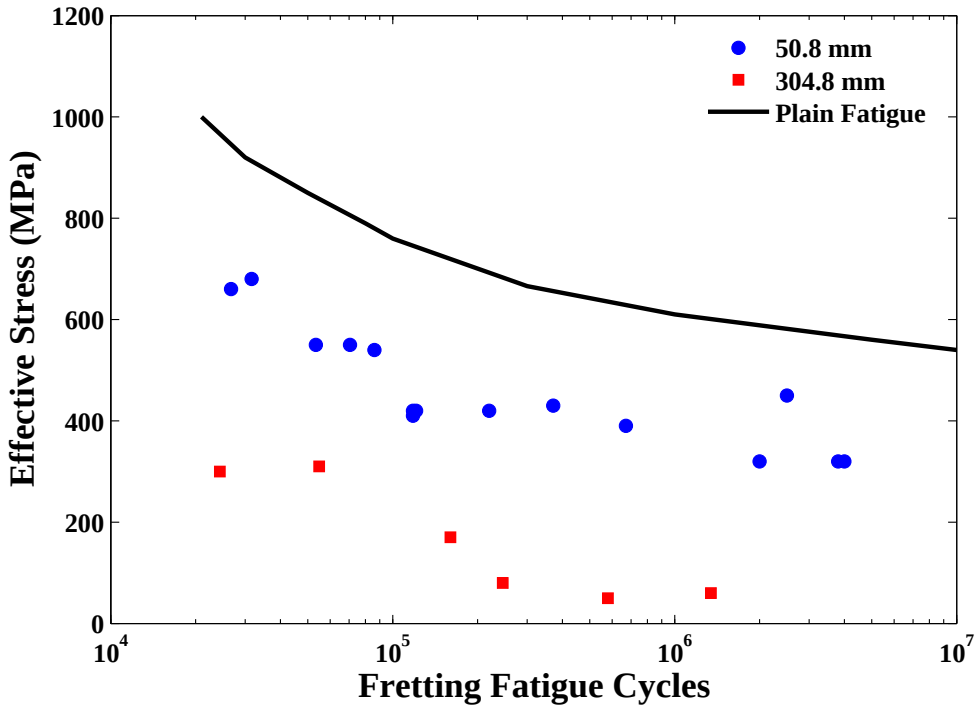

Figure 5.11: Effective Stress versus Fretting Fatigue Life relationships for Ti-6Al-4V

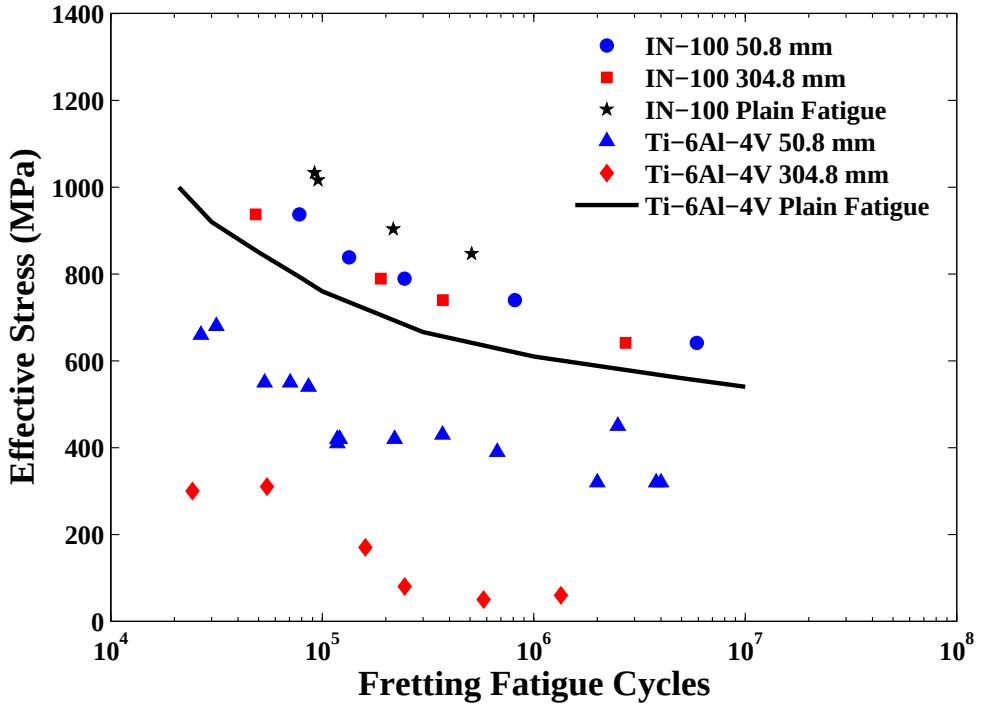

Figure 5.12: Effective Stress versus Fatigue Life relationships for IN-100 and Ti-6Al-4V Alloys

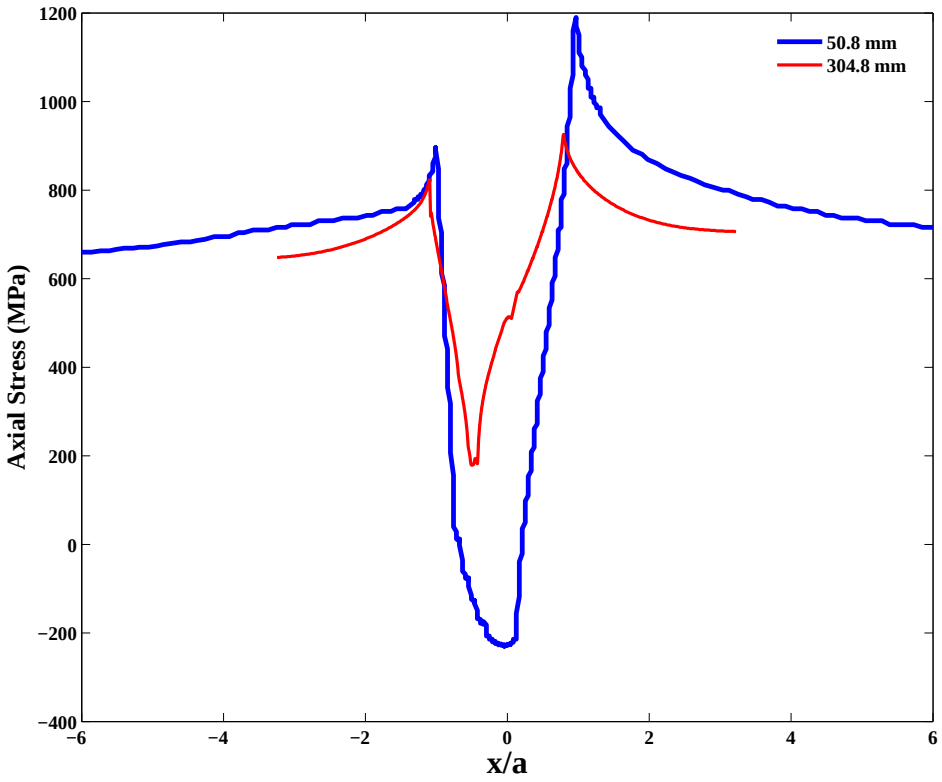

Figure 5.13: Axial Stress versus Location along the contact area for both pad radii for maximum bulk stress of 800 MPa

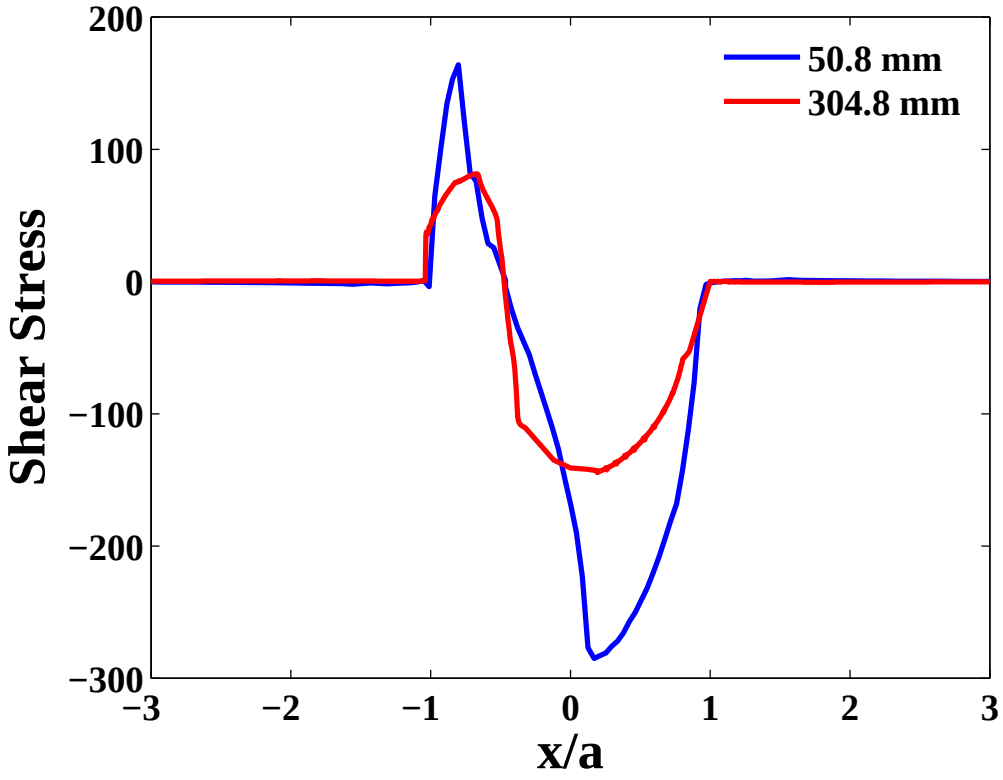

Figure 5.14: Shear Stress versus Location along the contact area for both pad radii for maximum bulk stress of 800 MPa

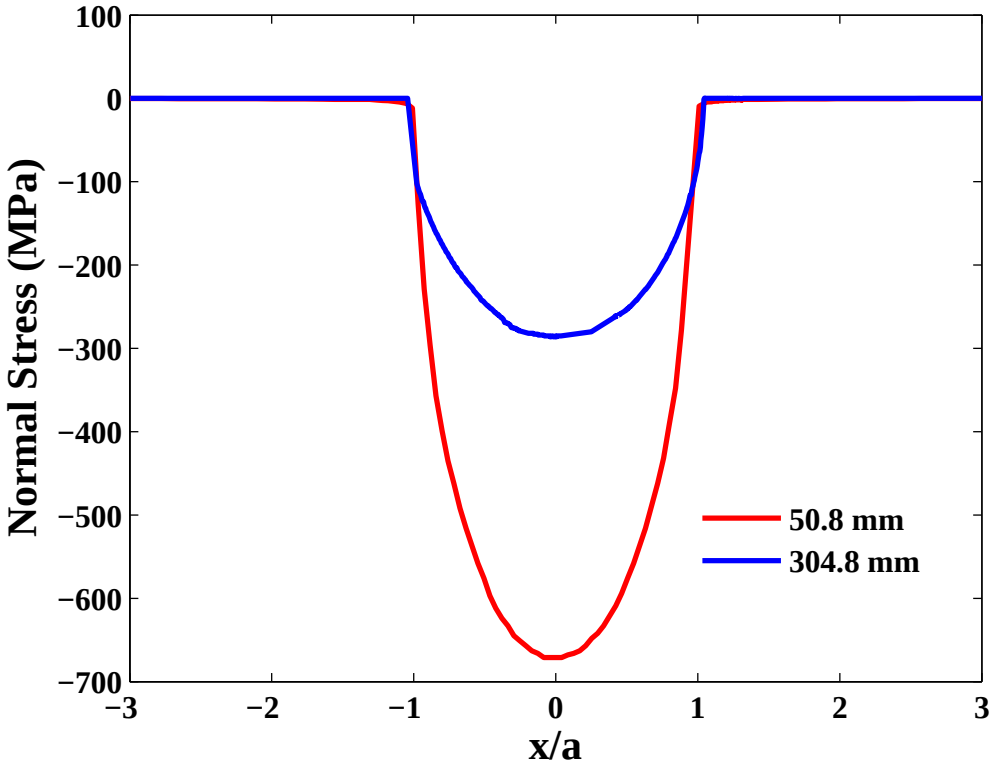

Figure 5.15: Normal Stress versus Location along the contact area for both pad radii for maximum bulk stress of 800 MPa

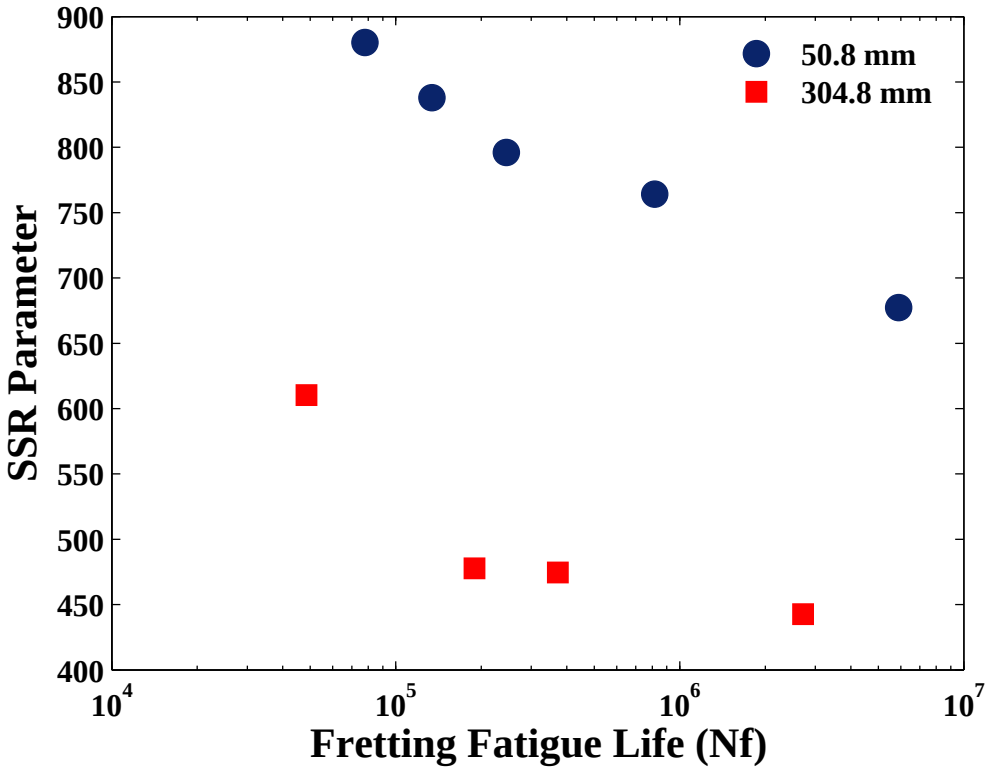

Figure 5.16: Shear Stress Range Distribution versus Fretting Fatigue Life

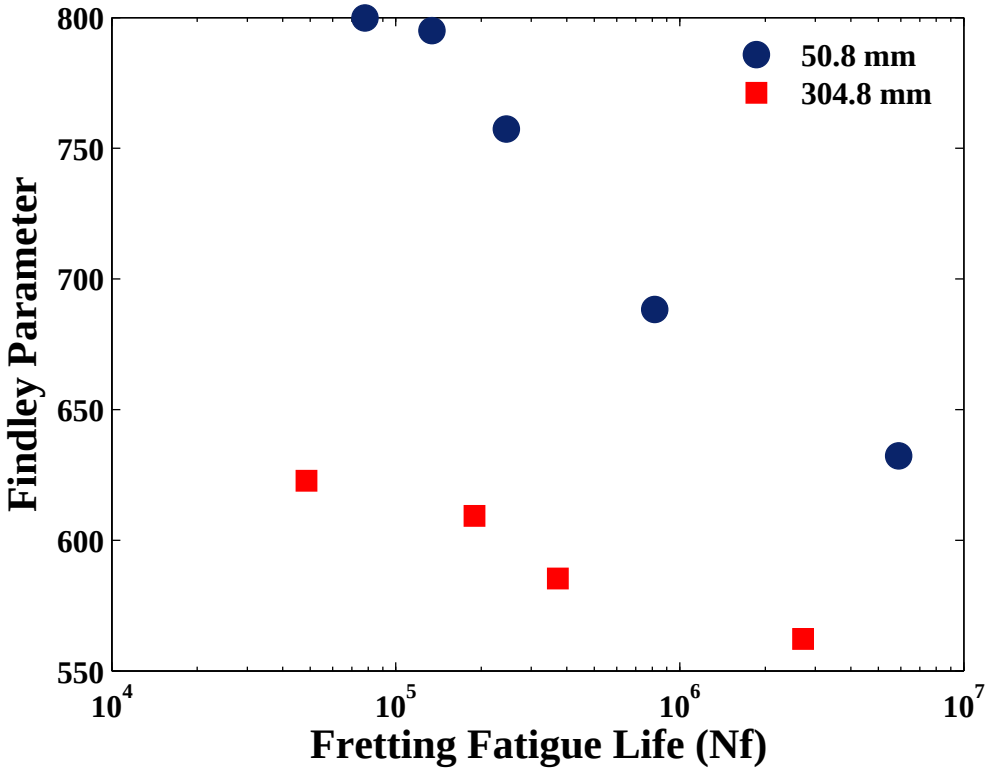

Figure 5.17: Findley Parameter Distribution versus Fretting Fatigue Life

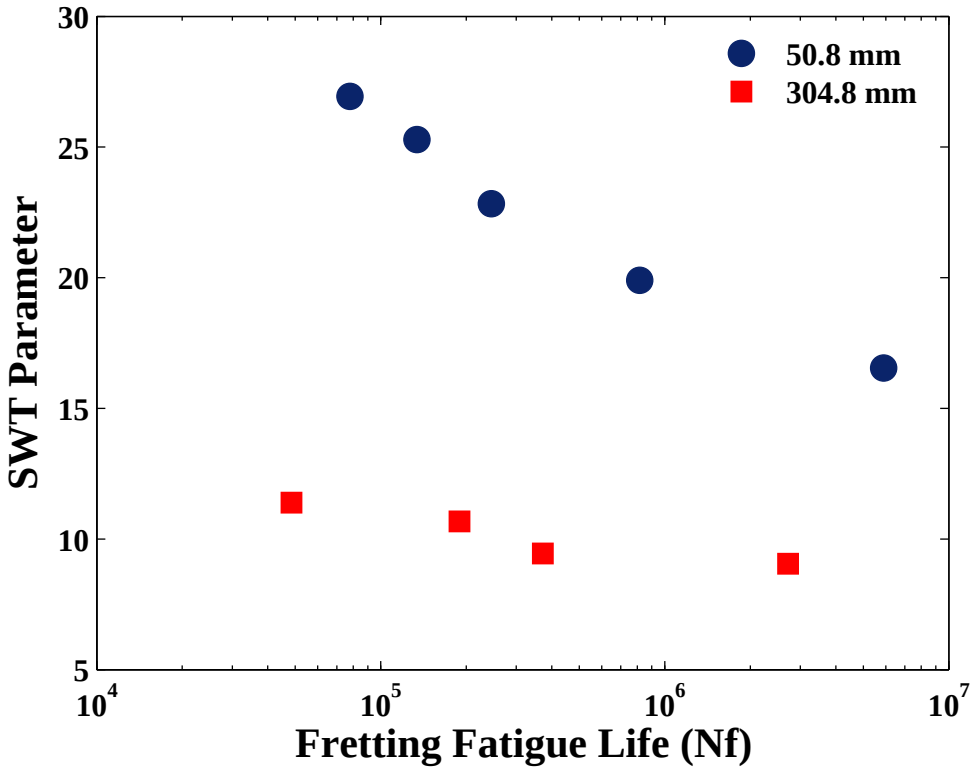

Figure 5.18: SWT parameter versus Fretting Fatigue Life

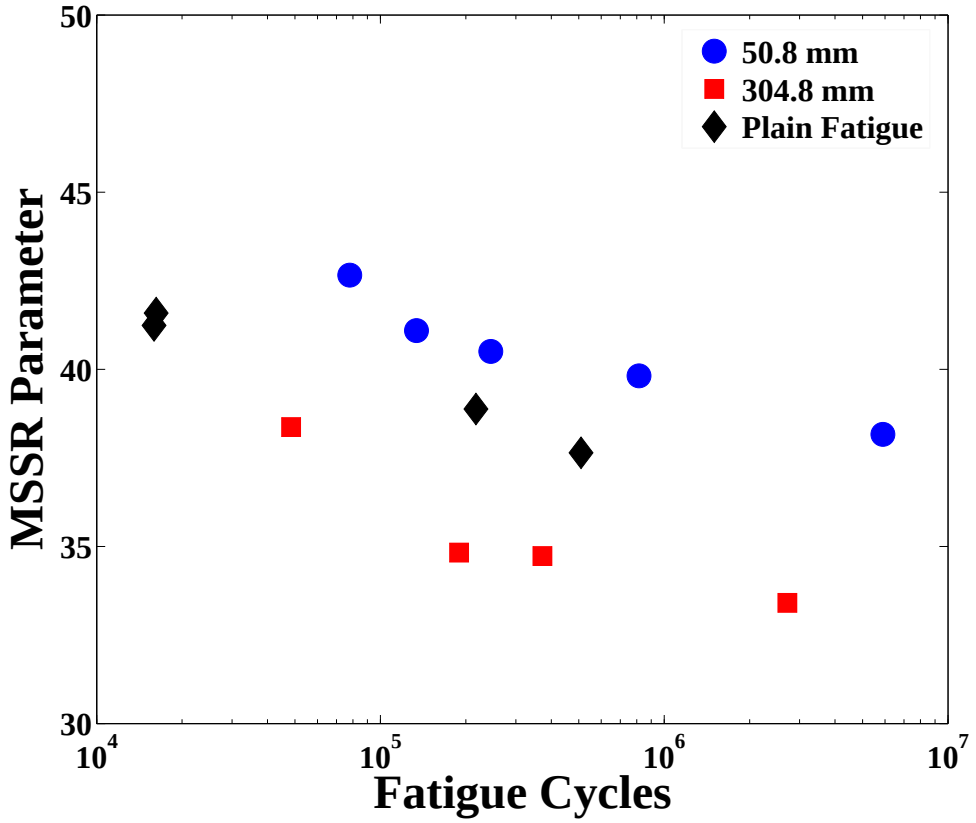

Figure 5.19: Modified Shear Stress Range (MSSR) parameter versus Fretting Fatigue Life (A=0.75, B=0.5, C=0.75, D=0.5) for IN-100

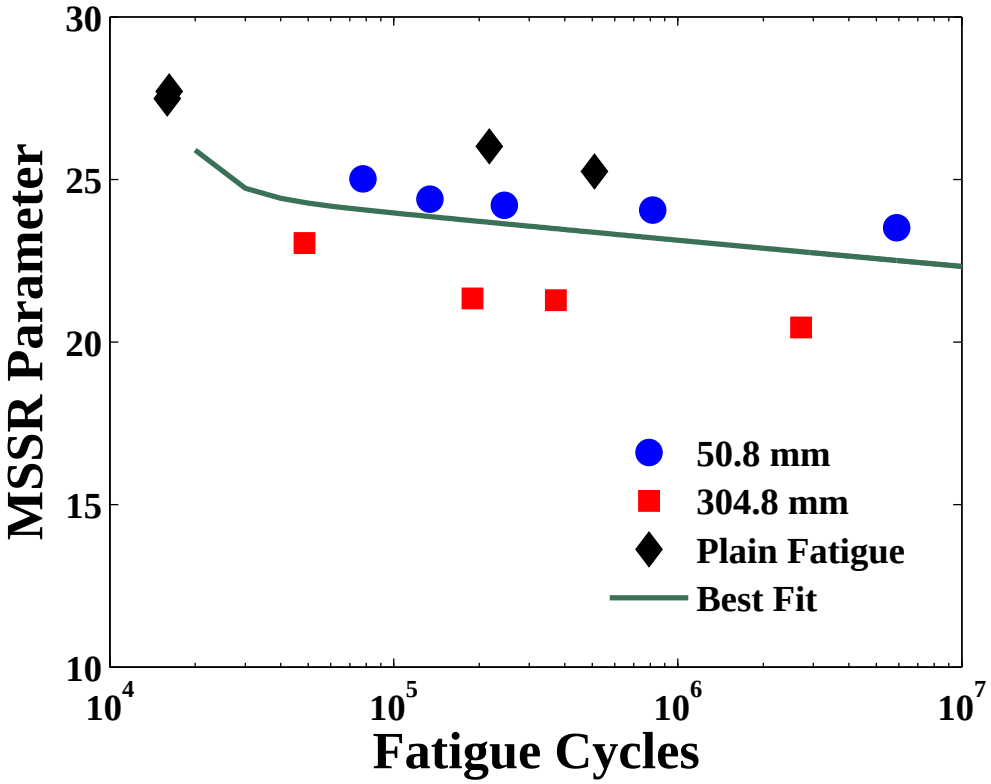

Figure 5.20: Modified Shear Stress Range (MSSR) parameter versus Fretting Fatigue Life (A=0.75, B=0.25, C=0.75, D=0.5) for IN-100

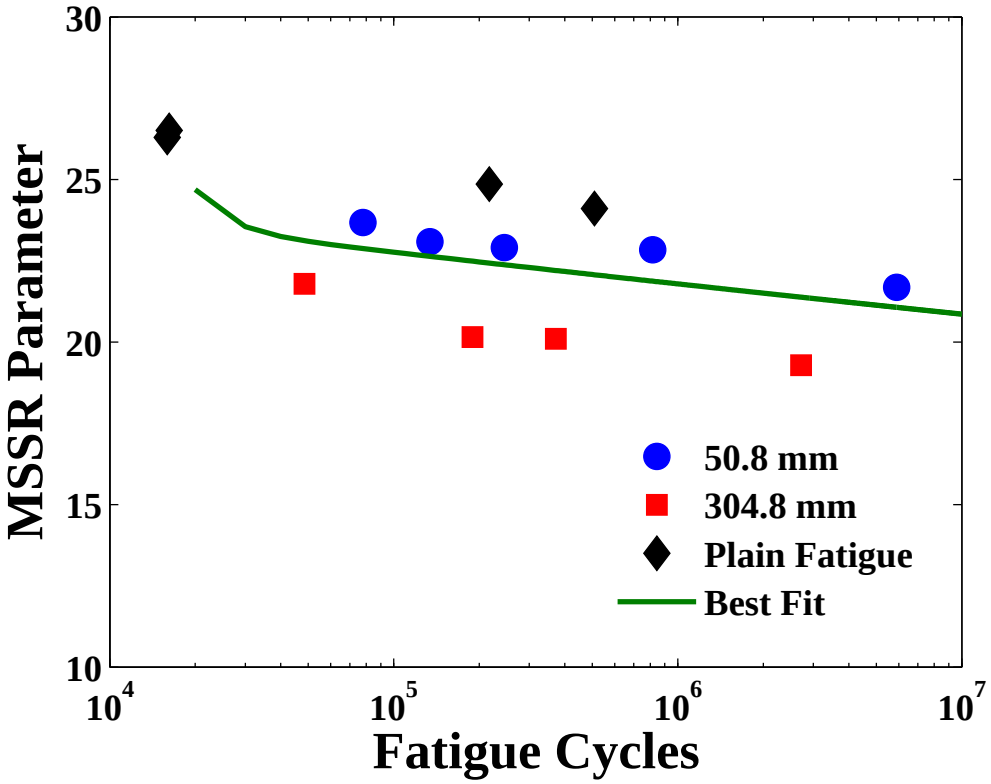

Figure 5.21: Modified Shear Stress Range (MSSR) parameter versus Fretting Fatigue Life (A=0.5, B=0.25, C=0.75, D=0.5) for IN-100

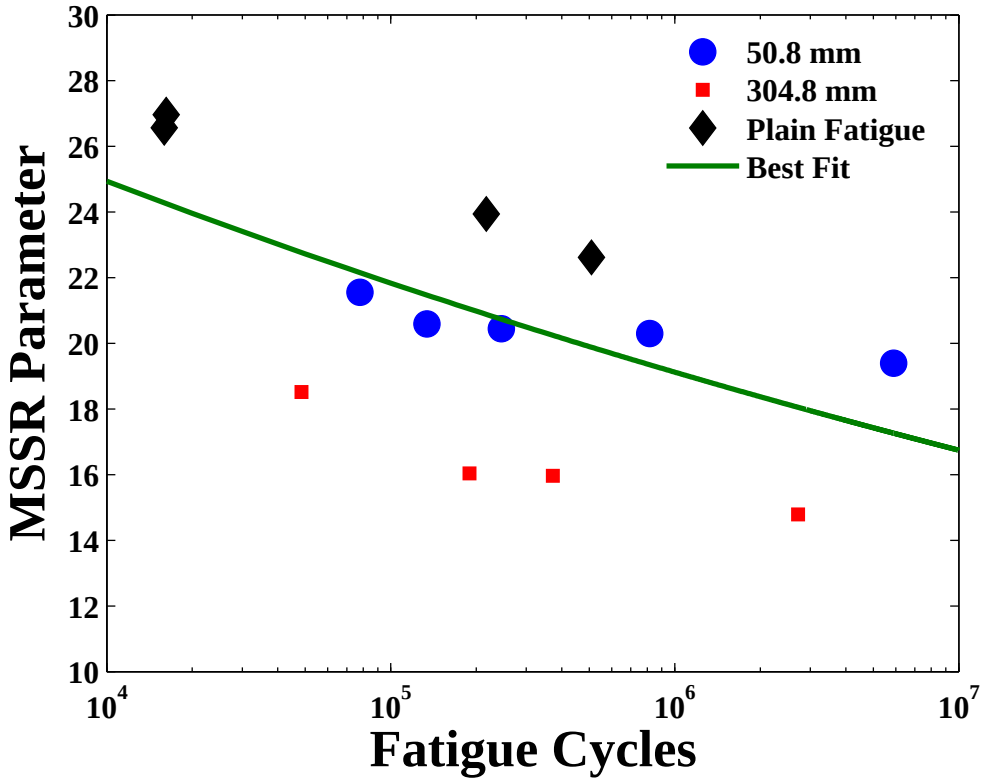

Figure 5.22: Modified Shear Stress Range (MSSR) parameter versus Fretting Fatigue Life (A=0.05, B=0.5, C=0.05, D=0.9) for IN-100

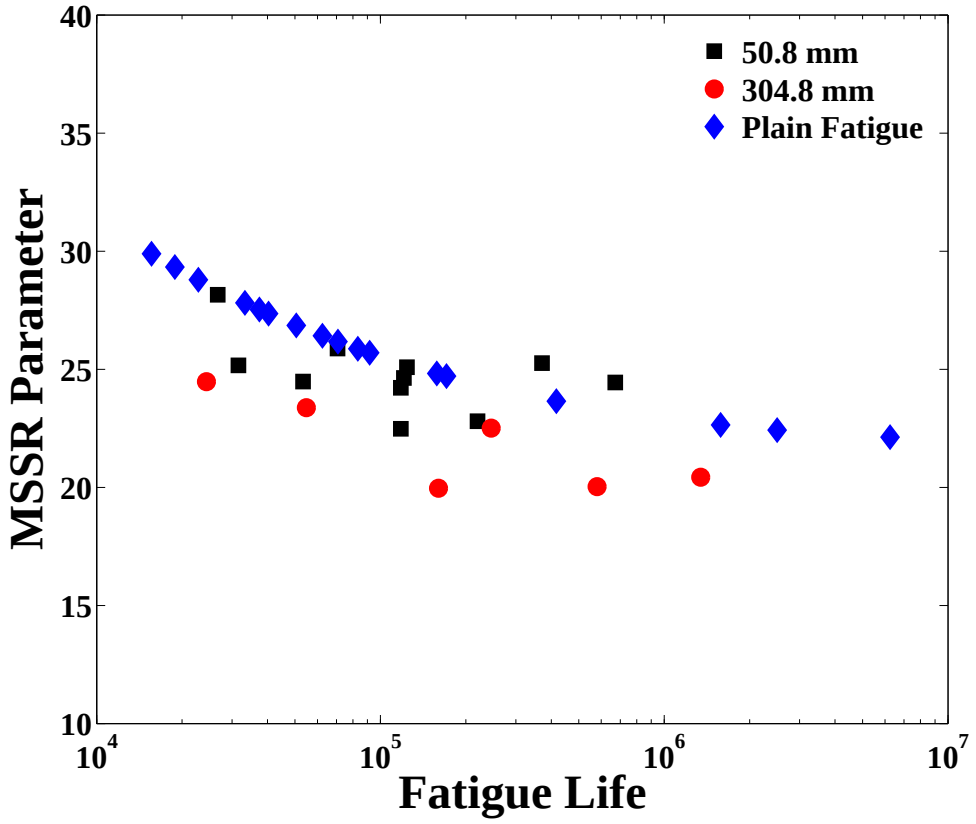

Figure 5.23: Modified Shear Stress Range (MSSR) parameter versus Number of Cycles (A=0.75, B=0.5, C=0.75, D=0.5) for Ti-6Al-4V alloy

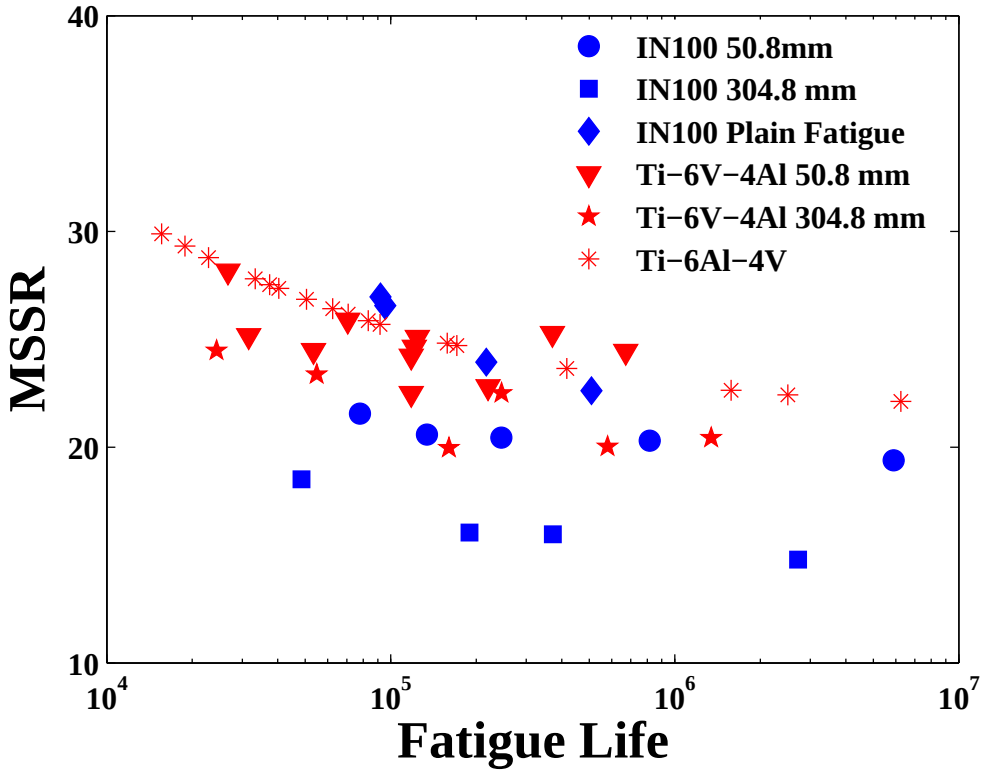

Figure 5.24: Modified Shear Stress Range (MSSR) parameter versus Number of Cycles for IN-100 and Ti-6Al-4V alloys

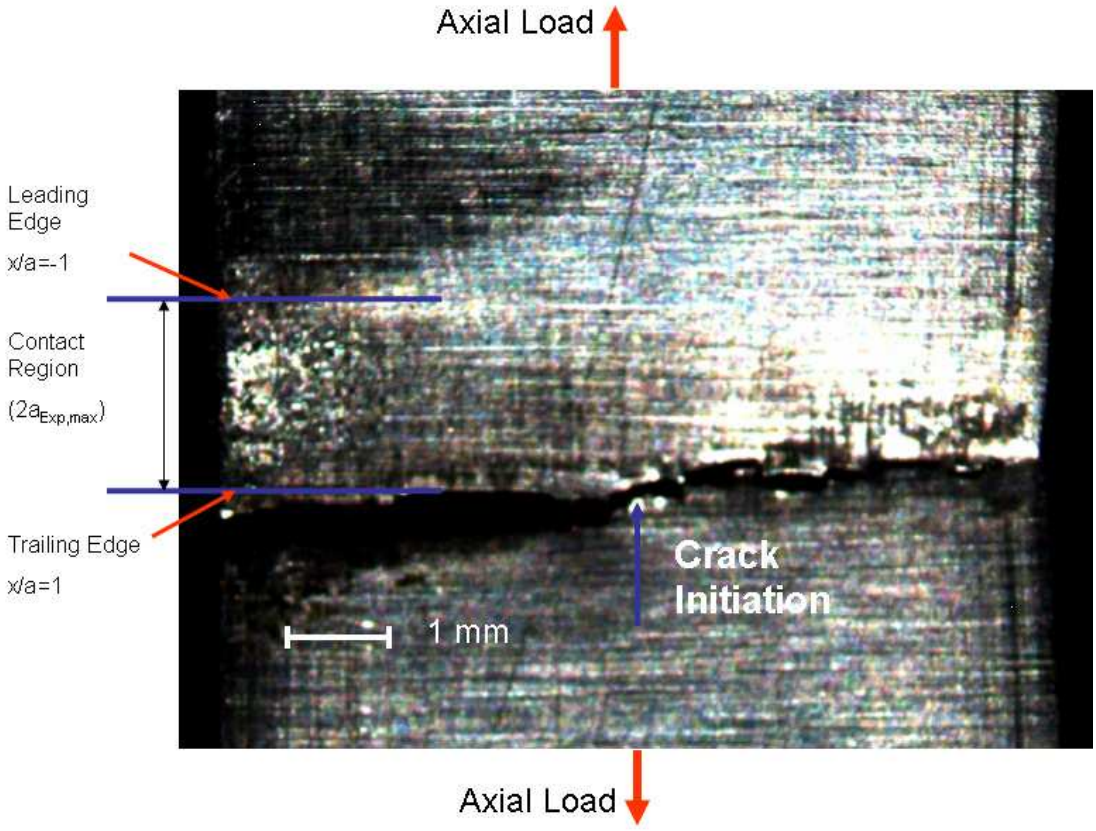

Figure 5.25: Crack Initiation Location (test #9)

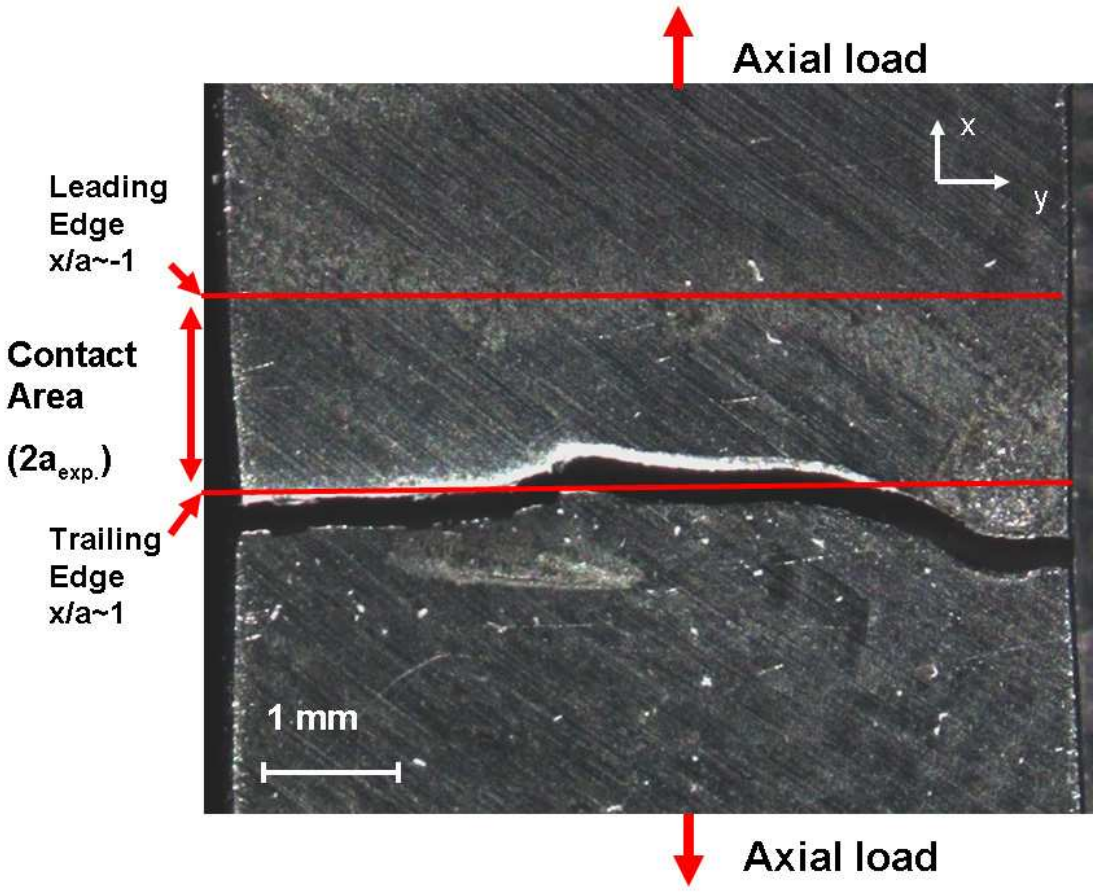

Figure 5.26: Crack Initiation Location (test #9)

Table 5.1: Experimental Test Results

Test	Pad	P	σ_{eff}	Q_{max}	Q_{min}	N_f
	mm	N	(MPa)	(N)	(N)	(Cycles)
1	50.8	4003	641.15	546.78	-643.44	5,900,000
2	50.8	4003	739.79	788.98	-773.46	815,449
3	50.8	4003	789.11	1 139.75	-1 081.67	245,000
4	50.8	4003	838.43	1 225.67	-1 028.96	134,103
5	50.8	4003	937.07	898.63	-706.73	77,937
6	304.8	4003	641.15	439.64	-547.92	2,717,287
7	304.8	4003	739.79	798.91	-807.3	372,173
8	304.8	4003	789.11	648.26	-862.41	189,304
9	304.8	4003	937.07	678.37	-709.66	48,457
10*	-	0	739.79	-	-	509,166
11*	-	0	789.11	-	-	216,993
12*	-	0	887.75	-	-	95,671
13*	-	0	986.39	-	-	91,950

Table 5.2: FEA Input Data

Test #	Pad Radius mm	Step	Contact Pressure MPa	Shear Pressure MPa	Bulk stress MPa
1	50.8	max	66.19	12.80	642.86
1	50.8	min	66.19	-11.63	19.63
2	50.8	max	66.19	15.98	737.16
2	50.8	min	66.19	-14.07	23.11
3	50.8	max	66.19	19.30	786.36
3	50.8	min	66.19	-18.31	23.52
4	50.8	max	66.19	20.75	840.78
4	50.8	min	66.19	-17.42	25.35
5	50.8	max	66.19	15.69	939.43
5	50.8	min	66.19	-12.34	28.08
6	304.8	max	66.19	7.39	641.37
6	304.8	min	66.19	-9.27	21.12
7	304.8	max	66.19	13.53	721.75
7	304.8	min	66.19	-13.67	21.00
8	304.8	max	66.19	10.98	780.76
8	304.8	min	66.19	-14.60	21.37
9	304.8	max	66.19	11.49	942.91
9	304.8	min	66.19	-12.02	28.45

Table 5.3: SSR Parameter Results

Pad	Test	SSR	θ	σ_{max}	σ_{min}	$a_{pred.}$	$a_{exp.}$	Difference
mm		MPa	degree	MPa	MPa	m	m	%
50.8	1	677.31	-90	670.16	-156.47	0.00059	0.00060	-3.16
50.8	2	764.14	-90	697.60	-191.75	0.00058	0.00060	-3.16
50.8	3	796.12	-90	733.68	-166.83	0.00059	0.00060	-2.13
50.8	4	837.90	46.4	744.40	-148.20	0.00060	0.00060	-1.11
50.8	5	880.24	-90	783.17	-199.36	0.00055	0.00060	-8.32
304.8	6	442.61	45.4	501.43	-127.96	0.0013	0.0015	-9.43
304.8	7	474.63	44.6	548.24	-126.24	0.0014	0.0015	-8.13
304.8	8	477.82	43.1	557.91	-114.07	0.00134	0.0015	-5.55
304.8	9	610.38	44.6	659.91	-156.28	0.0013	0.0015	-10.76

Table 5.4: Findley Parameter Results

Pad	Test	FP	θ	τ_{max}	τ_{min}	$x/a_{pred.}$	$a_{exp.}$	Difference
mm		MPa	degree	MPa	MPa	m	m	%
50.8	1	632.31	152.40	474.41	-116.93	0.0006	0.0006	-4.19
50.8	2	688.34	153.60	537.84	-126.87	0.0006	0.0006	-5.23
50.8	3	757.40	153.60	587.35	-147.90	0.0006	0.0006	-7.29
50.8	4	795.00	153.20	614.89	-164.03	0.0006	0.0006	-7.29
50.8	5	799.84	153.40	626.59	-122.48	0.0006	0.0006	-6.26
304.8	6	562.21	150.50	440.01	-116.31	0.0014	0.0015	-5.80
304.8	7	585.40	153.30	441.06	54.52	0.0013	0.0015	-11.88
304.8	8	609.35	157.10	388.37	-170.84	0.0013	0.0015	-11.90
304.8	9	622.79	153.50	534.35	52.35	0.0013	0.0015	-11.57

Table 5.5: SWT Parameter Results

Pad	Test	SWT_{max}	σ_{max}	σ_{min}	θ	$a_{pred.}$	$a_{exp.}$	Difference
mm		MPa	MPa	MPa	deg	m	m	%
50.8	1	16.54	1928.75	-315.20	1.20	5.71E-04	0.0006	-5.23
50.8	2	19.90	2058.56	-379.64	1.10	5.71E-04	0.0006	-5.23
50.8	3	22.83	2190.79	-436.78	1.00	5.71E-04	0.0006	-5.23
50.8	4	25.29	2309.76	-451.18	0.90	5.71E-04	0.0006	-5.23
50.8	5	26.94	2456.51	-309.36	0.90	5.71E-04	0.0006	-5.23
304.8	6	9.05	1500.14	-22.31	0.20	1.28E-03	0.0015	-13.51
304.8	7	9.45	1533.92	-19.76	179.90	1.17E-03	0.0015	-20.40
304.8	8	10.67	1619.95	-42.32	179.70	1.23E-03	0.0015	-16.95
304.8	9	11.39	1524.88	-358.19	1.20	5.64E-04	0.0015	-61.76

Table 5.6: MSSR Parameter Results in Original Version (A=0.75, B=0.5, C=0.75, D=0.5)

Pad	Test	MSSR	θ	$a_{pred.}$	$a_{exp.}$	Difference
mm		MPa	degree	m	m	%
50.8	1	38.16	138.00	0.0006	0.00060	-3.16
50.8	2	39.82	138.80	0.0006	0.00060	-3.16
50.8	3	40.50	137.90	0.0006	0.00060	-2.13
50.8	4	41.09	137.20	0.0006	0.00060	-1.11
50.8	5	42.66	139.70	0.0006	0.00060	-8.32
304.8	6	33.40	45.40	0.0013	0.0015	-9.43
304.8	7	34.73	44.60	0.0014	0.0015	-8.13
304.8	8	34.83	43.10	0.0014	0.0015	-5.55
304.8	9	38.37	44.60	0.0013	0.0015	-10.72

Table 5.7: MSSR Parameter Results Version 1 (A=0.75, B=0.25, C=0.75, D=0.5)

Pad	Test	MSSR	θ	σ_{max}	σ_{min}	$a_{pred.}$	$a_{exp.}$	Difference
mm		–	degree	MPa	MPa	m	m	%
50.8	1	23.52	133.20	700.74	-179.55	0.00056	0.00060	-7.29
50.8	2	24.06	133.30	740.20	-197.48	0.00055	0.00060	-8.32
50.8	3	24.21	137.90	733.68	-166.83	0.00059	0.00060	-2.13
50.8	4	24.40	137.20	744.40	-148.20	0.00060	0.00060	-1.11
50.8	5	25.02	139.70	783.17	-199.36	0.00055	0.00060	-8.32
304.8	6	20.45	45.00	511.21	-110.36	0.0014	0.0015	-8.56
304.8	7	21.29	44.30	558.78	-109.26	0.0014	0.0015	-6.84
304.8	8	21.34	43.60	561.42	-116.41	0.0013	0.0015	-11.47
304.8	9	23.05	44.60	659.91	-156.28	0.0013	0.0015	-10.72

Table 5.8: MSSR Parameter Results Version 2 (A=0.5, B=0.25, C=0.75 and D=0.5)

Pad	Test	MSSR	θ	σ_{max}	σ_{min}	$a_{pred.}$	$a_{exp.}$	Difference
mm		–	degrees	MPa	MPa	-	m	%
50.8	1	21.69	34.4	666.12	188.35	0.0006	0.0006	-2.84
50.8	2	22.84	133.30	740.20	-197.48	0.0006	0.0006	-8.32
50.8	3	22.91	137.90	733.68	-166.83	0.0006	0.0006	-2.13
50.8	4	23.085	137.20	744.40	-148.20	0.0006	0.0006	-1.11
50.8	5	23.68	139.70	783.17	-199.36	0.0006	0.0006	-8.32
304.8	6	19.29	45.00	511.21	-110.36	0.0013	0.0015	-8.56
304.8	7	20.10	44.30	558.78	-109.26	0.0014	0.0015	-6.84
304.8	8	20.15	43.60	561.42	-116.41	0.0013	0.0015	-11.90
304.8	9	21.79	44.60	659.91	-156.28	0.0013	0.0015	-10.72

VI. Conclusions and Recommendations

6.1 Summary

Much work has been done in the area of fretting fatigue on titanium based alloys, but only a few have been devoted to investigate the fretting fatigue behavior of nickel based superalloys. In reality, this material is used extensively in the engine hot section, in the same hostile environment as titanium alloys. Therefore, understanding the behavior of nickel based superalloys is of equal importance, since this will allow turbine design engineers to predict its effects and make a more efficient engine, and optimize the fretting fatigue life of the concerned components. The main objective of this study was to systematically investigate the fretting fatigue behavior of polycrystalline nickel alloy, IN-100 under room temperature.

Thirteen fatigue tests were conducted, nine of them were under fretting fatigue condition. The first five fretting fatigue experiments were accomplished with a 50.8 mm pad configuration while the last four were made with 304.8 mm pads. Fretting fatigue tests were conducted over a wide range of maximum stresses, σ_{max}=650 to 950 MPa with stress ration of R = 0.03. The axial load was controlled via the 22.2 kN servo-hydraulic load frame. The axial load variation that the test specimen undergoes during the test runs are measured by load cells attached to the servo-hydraulic load frame. This actuator is controlled by Multi-Purpose Test Software (MPT) which allows the user to choose the magnitude, frequency, and waveform of the applied axial load. Applied load outputs were monitored and recorded continuously until failure of specimens, and the resulting tangential loads were determined as half the difference between lower and upper axial loads. These experimental values, in conjunction with the normal and axial stress conditions, were used as the inputs for FEA modelling. Also, crack initiation location and orientation angle were investigated using optical and scanning electron microscopy.

To simulate the experimental test setup, finite element analysis was conducted on both pad configurations, using two separate models. These models were validated using the analytical solution formulated by the Ruiz program. These numerical ana-

lyzes were employed to perform a systematic study of the local shear distributions. In addition, using the numerical analysis outputs, four fretting fatigue parameters, shear stress range (SSR), Findley parameter, Smith-Watson-Topper (SWT) parameter and MSSR parameter, were evaluated based on their ability to predict fretting fatigue life without dependence on pad geometry, crack location and crack initiation orientation angle. The experimental and numerical results were compared and discussed in light of the fretting fatigue behavior database accumulated in previous studies conducted on a titanium-based alloy Ti-6Al-4V, that operates in similar engine conditions.

6.2 Conclusions

1. As a function of effective stress, fretting fatigue data exhibits a much shorter fatigue life than its plain fatigue counterpart. Fatigue endurance limit was significantly reduced by the presence of fretting, i.e. the introduction of a normal load. So in essence, IN-100 behavior under fretting fatigue does confirm the general premise of degradation, observed in other alloys, as compared to plain fatigue.

2. The two pad radii used, 50.8 mm and 304.8 mm, showed very close results in terms of fretting fatigue life, interestingly with less pronounced effect than with the titanium-based alloys. However, the degradation of fretting fatigue endurance is still observed as the pads become flatter.

3. For all experiments under this study, crack initiation location occurred at the trailing edge, at a location of x/a$\sim$ +1.0 along the x-direction.

4. Crack initiation orientation angle was found to be $\pm 45^o$ with a variation of $\pm 10^o$, as was the case in studies conducted on Ti-6Al-4V.

5. Fatigue parameters, SSR, Findley and SWT, investigated in this study, failed to meet all the three criteria for predictive parameter acceptance for IN-100. It is most likely due to the fact that the contribution of normal stress in these parameters, which is not taken into consideration at all in the SSR parameter, is not represented appropriately.

6. By modifying the MSSR constants, this parameter was able to collapse the fretting fatigue data from both pad radii onto a single curve and thus predict fretting fatigue life without dependence on pad geometry. Two versions of this parameter are presented, one with A=0.5, B=0.25, C=0.75 and D=0.5, while the other uses A=0.05, B=0.5, C=0.05 and D=0.9. This demonstrates that although shear stress plays a major role in fretting fatigue, normal stress contribution is not negligible.

7. Finally, the scatter in the MSSR versus fatigue life data in the nickel superalloy, IN-100, was comparable to its counterpart from titanium alloy.

6.3 Recommendations for Future Work

1. This study focused on the fretting fatigue behavior of IN-100 at room temperature for two pad radii. For a judicious and complete investigation of the fretting fatigue behavior of any material, the first step is always to study its behavior at room temperature. All the findings in this work can be considered as the baseline data to be further investigated under more realistic conditions simulating the engine environment. In reality, this material operates at elevated temperature in the engine hot section. As such, further effort should be devoted to investigate SCN and polycrystalline IN-100 fretting fatigue behavior in an environment similar to the conditions of the material operation settings.

2. It might also be interesting to see if the use of heat treatment on specimens before experiment tests makes any difference in the specimen's performance. In effect, it has been suggested by researchers in the field to do heat treat the specimens in order to relax some of the stress concentration developed in the material just from mere machining.

3. Through modification of MSSR constants, this parameter was able to come close to collapsing the two configuration data onto one single curve capable of predicting fretting fatigue data. However, it was clear that there is something else missing in the formulation of the parameter. This could be as simple as the definition of the two

stress components or even a totally different parameter. Therefore, it might be useful to conduct more experiments at room temperature with different contact geometries and loading conditions in order to investigate further.

Appendix A. Mechanical Properties

For the material used in this study, the mechanical properties were determined experimentally. Strain gages were glued to the a specimen to measure the axial and horizontal strains while load was increased incrementally for values below the yield stress. As shown in Fig. A.1 and A.2, analyzing the data obtained from this experiment allowed the author to obtain the following: Modulus of Elasticity=103.15 GPa and Poisson's Ratio=.28.

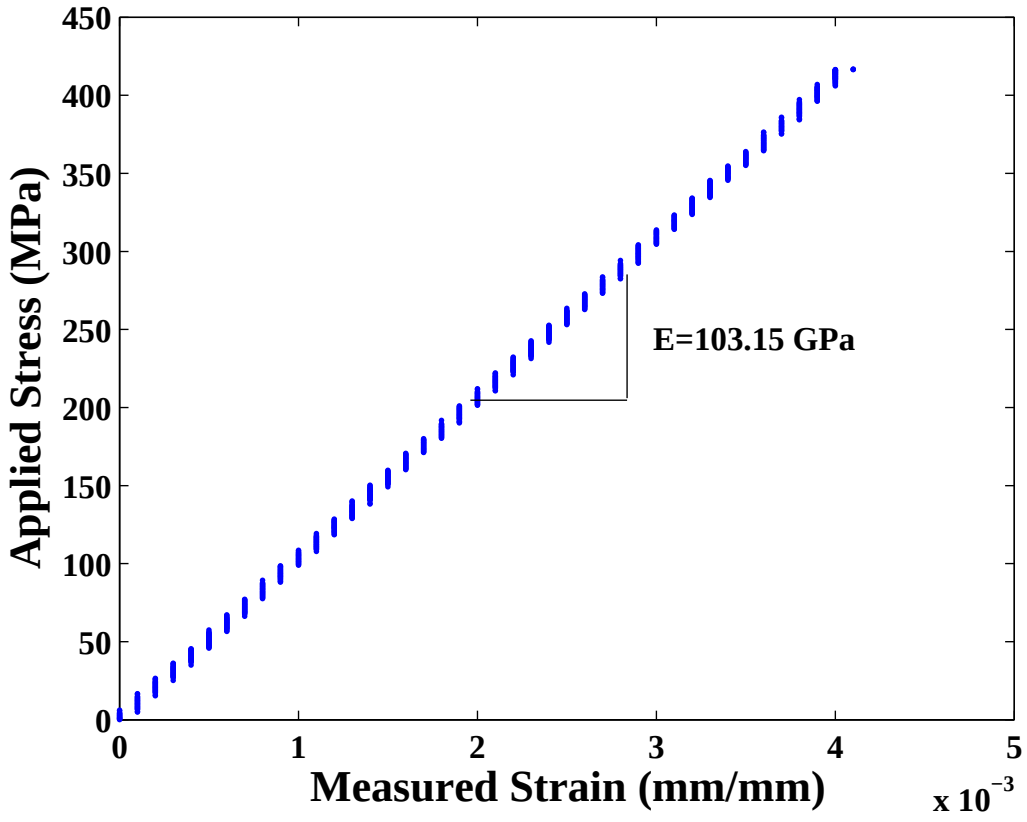

Figure A.1: Applied Stress versus Measured Strain

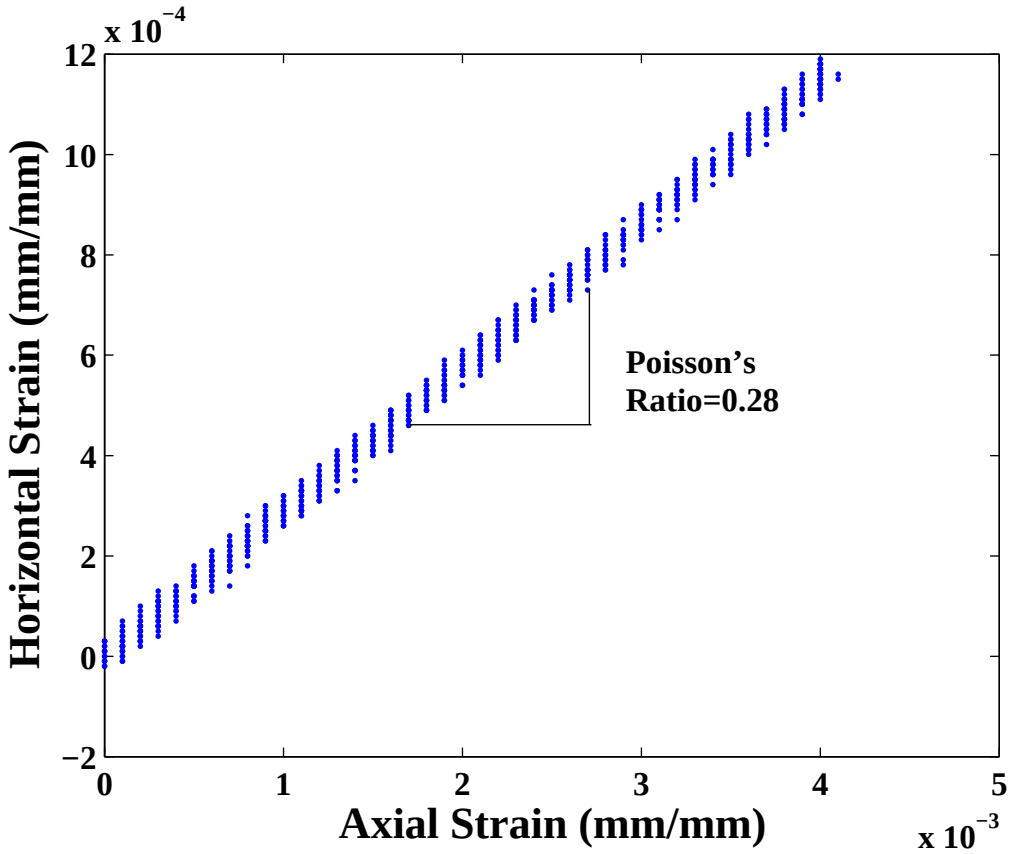

Figure A.2: Horizontal Strain versus Axial Strain

Appendix B. Ti-6Al-4V Stress Profiles

This appendix shows typical stress profiles, σ_{xx}, σ_{xy} and σ_{yy} versus location along the contact area, for Ti-6Al-4V material [3].

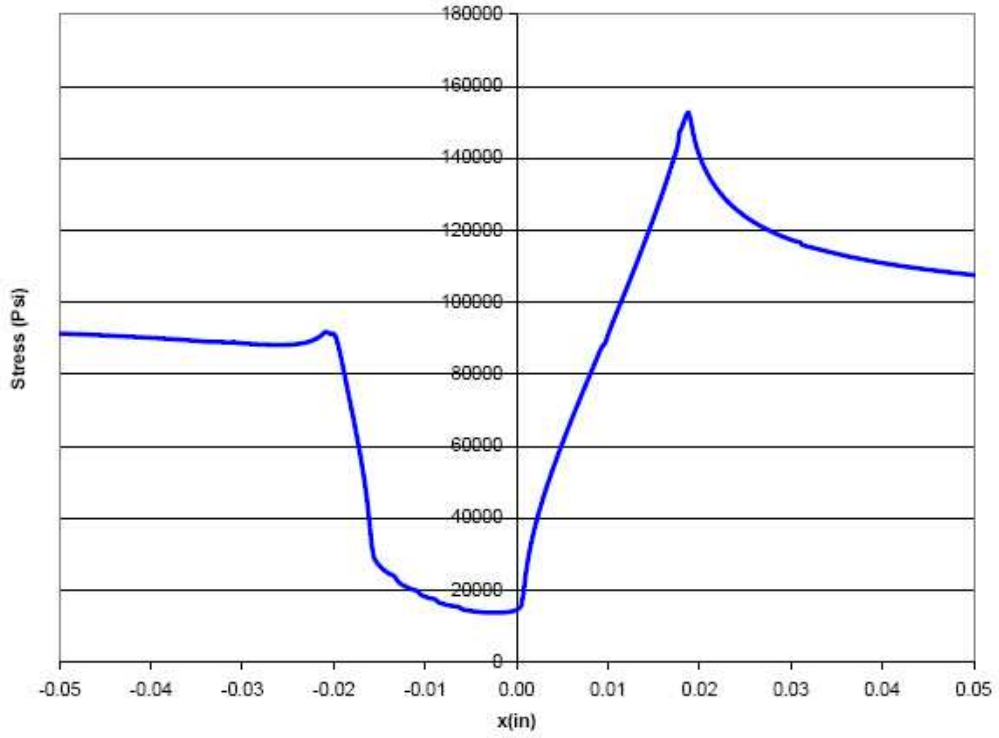

Figure B.1: Axial Stress Distribution along the Contact surface for Ti-6Al-4V

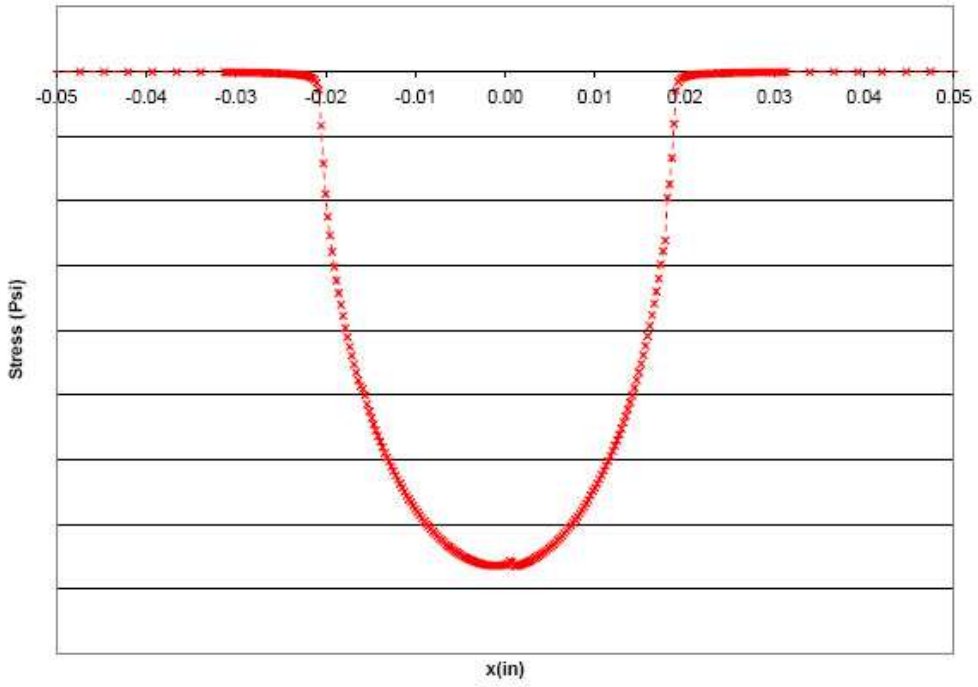

Figure B.2: Normal Stress Distribution along the Contact surface for Ti-6Al-4V

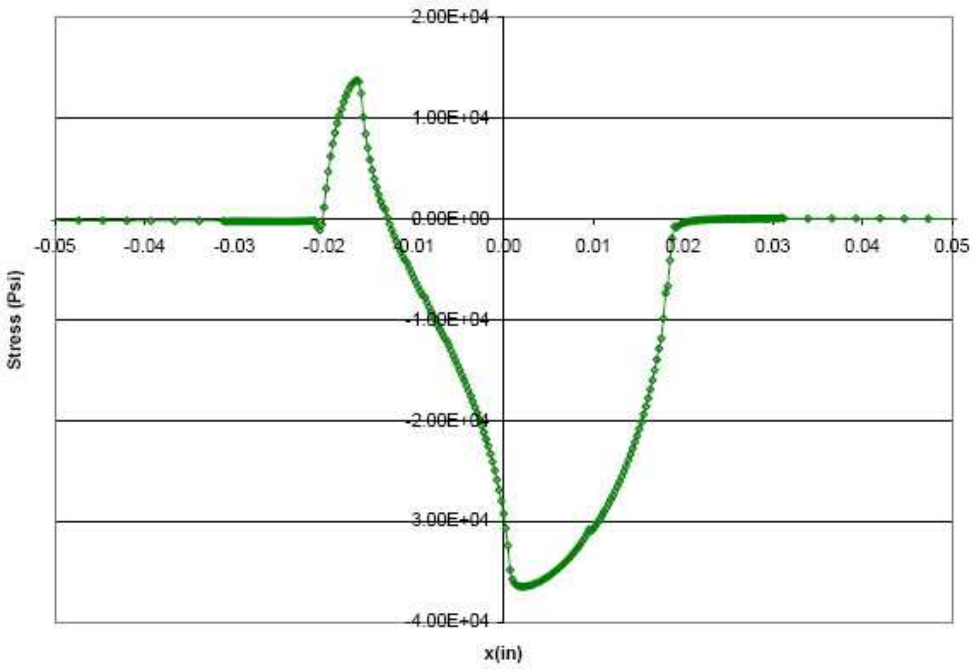

Figure B.3: Shear Stress Distribution along the Contact surface for Ti-6Al-4V

Appendix C. MSSR Intermediate Steps

This appendix, more intermediate steps are presented concerning the modification of MSSR constants in order to make the two pad radii curves collapse onto one single curve. As discussed in Section 5.5, this study adopted a second approach in this regard in order to keep some slope effect similar to the one seen in the S-N curve. This method involves changing the MSSR constants first similar to the Findley parameter approach, by reducing the normal stress factor (C) to even lower values than 0.35 used in the latter, as k factor.

Figure C.1 shows a comparison between MSSR parameter with constants A=0.5, B=1.0, C=0.35 and D=1.0 and the Findley parameter (FP). The comparison show that the two curves (for both pad radii) are not that far apart since they are almost defined in the same way. However, between the two pad radii curves, the separation is still apparent which means that this version of MSSR is not able to predict fatigue life without dependency on pad geometry.

Figure C.2 plots the two pad radii curves for a new MSSR definition with constants A=0.5, B=1.0, C=0.20 and D=1.0. As the figure depicts, the two curves are coming even closer together as C constant is decreased. Nonetheless, between the two pad radii curves, the separation is still apparent which means that this version of MSSR is also not able to predict fatigue life without dependency on pad geometry.

Finally, Fig. C.3 shows the two pad radii curves for a new MSSR definition with constants A=0.5, B=1.0, C=0.05 and D=1.0. This figure illustrates that the two curves are coming even closer together as C constant is decreased, while keeping similar slope to the S-N curve in Fig. 5.10. However, the two curves are still apart, while we have almost reached the limit on reducing C constants. Therefore, the shear stress constants A and B are modified in attempt to collapse the two pad curves onto a single curve, as discussed in Section 5.5.

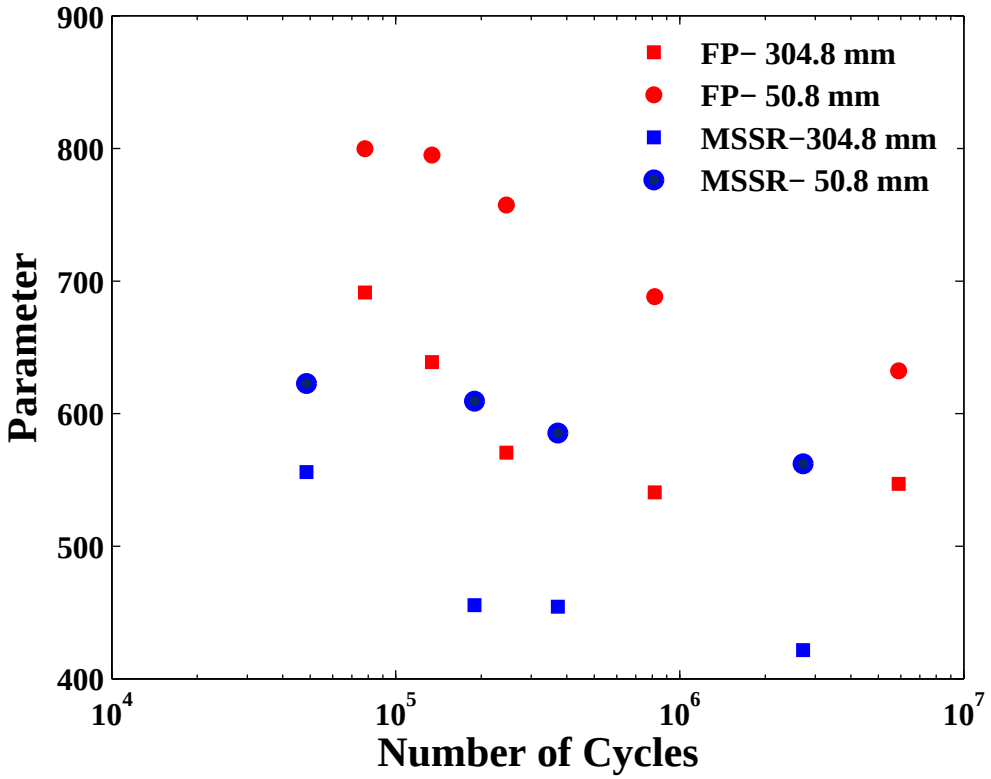

Figure C.1: Modified Shear Stress Range (MSSR) parameter and Findley Parameter (FP) versus Fretting Fatigue Life (A=0.5, B=1.0, C=0.35, D=1.0)

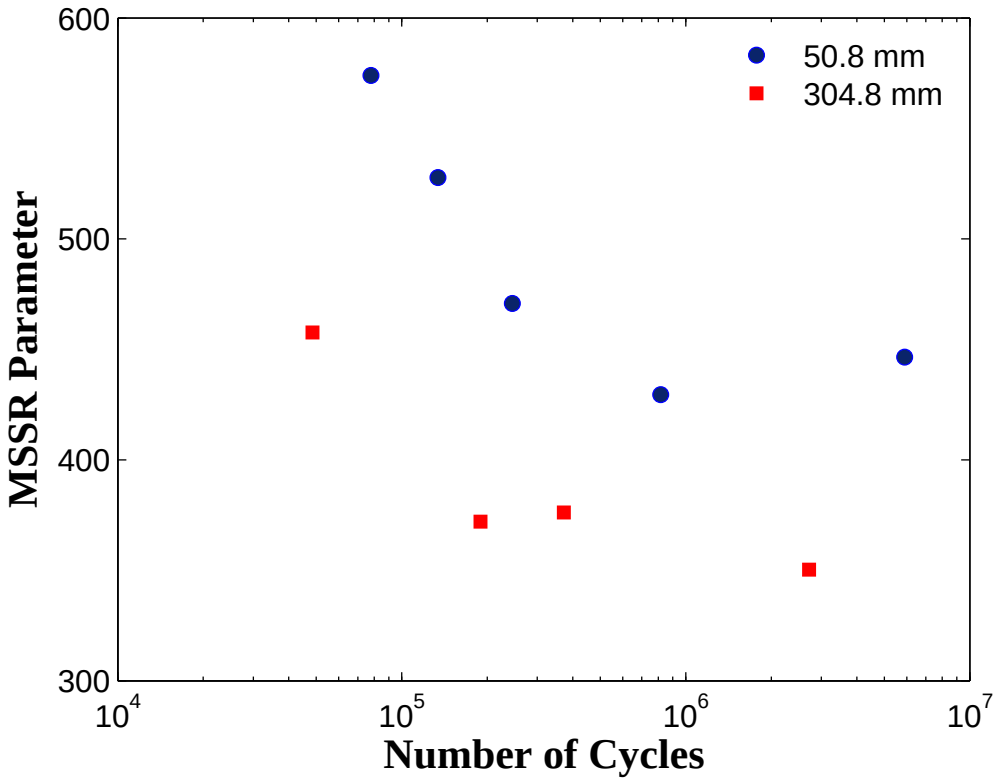

Figure C.2: Modified Shear Stress Range (MSSR) parameter versus Fretting Fatigue Life (A=0.5, B=1.0, C=0.20, D=1.0)

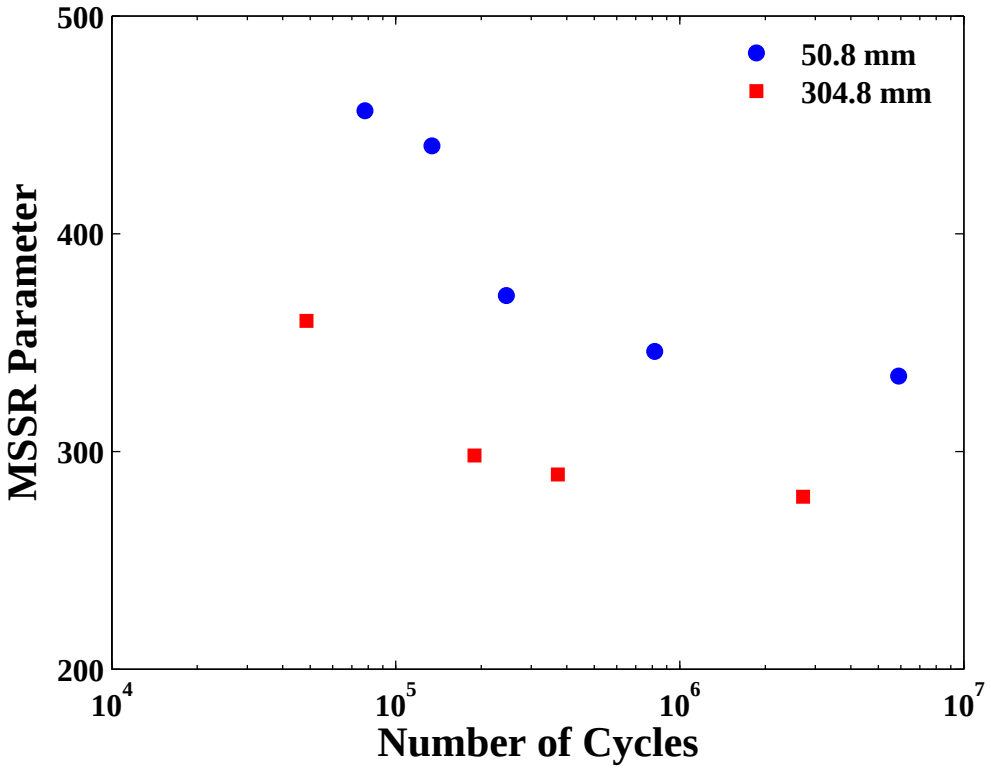

Figure C.3: Modified Shear Stress Range (MSSR) parameter versus Fretting Fatigue Life (A=0.5, B=1.0, C=0.05, D=1.0)

Bibliography

1. Adibnazari, S. "A Fretting Fatigue Normal Pressure Threshold Concept". *Wear*, 1993.

2. Adibnazari, S. and D. Hoeppner. "Study of Fretting Fatigue Crack Nucleation in 7075-T6 Aluminum Alloy". *Wear*, 159:257–264, 1992.

3. Albinali, S. *Effects of Temperature and Shot-Peening Intensity On Fretting Fatigue Behavior of Titanium Alloy Ti-6Al-4V*. Master's thesis, Graduate School of Engineering, Air Force Institute of Technology (AETC), Wright-Patterson AFB OH, March 2005. AFIT/GAE/ENY/052-M25.

4. Anton, D. *Structural Applications of Intermetallic Compounds*. John Wiley & sons Ltd., CT, USA, 1995.

5. Antoniou, R. and T. Radtke. "Mechanisms of Fertting Fatigue of Titanium Alloys". *Materials Science and Engineering*, A237:229–240, 1997.

6. Brien, V. and B. Decamps. "Low-Cycle Fatigue of Nickel-based Superalloy at High Temperature: Deformation Microstructures". *Materials Science and Engineering*, A316:18–31, 2001.

7. Chan, K. and Y. Lee. "Ruiz Program", 1998.

8. D., Lykins C., S. Mall, and V. K. Jain. "A Shear Stress Based Parameter For Fretting Fatigue Crack Initiation". *Fatigue and Fracture of Engineering Materials and Structures*.

9. Donachie, M. J. and S. J. Donachie. *handbook of Materials and Selection*. John Wiley & sons, Inc., New York, 2002.

10. Findley, W. N. "Fatigue of Metals Under Combinations of Stresses". *Transactions, ASME*, 79:1337–1348, 1957.

11. Harris, W. J. "The Influence of Fretting on Fatigue". *AGARD Specialists Meeting of Fretting in Aircraft Systems*, 1975.

12. Hattori, T. "Fretting Fatigue Analysis Using Fracture Mechanics". *JSME International Journal*, 100–107, July 1988.

13. Hattori, T. "Initiation and Propagation Behavior of Fretting Fatigue Cracks". *Proceedings of the* 3^{rd} *International Conference on Contact Mechanics*, 183–192. Madrid, Spain, July 1997.

14. Hills, D. and D. Nowell. "Contact Stress in a Moderately Thin Strip (with Particular Reference to Fretting Experiments". *Wear*, 185:235–238, 1995.

15. Iyer, K. and S. Mall. "Effects of Cyclic Frequency and Contact Pressure on Fretting Fatigue Under Two-Level Block Loading". *Fatigue and Fracture of Engineering Materials and Structures*, 23(ISSN 8756-758X):335–345, 2000.

16. Koshal, D. *Manufacturing Engineer's Reference Book*. Butterworth-Heinemann Ltd, Oxford, England, 1993.

17. Krgo, A., A. R. Kallmeyer, and P. Kurath. "Evaluation of HCF Multiaxial Fatigue Life Prediction Mehodologies for Ti-6Al-4V". *Proceedings of the 5th National Turbine Engine High Cycle Fatigue Conference*. Arizona, 2000.

18. Lundberg and A. Palmgren. "Dynamic Capacity of Rolling Bearings". *Acta Polytechnica-mech Eng. Series 1*, 1:4–51, 1947.

19. Lykins, C. D., S. Mall, and Douglas. *An Investigation of Fretting Fatigue Crack Initiation Behavior of the Titanium alloy Ti-6Al-4V*. Ph.D. dissertation, University of Dayton, OH, December 2004.

20. Magaziner, R. S. *Examination Of Contact Width On Fretting Fatigue*. Ph.D. dissertation, Graduate School of Engineering, Air Force Institute of Technology (AETC), Wright-Patterson AFB OH, March 2002. AFIT/GAE/ENY/02-8.

21. Migala, T. N. and T. L. Jacobs. "Low Plasticity Burnishing: An Affordable, Effective Means of Surface Enhancement". *Surface Enhancement technologies*, 1–9.

22. Mingjian, H. "Stress Distribution and Prediction of Crack Location in Dovetail Joints". *Journal of Aerospace Power*, 12:B307–B310, July 1991.

23. Murthy, H., D. B. Garcia, J. F. Matlik, and T. Farris. "Fretting Fatigue of Single Crystal/Polycrystalline Nickel Subjected to Blade/Disk Contact Loading". *Acta Astronautica*, 57:1–9, 2005.

24. Namjoshi, S. A., S. Mall, V. K. Jain, and O. Jin. "Fretting Fatigue Crack Initiation Mechanism in Ti-6Al-4V". *Fatigue Fracture Engineering Material Structure*, September 2001.

25. Namjoshi, S. A., A. Shantanu, S. Mall, V. K. Jain, and O. Jin. "Fretting Fatigue Crack-initiation Mechanism of Ti-6Al-4V". December 2000.

26. Nishioka, K. and K. Hirakawa. "Fundamental Investigations into Fretting Fatigue of Metals". *Bulletin of JSME, Part 2*, 12(50):180–187, 1969.

27. Piard, A., D. Gamby, C. Carbou, and J. Mendex. "A Numerical Simulation of Creep-Fatigue Crack Growth in a Nickel-base Superalloys". *Engineering Fracture Mechanics*, 71:2299–2317, 2004.

28. Sabelkin, V., S. A. Martinez, S. Mall, S. Sathish, and M. P. Blodgett. "Effect of Shot-peening Intensity on Fretting Fatigue Crack-initiation Behaviour of Ti-6Al-4V". *Fatigue Fract Engng Mater Struct*, September 2004.

29. Sakata, H. "An Application of Fracture Mechanics to Fretting Fatigue Analysis". *Proceedings of the International Conference*, 303–313. Amsterdam and New York, North Holland, 1987.

30. Shyam, A. and W. W. Milligan. "A Model for Slip Irreversibility, and its Effects on the Fatigue Crack Propagation Threshold in a Nickel-base Superalloy". *Acta Materialia*, 53:835–844, 2005.

31. Smith, A., P. Watson, and T. Topper. "A Stress Strain Function for the Fatigue of Metals". *Journal of Meterials, JMLSA*, 5:767–778, 1970.

32. Socie, D. "Multiaxial Fatigue Damage Models". *Journal of Engineering Material and Technology*, 109:293–298, 1987.

33. Sondhi, S. K., B. F. Dyson, and M. McLean. "Tension-Compression Creep Asymmetry In a Turbine Disc Superalloy: Roles of Internal Stress and Thermal Ageing". *Acta Materiala*, 52:1761–1772, December 2004.

34. Strudel, J. "Nickel Base Superalloys, An Engineering and Scientific Challenge". *NMD*, 2005.

35. Szolwinski, G. "Comparison of Fretting Fatigue Crack Nucleation Experiments to Multi-Axial Fatigue Theory Life Predictions". *Proceedings of the Symposia, 1997 ASME International Mechanical Engineering Congress and Exposition*, 449–457. Dallas, Texas, November 1997.

36. Szolwinski, G. and T. Farris. "Fretting Fatigue Crack Initiation- Aging Aircraft Concerns". *AIAA/ASME/ASCE/AHS/ASC Structures, Structural Dynamics, an Materials Conference, Technical Papers*, 2173–2179. Washington D.C, 1994.

37. Szolwinski, G. and T. Farris. "Mechanics of Fretting Fatigue Crack Formation". *Wear*, 198:93–107, 1996.

38. Szolwinski, G., G. Harish, and T. Farris. "An Experimental Study of Fretting Fatigue Crack Nucleation in Airframe Alloys". *Conference on Aging Aircraft*. 1997.

39. Szolwinski, G., G. Harish, P. McVeigh, and T. Farris. "The Role of Fretting Fatigue Crack Nucleation in the Onset of Widespread Fatigue Damage: Analysis and Experiments". *FAA-NASA Symposium on the Continued Airworthiness of Aircraft Structures*. 1996.

40. Walker, K. "The Effect of Stress Relation during Crack Propagation and Fatigue for 2024-Y3 and 7075-T6 Aluminum". *Presented to subcommittee E-9V Winter Meeting*. 1969.

41. Wan, J. S. and Z. F. Yue. "A Low-Cycle Fatigue Life Model of Nickel-based Single Crystal Superalloys Under Multiaxial Stress State". *Materials Science and Engineering*, A392:145–149, 2005.

42. Waterhouse, R. "Fertting Fatigue". *International Materials Review*, 37(2):77–97, 1992.

43. Yuksel, H. I. *Effects of Shot-Peening On Hight Cycle Fretting Fatigue Behavior of Ti-6Al-4V*. Master's thesis, Wright Patterson Air Force Base, OH, March 2002.

REPORT DOCUMENTATION PAGE

Form Approved
OMB No. 074-0188

1. REPORT DATE *(DD-MM-YYYY)*	**2. REPORT TYPE**	**3. DATES COVERED** *(From – To)*
23/03/2006	**Master's Thesis**	Sep 2004 – Mar 2006

4. TITLE AND SUBTITLE

Fretting Fatigue Behavior of Nickel Alloy IN100

5a. CONTRACT NUMBER

5b. GRANT NUMBER

5c. PROGRAM ELEMENT NUMBER

6. AUTHOR(S)

Madhi, Elhoucine, Captain, RMAF

5d. PROJECT NUMBER

5e. TASK NUMBER

5f. WORK UNIT NUMBER

7. PERFORMING ORGANIZATION NAMES(S) AND ADDRESS(S)

Air Force Institute of Technology
Graduate School of Engineering and Management (AFIT/EN)
2950 Hobson Way
WPAFB OH 45433-7765

8. PERFORMING ORGANIZATION REPORT NUMBER

AFIT/GAE/ENY/06-M22

9. SPONSORING/MONITORING AGENCY NAME(S) AND ADDRESS(ES)

AFRL/MLLP
Attn: Dr. Mark Blodgett
Metals, Ceramics and NDE Division
Materials and Manufacturing Directorate
2230 Tenth St. Suite 1, Bldg 655
Wright Patterson Air Force Base, OH DSN: 785-9799

10. SPONSOR/MONITOR'S ACRONYM(S)

11. SPONSOR/MONITOR'S REPORT NUMBER(S)

12. DISTRIBUTION/AVAILABILITY STATEMENT

APPROVED FOR PUBLIC RELEASE; DISTRIBUTION UNLIMITED.

13. SUPPLEMENTARY NOTES

14. ABSTRACT

In this study, a systematic investigation of the fretting fatigue behavior of nickel alloy, IN-100 was carried out. The study includes both experimental work and the corresponding analysis of the contact conditions, and the latter is accomplished using the finite element method. Fretting fatigue tests were performed over a wide range of axial stresses to examine both low and high cycle fretting fatigue under constant contact load and the influence of different pad geometries was also explored. It was observed that fretting reduced the fatigue strength of IN-100, and that increasing cylindrical pad radii does not have the same effect as in titanium-based alloys. The crack initiation location and orientation along the surface were measured using the Optical and Scanning Electron Microscopy (SEM). In all experiments, cracks were found to initiate near the contact zone trailing edge, and at an orientation of 45° with a scatter of 10°. Finite element analysis was conducted through the commercially available software, ABAQUS, to obtain the contact region state variables such as stress, strain and displacement. These state variables were needed for the computation and analysis of fretting fatigue crack initiation parameters which were Findley parameter, Smith-Watson-Topper (SWT) parameter, shear stress range (SSR), and modified shear stress range (MSSR). These parameters were evaluated based on their ability to predict crack location, crack initiation angle and fatigue life without dependence on contact geometry. The comparison of the analysis and the experimental results showed that fretting fatigue life is not only governed by shear stress on the critical plane, but also the normal stresses plays a role in the crack initiation mechanism. After adjusting the constants used in MSSR calculations for Ti-6Al-4V, it was found that MSSR parameter is also capable of predicting crack location, crack initiation angle and fatigue life in IN-100.

15. SUBJECT TERMS

Fatigue tests, fretting, nickel alloys, finite element analysis

16. SECURITY CLASSIFICATION OF:			**17. LIMITATION OF ABSTRACT**	**18. NUMBER OF PAGES**	**19a. NAME OF RESPONSIBLE PERSON**
REPORT	**ABSTRACT**	**c. THIS PAGE**			Dr. Shankar Mall, CIV, USAF (ENY)
U	**U**	**U**	**UU**	135	**19b. TELEPHONE NUMBER** *(Include area code)* (937) 255-3636, ext 4587; e-mail: Shankar.mall@afit.edu